GUIDANCE AND CONTROL OF A SUBMARINE-LAUNCHED CRUISE MISSILE

A THESIS SUBMITTED TO
THE GRADUATE SCHOOL OF NATURAL AND APPLIED SCIENCES
OF
MIDDLE EAST TECHNICAL UNIVERSITY

BY

SEMİH KÖKLÜCAN

IN PARTIAL FULFILLMENT OF THE REQUIREMENTS
FOR
THE DEGREE OF MASTER OF SCIENCE
IN
ELECTRICAL AND ELECTRONICS ENGINEERING

AUGUST 2019

Approval of the thesis:

GUIDANCE AND CONTROL OF A SUBMARINE-LAUNCHED CRUISE MISSILE

submitted by **SEMİH KÖKLÜCAN** in partial fulfillment of the requirements for the degree of **Master of Science in Electrical and Electronics Engineering Department, Middle East Technical University** by,

Prof. Dr. Halil Kalıpçılar
Dean, Graduate School of **Natural and Applied Sciences** ______________

Prof. Dr. İlkay Ulusoy
Head of Department, **Electrical and Electronics Engineering** ______________

Prof. Dr. M. Kemal Leblebicioğlu
Supervisor, **Electrical and Electronics Eng. Dept., METU** ______________

Examining Committee Members:

Prof. Dr. Ozan Tekinalp
Aerospace Eng. Dept., METU ______________

Prof. Dr. M. Kemal Leblebicioğlu
Electrical and Electronics Eng. Dept., METU ______________

Assoc. Prof. Dr. Afşar Saranlı
Electrical and Electronics Eng. Dept., METU ______________

Assist. Prof. Dr. Elif Vural
Electrical and Electronics Eng. Dept., METU ______________

Assist. Prof. Dr. Yakup Özkazanç
Electrical and Electronics Eng. Dept., Hacettepe University ______________

Date:

I hereby declare that all information in this document has been obtained and presented in accordance with academic rules and ethical conduct. I also declare that, as required by these rules and conduct, I have fully cited and referenced all material and results that are not original to this work.

Name, Surname: Semih Köklücan

Signature :

ABSTRACT

GUIDANCE AND CONTROL OF A SUBMARINE-LAUNCHED CRUISE MISSILE

Köklücan, Semih
M.S., Department of Electrical and Electronics Engineering
Supervisor: Prof. Dr. M. Kemal Leblebicioğlu

August 2019, 167 pages

A typical mission profile of submarine-launched cruise missiles begins with the launch phase which covers the motion of the missile from the launch to the water-exit and continues with the boost phase which lasts from the water-exit to the beginning of the cruise phase. In order to achieve the desired range of the launch and boost phases, efficient utilization of available energy which carries the missile to the beginning of the cruise phase is necessary. For this purpose, this study presents a new approach for energy-optimal control of the underwater and air motion of a submarine-launched cruise missile. In this approach, the aforementioned problem is modeled and solved as a minimum-effort optimal control problem. Then, the effects of initial and final conditions on energy need are investigated, and the optimal conditions that result with the minimum energy need are determined. Besides that, to control the motion of the missile from the sea surface to target, proportional-integral-derivative (PID), linear quadratic regulator (LQR) and pole-placement based autopilots are designed and compared with each other. Prior to the guidance and control design steps, six degrees of freedom (6 DOF) motion equations are derived, then the hydrodynamic and aerodynamic parameters are retrieved. The nonlinear 6 DOF motion model is simplified and linearized before minimum-effort optimal control design and autopilot studies. Results of the designed guidance and control strategies are presented through the nonlinear 6 DOF simulations. Finally, some comments are made and future studies are mentioned based on theoretical and simulation studies.

Keywords: Submarine-Launched Cruise Missile, Guidance, Control, Energy-Optimal Control, Six Degrees of Freedom Motion Model

ÖZ

DENİZALTINDAN FIRLATILAN BİR SEYİR FÜZESİNİN GÜDÜM VE KONTROLÜ

Köklücan, Semih
Yüksek Lisans, Elektrik ve Elektronik Mühendisliği Bölümü
Tez Yöneticisi: Prof. Dr. M. Kemal Leblebicioğlu

Ağustos 2019 , 167 sayfa

Denizaltından fırlatılan seyir füzelerine ait tipik bir görev profili, füzenin fırlatılışından sudan çıkışına kadar olan hareketini kapsayan fırlatma fazı ile başlayıp, sudan çıkıştan itibaren seyir fazı başlangıcına kadar süren yükselme fazı ile devam eder. Fırlatma ve yükselme fazı için hedeflenen menzil değerine ulaşmak amacıyla, füzeyi seyir başlangıç koşullarına taşıyacak mevcut enerjinin efektif bir şekilde kullanılması gerekmektedir. Bu amaçla, bu çalışmada denizaltından fırlatılan bir seyir füzesinin sualtı ve hava hareketi boyunca enerji-optimal kontrolü üzerine yeni bir yaklaşım sunulmuştur. Bu yaklaşımda, ifade edilen problem bir minimum-efor optimal kontrol problemi olarak modellenmiş ve çözülmüştür. Ardından başlangıç ve son koşulların enerji ihtiyacı üzerindeki etkileri incelenmiş ve minimum enerji ihtiyacını sağlayacak koşullar tespit edilmiştir. Bunun yanında, füzenin su yüzeyinden hedefe kadar olan hareketini kontrol etmek amacıyla, oransal-integral-türevsel (PID), doğrusal karesel regülatör (LQR) ve kutup yerleştirme temelli üç farklı otopilot tasarımı gerçekleştirilmiş ve birbiriyle karşılaştırılmıştır. Güdüm ve kontrol tasarımı yapılmadan önce, altı serbestlik dereceli (6 DOF) hareket denklemleri türetilmiş, ardından hidrodinamik ve

aerodinamik parametreler elde edilmiştir. Minimum-efor optimal kontrol ve otopilot tasarımı çalışmalarından önce, doğrusal olmayan 6 DOF hareket modeli sadeleştirilmiş ve doğrusallaştırılmıştır. Tasarlanan güdüm ve kontrol stratejilerinin sonuçları, doğrusal olmayan 6 DOF benzetimler kullanılarak ortaya konmuştur. Son olarak ise yürütülen teorik çalışmalar ve benzetim çalışmaları temel alınarak bazı yorumlar yapılmış ve gelecek çalışma alanlarından bahsedilmiştir..

Anahtar Kelimeler: Denizaltından Fırlatılan Seyir Füzesi, Güdüm, Kontrol, Enerji-Optimal Kontrol, Altı Serbestlik Dereceli Hareket Modeli

To my family...

ACKNOWLEDGMENTS

Firstly, I would like to express my gratitude to my supervisor Prof. Dr. M. Kemal Leblebicioğlu for his valuable guidance, encouragements, and insight throughout my research.

I want to extend my sincere thanks to my friends for their unique friendship during the whole period.

I also wish to thank my colleagues at TÜBİTAK SAGE for their moral, technical and academical support.

Finally, I would like to express my deepest appreciation to my family for their continuous and peerless love, help, and support.

TABLE OF CONTENTS

LIST OF TABLES

TABLES

LIST OF FIGURES

FIGURES

LIST OF ABBREVIATIONS

6 DOF	Six Degrees of Freedom
CB	Center of Buoyancy
CG	Center of Gravity
CO	Origin of the Body Frame
ECI	Earth-Centered Inertial Frame
LQR	Linear Quadratic Regulator
P	Proportional
PI	Proportional-Integral
PID	Proportional-Integral-Derivative
TVC	Thrust Vector Control

CHAPTER 1

INTRODUCTION

1.1 Motivation and Problem Definition

Cruise missiles are precision-guided weapons which are able to fly long distances to accomplish strategic or tactical missions. Through their flight, they are usually continuously powered by an engine and supported by aerodynamic surfaces to make use of the aerodynamic lift. Aircrafts, land-based launchers, ships or submarines can be used as launching platforms and cruise missiles can be used against land or sea targets. In terms of their cruise speed, their subsonic, hypersonic and supersonic versions exist [1]. The first, German V-1 "buzz bomb" and following examples of this critical technology, such as U.S. Matador and Regulus missile, were not able to obtain location information during flight. Then, it was not even possible that their guidance system is corrected with the position information [2]. However, from the beginning of their first development in the 1940s, modern cruise missiles of today are equipped with advanced technologies. From the guidance, navigation and control perspective, some of these technologies can be listed as follows: (i) inertial navigation systems assisted with satellite navigation systems, terrain contour matching systems, magnetic or barometric measurement systems (ii) imaging infrared and radar seeker systems (iii) digital scene matching systems (iv) two-way satellite communication which enables mission re-planning and acquisition of critical information during flight and (v) guidance concepts which allow some strategic plans such as waypoint navigation, loitering, terrain following, sea-skimming and etc [3–6]. In the light of given information, it is evident that cruise missiles can play a crucial role in the defense organizations of countries.

Submarine launching of cruise missiles differs from other launching methods in several important ways. Since the electromagnetic wave propagation is strongly attenuated by the seawater, radars cannot detect the submarines efficiently. Furthermore, the available sonar systems of today are not able to provide efficient detection ranges. The underwater operation can hide submarines from other reconnaissance missions performed by satellites and aerial vehicles. Therefore, concealment, sudden attack ability and high level of survivability are some aspects of submarine-launched missiles [7]. A typical launch, boost and initial cruise phases of a submarine-launched cruise missile are shown in Figure 1.1.

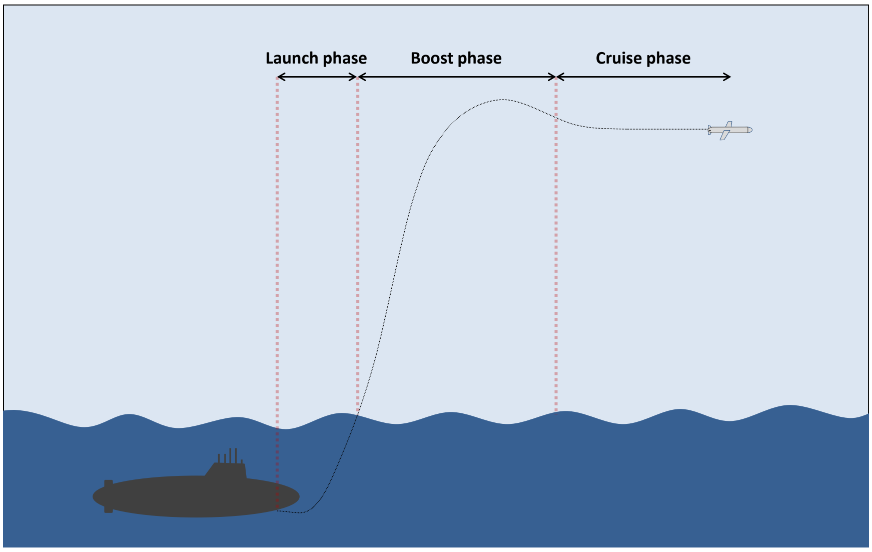

Figure 1.1: A typical mission initial phases of a submarine launched cruise missile

During the launch and boost phases, the commonly used control method is generating necessary forces and moments via thrust control. In general, these can be achieved by vectoring booster thrust or using additional lateral thrusters. Aerodynamic surfaces, which are less effective than the thrust forces and moments at low speed, may also be used in combination with thrust control [8], [9], [10].

Two conventional launching methods from submarines are vertical and horizontal launch, which are shown in Figure 1.2. In the former, the missile is launched from a vertical launching system of the submarine and generally reaches to the sea surface perpendicularly. For example, The Mk 45 vertical launching system that is used in some class of US submarines is shown in Figure 1.3, [11]. For the latter, the missile is launched from a horizontal tube on the submarine, and then the water-exit attitude of the missile can be controlled. Two methods to control the water-exit attitude are using a moment generating vectored thrust force or igniting the missile booster at a predetermined pitch angle/axial velocity conditions while the missile pitching upwards [12].

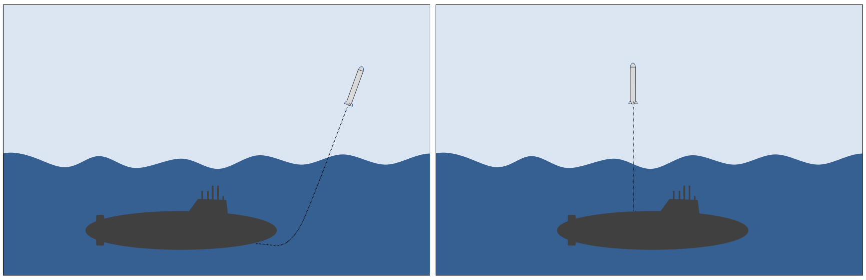

Figure 1.2: Horizontal and vertical launch from submarine

For both launching methods, in order to achieve the desired range or increase the range of the launch and boost phases, it is crucial to use available energy for thrust generation efficiently. The total energy need of the launch and boost phases can change according to the initial and final flight conditions of these phases and also with the total planned completion time. So, a control and guidance scheme to be applied should take into account these factors to increase missile range for the phases before starting to cruise.

Figure 1.3: The Mk 45 vertical launching system

1.2 Literature Survey

Most likely because of the confidentiality of the works related to the subject, the existing open literature does not have many studies on the guidance and control of underwater-launched missiles. However, some notable works are listed in this study. In [13], attitude and depth/height control of a submarine-to-air missile are achieved using Linear Quadratic Regulator and an optimal guidance law. Time-optimal control of a submarine-launched missile based on thrust vector deflection parameterization with the enhanced time-scaling method is given in [14]. [7] presents an adaptive fixed-time sliding mode attitude tracking control of a submarine-launched missile during water-exit motion. In addition to these works, there are some studies which focus on water-exit or just after water-exit control of some vehicles operationally and physically similar to missiles. [15] is a study in which a nonlinear sliding mode control utilizing an adaptive backstepping approach is designed in order to achieve an attitude tracking control for an out-of-water course of a high-speed underwater vehicle attacking aerial targets. [16] suggests a sliding mode controller which guarantees that an underwater-to-air vehicle reaches the desired conditions after leaving the water and it prevents the vehicle from falling back into the water.

Moreover, there are also some studies that do not include a controller design but concentrate on modeling and simulation of underwater launch and water-exit phases. In [17], the water-exit dynamic model which considers the added mass and its changing rate are established, and the water-exit motion is simulated. [18] is another work that focuses on the simulation of a vertically launched submarine missile's out-water movement. In [19], three-dimensional water-exit trajectory model of a submarine-launched missile is built based on dynamic mesh technique and simulations are performed to obtain characteristics of missile's water-exit trajectory and attitude. In [20], a water-exit mechanical model under wave effect is established based on the potential flow theory, and the numerical results are compared with the experimental results. [21] is a technical report which investigates whether measured underwater motion data of a missile can be predicted using equations of motion and hydrodynamic parameters obtained experimentally or theoretically.

1.3 Proposed Method

The examples of existing valuable studies from the open literature were given in the previous part. Especially, the studies which take guidance and control objectives into account are noteworthy here. However, one aspect that is not dealt with in these works is energy optimizing control, which can be a desirable objective in order to increase the missile range for the launch and boost phases. Obtaining some predefined flight conditions at the end of the boost phase may be necessary for real systems due to mission objectives or system constraints. For example; the cruise engine can only start within a specific altitude-speed envelope, or initial success of the cruise autopilot may depend on the flight conditions at which the boost phase ends. Therefore, effective usage of the available energy to increase missile range gives also the flexibility to the system designer to accomplish some other goals.

In our approach, to suggest a solution to the given problem, launch and boost phase control problem of a conceptual submarine launched cruise missile is modeled and solved as a minimum-effort optimal control problem. Formulated optimal control problems are transformed into optimization problems by discretizing them and then solved as a parameter optimization problem. The energy associative cost function to be minimized is determined as the integral of the square of the applied thrust. Firstly, the launch and boost phases are considered separately, and energy minimizing control solutions are found to satisfy the given initial and final conditions. These conditions include velocity, depth/altitude, attitude, and time interval. Secondly, the effects of the final and initial conditions on total energy need are investigated. The optimal conditions that result with the minimum energy need are determined. Where it is appropriate, initial and final conditions are also used as free parameters to be found, to minimize the control effort. Then, for the eventual initial and final conditions of the launch and boost phases, energy minimizing control solution and resulting flight scenario is obtained for these phases.

1.4 Publications

The papers originating from this study are listed in this section.

- "Energy Optimal Control of an Underwater-to-Air Missile's Underwater Motion" titled paper is accepted for "8th National Defense Applications Modeling and Simulation (USMOS) Conference, 2019" .
- "Minimum-Effort Optimal Control of a Submarine-Launched Cruise Missile's Underwater Motion" titled paper is accepted for "21th Local Conference of Turkish National Committee of Automatic Control (TOK), 2019"
- The studies for a journal paper publication have been going on.

1.5 Thesis Organization

The thesis organization can be summarized as follows. Chapter 1 presents the motivation and problem definition related to the energy-minimizing control of a submarine-launched cruise missile's launch and boost phases. Literature survey about the subject and the approach in this thesis are also presented. Publications that are originated from this study are given. In Chapter 2, the missile system is described with its flight modes, mission profile, control methods, and physical properties. Chapter 3 is dedicated to the mathematical modeling of the motion of the missile in 6 degrees of freedom. In Chapter 4, hydrodynamic and aerodynamic parameters of the missile are derived. In Chapter 5, minimum-energy guidance, and control design for launch and boost phases are accomplished. Autopilot design studies are presented in Chapter 6. Lastly, the results of the study are discussed and conclusions are given in Chapter 7.

CHAPTER 2

SYSTEM DESCRIPTION

2.1 Introduction

In this chapter; firstly, three different flight modes of the missile are defined. Each flight mode corresponds to a different outer geometry of the missile and different active control structure. Then, the complete mission profile that is seen from the launch to the target hit is described. This mission profile consists of four different phases, which are launch, boost, cruise, and terminal. After that, control methods in actuator level and their usage are explained. Last, physical properties for three different missile configurations are provided with the related parameter values.

2.2 Flight Modes

There are three different flight modes of the missile which accompany the mission phases described in the next section. The first flight mode is active through the launch phase, the second flight mode is active through the boost phase, and the third flight mode is active through the cruise and terminal phases. The flight modes and the usage of control means at these modes are shown in Table 2.1. Detailed physical properties for each flight mode are given in Section 2.5.

As it can be deduced from the information given in Table 2.1, in each flight mode the missile has a different type of hydrodynamic or aerodynamic configuration. The 2-dimensional views of these configurations are shown in Figure 2.1.

Flight Mode	Booster Motor	TVC	Tail Fins	Wings	Cruise Engine
1	On	Off	Off	Off	Off
2	On	On	On	Off	Off
3	Jettisoned	-	On	On	On

Table 2.1: Flight modes and active control means

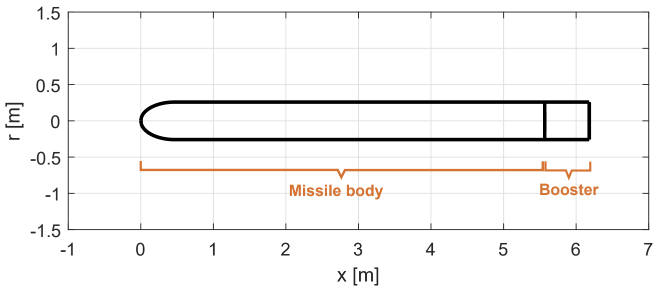

(a) Flight Mode 1

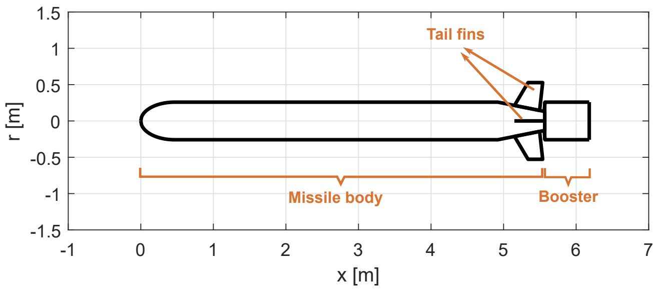

(b) Flight Mode 2

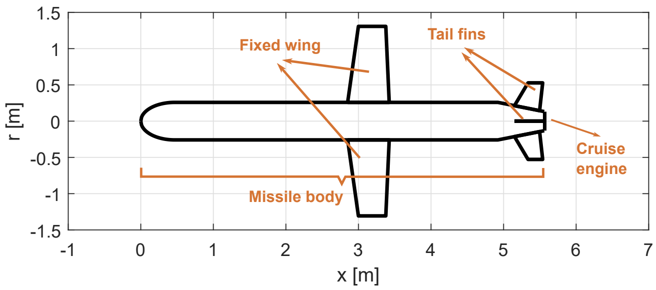

(c) Flight Mode 3

Figure 2.1: 2-dimensional views of different flight modes

2.3 Mission Profile

The conceptual submarine launched cruise missile in this work has a mission profile which consists of four main phases. These are the launch phase, boost phase, cruise phase, and terminal phase, which can be seen in Figure 2.2.

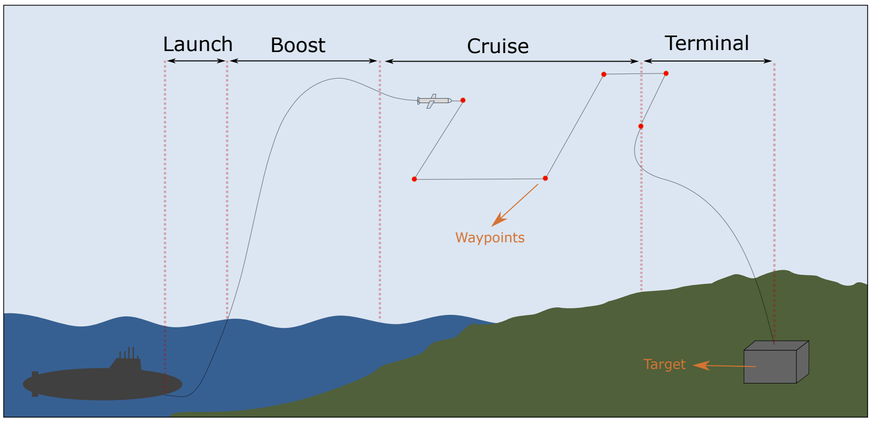

Figure 2.2: Mission profile with launch, boost, cruise and terminal phases

Launch phase: This phase starts with the missile's vertical or horizontal ejection from the submarine and ends when the missile reaches to the sea surface. After the ejection, the booster motor is ignited to generate the necessary force to move the missile upwards. For vertical ejection case, a vertical water-exit is achieved. However, different water-exit attitude angles can be achieved for the horizontal ejection case. This is done by igniting the missile booster at a predetermined condition while the missile is pitching upwards after the horizontal ejection and then applying a predetermined booster thrust profile. The design characteristic, which makes the missile's pitch-up motion possible after the horizontal ejection, will be explained in Section 2.5.

Boost phase: This phase covers the motion from the sea surface to an altitude at which the missile climbs before it starts to cruise. In this phase, tail fins are deployed to achieve zero roll motion, and the booster thrust vector control is activated to accomplish attitude control. It should be noted that, until the last section of this phase where the missile is close to the zero-pitch angle condition, the lifting forces which provide the upward motion are substantially come from the booster thrust force, and the contribution of the aerodynamic lifting force is relatively small due to the aerodynamic configuration.

Cruise phase: When the missile reaches a predefined flight condition at the end of the boost phase, the cruise phase starts and continues until the terminal phase begins. At the beginning of this phase, the booster motor is jettisoned, the cruise engine starts, and fixed wings are deployed. The tail fins, which are already deployed in the previous phase, are used as aerodynamic control surfaces. Through the cruise phase, a guidance and control scheme for waypoint navigation and altitude hold is applied.

Terminal phase: The terminal phase starts at a predefined range from the target. Then, the appropriate terminal guidance scheme is initiated to reach that target's coordinate.

2.4 Control Methods

During the whole flight of the missile, several control methods are applied. They are explained as follows.

Thrust Vector Control (TVC): This method is used to control the attitude of the missile through the boost phase as the second flight mode is active. In this study, TVC is accomplished by deflecting the thrust generated by the booster motor. The point of application of this thrust and possible deflections are shown in Figure 2.3, and mathematical thrust force and moment model will be given in Chapter 3. The actuator dynamic model which provides thrust deflection will be given in Chapter 6.

Aerodynamic Control with Tail Fins: Tail fins are deployed in the boost phase and used until the end of the terminal phase. Viewing from the rear, they are located with "+" configuration as shown in Figure 2.4. They generate the aerodynamic control surface deflections, which are deflections of elevator, rudder, and aileron surfaces. In the boost phase, tail fins are used to keep roll angle at zero. When the cruise phase starts, the control of the missile at pitch, roll and yaw axes are done using aerodynamic control via tail fins. The fin actuator system's dynamic model will be given in Chapter 6.

Thrust Magnitude Control: In this study, the magnitude of the generated thrust

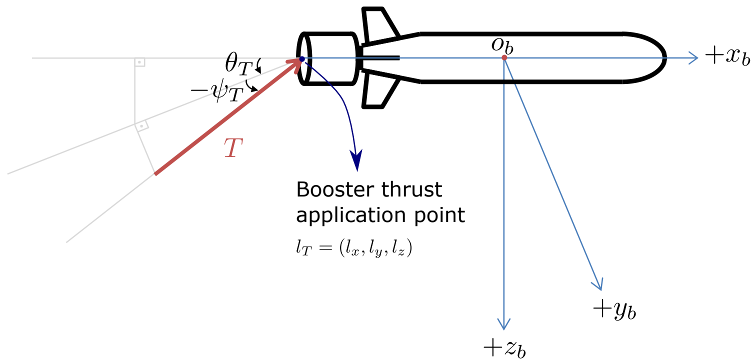

Figure 2.3: Application point of booster thrust and thrust deflection angles

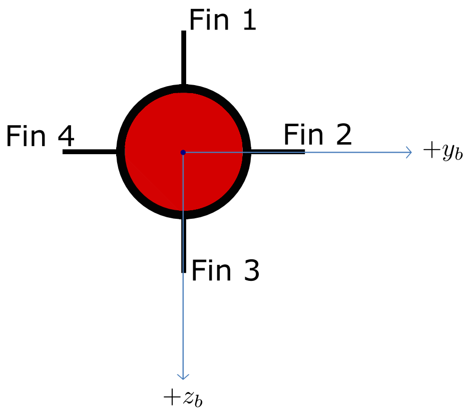

Figure 2.4: View of tail fins from the rear side of the missile

by booster motor and cruise motor can be controlled. The control of the booster motor thrust is done to achieve an energy minimizing control during launch and boost phases. On the other hand, generated thrust by the cruise engine is controlled to realize the commanded speed during the cruise and terminal phases. Both the booster motor and cruise engine models are ideal, such that the commanded thrust force is exactly generated. While the booster motor can provide a thrust force between 0 and 30 kN, the cruise engine can generate a thrust force between 0 and 10 kN.

2.5 Physical Properties

Physical properties of the missile are needed for several reasons in this study. The derivation procedure of hydrodynamic/aerodynamic parameters is conducted by using the physical parameter values of the missile. Furthermore, the mathematical model of the missile, which is constructed in Chapter 3, is based on both physical properties and hydrodynamic/aerodynamic model database. Moreover, physical properties are necessary through the control system design. Thus, the physical properties are provided here as a part of the system description. To form a basis for the conceptual cruise missile design in this study, the Tomahawk cruise missile is chosen. For the data which is not available in the related open sources, reasonable values are chosen or calculated according to the physical model of the missile.

The missile in this study has a cylinder-like shape in Flight Mode 1. The nose of the missile can be considered as a half spheroid. Taking the missile nose as origin; for Flight Mode 1, the radius of the missile, $r(x)$, with respect to the length, x, is given as

$$r(x) = \begin{cases} 0.2588\sqrt{1 - \dfrac{(x-0.4661)^2}{0.4661}}, & \text{for } 0 \leq x \leq 0.4661 \\ 0.2588, & \text{for } 0.4661 < x \leq 6.1806 \end{cases} \tag{2.1}$$

For Flight Mode 2, the change of the radius with the length is given as

$$r(x) = \begin{cases} 0.2588\sqrt{1 - \dfrac{(x-0.4661)^2}{0.4661}}, & \text{for } 0 \leq x \leq 0.4661 \\ 0.2588, & \text{for } 0.4661 < x \leq 4.9216 \\ -0.1988(x-4.9216) + 0.2588 & \text{for } 4.9216 < x \leq 5.5666 \\ 0.2588, & \text{for } 5.5666 < x \leq 6.1806 \end{cases} \tag{2.2}$$

For Flight Mode 3, the same radius formula in Equation (2.2) can be used up to 5.5666 m length, which is also the total length for this mode since the booster motor is jettisoned.

Physical parameters for all flight modes are given in Table 2.2. Here, I_x, I_y, I_z are moments of inertia about rotational axes. The rotational axes are related to the missile body frame whose definition can be found in Chapter 3. (x_{cg}, y_{cg}, z_{cg}) is the location of the center of gravity, (x_{cb}, y_{cb}, z_{cb}) is the location of the center of buoyancy. The reference point, $(0, 0, 0)$, for these locations is the missile nose and the positive x-axis direction is from the nose to the rear side of the missile. This measurement frame and the locations of the center of gravity and center of buoyancy are shown in Figure 2.5. It should be noted that drawing and center locations are not to scale.

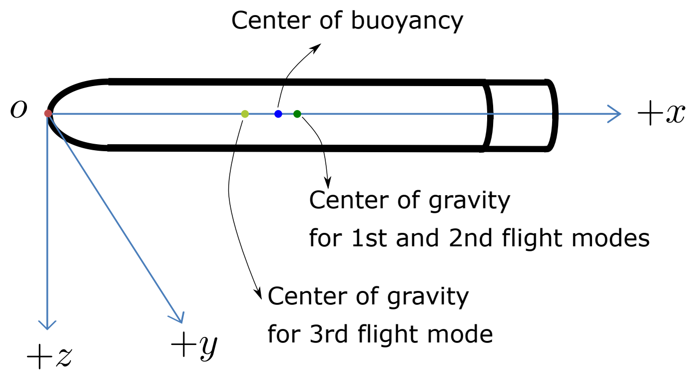

Figure 2.5: The locations of the center of gravity and buoyancy in their measurement frame

According to the information given in Table 2.2, noting some points may be useful. The length, mass, moments of inertia for pitch and yaw axes, location of the center of gravity of the missile for first and second modes change only when the booster motor is jettisoned in the third flight mode. Also, when the fixed wings are deployed in the last flight mode, the reference area is calculated according to the area spanned by the wings. The volume of the missile and location of the center of buoyancy are only provided for the first flight mode since they are only necessary for this mode.

As it is mentioned previously, following the horizontal ejection from a submarine, the missile has a tendency to pitch upwards. This is possible with the position relationship between the center of buoyancy and the center of gravity. Since the center of buoyancy is closer to the nose of the missile than that of the center of gravity, buoyancy force generates an upwards pitching moment for the nose. By making use of this

Parameter	Mode 1 Value	Mode 2 Value	Mode 3 Value	Unit
Length	6.1806	6.1806	5.5666	m
Diameter	0.5175	0.5175	0.5175	m
Mass	1513	1513	1243	kg
Reference Area	0.2104	0.2104	1.3047	m^2
Volume	1.332	-	-	m^3
Wingspan	-	-	2.6138	m
I_x	50.6684	50.6684	50.6684	kgm^2
I_y	4841.6944	4841.6944	3932.4233	kgm^2
I_z	4841.6944	4841.6944	3932.4233	kgm^2
(x_{cg}, y_{cg}, z_{cg})	(3.1903, 0, 0)	(3.1903, 0, 0)	(2.6388, 0, 0)	m
(x_{cb}, y_{cb}, z_{cb})	(3.0903, 0, 0)	-	-	m

Table 2.2: Physical parameters for all flight modes

design characteristic, water-exit attitude control will be achieved by using the booster thrust force without any thrust deflection.

CHAPTER 3

MATHEMATICAL MODELING

3.1 Introduction

This chapter is devoted to the construction of the missile's rigid body kinetics. In the scope of this study, the rigid body equations of motion should be derived for several reasons. Firstly, the missile's motion in 6 degrees of freedom (6 DOF) is simulated using rigid body motion equations which describe translational and rotational motion of the missile. Secondly, guidance and control design procedures that will be followed in the next chapters use simplified or linearized versions of nonlinear 6 DOF motion equations. The rigid body equations of motion will be derived using the Newton-Euler formulation and vectorial mechanics. The procedures in [22], [23] and [24] will be followed through the derivation steps. After the rigid body kinetics are obtained, hydrodynamic and aerodynamic, gravitational and buoyancy, and thrust force and moments that act on the missile body are explained in detail.

From now on in this study, the following notation is used to describe a property:

- While a boldface variable $\boldsymbol{y}$ represents an $n \times m$ property where n, m or both n and m are greater than one, a not boldface variable y represents a scalar.
- $\boldsymbol{y}_{\alpha\beta}^{\gamma}$ corresponds to $\boldsymbol{y}$ property of α frame with respect to β frame resolved in γ frame [25].

3.2 Kinematics

Motion Variables

In order to define the position and orientation of a vehicle which moves in 6 degrees of freedom, six independent coordinates are needed. These coordinates can be divided into two such that they both have three coordinates. While coordinates of the first group and their time derivatives are related to the position and translational motion, coordinates of the second group describe the orientation and rotational motion. The motion variables are shown in Figure 3.1 and Table 3.1. The body frame which is seen in Figure 3.1 will be explained in Section 3.2.1.

DOF		Forces and Moments	Linear and Angular Velocities	Positions and Euler Angles
1	motions in the x-direction (forward)	X	u	x
2	motions in the y-direction (side)	Y	v	y
3	motions in the z-direction (down)	Z	w	z
4	rotation about the x-axis (roll)	L	p	ϕ
5	rotation about the y-axis (pitch)	M	q	θ
6	rotation about the z-axis (yaw)	N	r	ψ

Table 3.1: The 6 DOF motion variables

The vectors defined below can be used to describe the motion of a vehicle which moves in 6 DOF

$$\boldsymbol{\eta} = [\boldsymbol{\eta}_1^T, \boldsymbol{\eta}_2^T]^T \qquad \boldsymbol{\eta}_1 = [x, y, z]^T \qquad \boldsymbol{\eta}_2 = [\phi, \theta, \psi]^T$$

$$\boldsymbol{\nu} = [\boldsymbol{\nu}_1^T, \boldsymbol{\nu}_2^T]^T \qquad \boldsymbol{\nu}_1 = [u, v, w]^T \qquad \boldsymbol{\nu}_2 = [p, q, r]^T$$

$$\boldsymbol{\tau} = [\boldsymbol{\tau}_1^T, \boldsymbol{\tau}_2^T]^T \qquad \boldsymbol{\tau}_1 = [X, Y, Z]^T \qquad \boldsymbol{\tau}_2 = [L, M, N]^T$$

where $\boldsymbol{\eta}$ is the position and orientation vector with coordinates in the Earth-fixed frame (definition of this frame is given in Section 3.2.1), $\boldsymbol{\nu}$ is the linear and angular velocity vector with coordinates in the body frame and $\boldsymbol{\tau}$ is the vector that shows

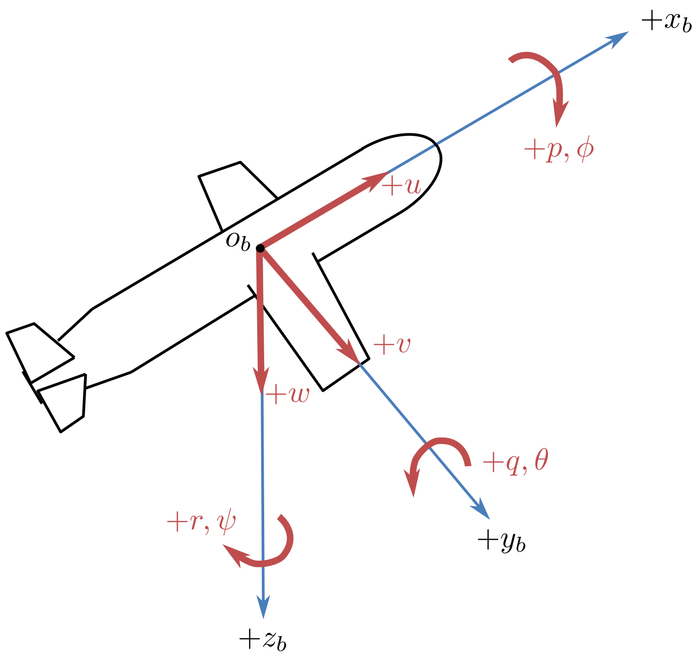

Figure 3.1: The 6 DOF motion variables in the body frame

forces and moments acting on the vehicle in the body frame.

3.2.1 Coordinate Frames

Earth-Centered Inertial Frame(ECI): Since the Newton's laws of motion are applicable in an inertial frame, a non-accelerating and non-rotating reference frame should be defined in order to derive the 6 DOF equations of motion. For that purpose, Earth-Centered Inertial Frame(ECI) is defined in the literature of flight dynamics and navigation (Figure 3.2). Through this work, this frame will be denoted by $\{i\}$. The ECI is centered at the Earth's center. z_i axis is directed to the true North pole. $x_i - y_i$ plane coincides with the equatorial plane, x_i and y_i axes do not rotate with the Earth. x_i direction is defined as the vector from the center of the Earth pointed to the Sun at the vernal equinox. y_i axis is orthogonal to the x_i and z_i direction according to the right-hand rule. The ECI is not a true inertial frame since the Earth accelerates in its orbit around the Sun, its spin axis slowly moves and the Galaxy rotates. Nevertheless, inertial frame assumption is sufficiently accurate for purposes such as flight dynamics or navigation [25], [26].

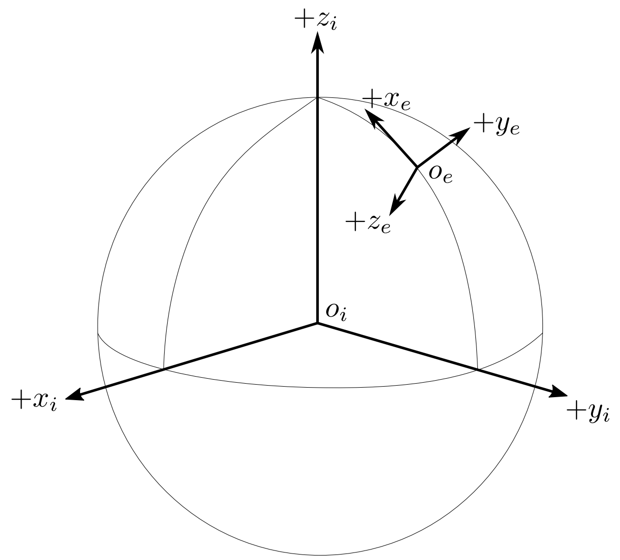

Figure 3.2: Earth-Centered Inertial Frame and Earth-Fixed Frame

Earth-Fixed Frame: The $\{e\}$ notation will be used to denote this frame (Figure 3.2). It has its origin at a fixed point on the Earth's surface. x_e axis points towards North, z_e axis points downwards, and the y_e axis is the complementing orthogonal axis found by the right-hand rule.

In the scope of this work, the Earth-fixed frame will be used as inertial frame since the motion of this frame is much smaller than that of the missile.

Body Frame: The notation $\{b\}$ will refer to this frame throughout the study (Figure 3.3). Its origin is fixed to a point of the missile. For the missile, the body axes x_b, y_b, z_b are chosen to coincide with the principal axes of inertia, and they are defined as: x_b points along to the nose, y_b is directed to right when viewed from rear and orthogonal to x_b, and z_b completes the orthogonal set according to the right-hand rule.

3.2.2 Transformation Matrices

Let's define the position, attitude, linear velocity and angular velocity vectors as,

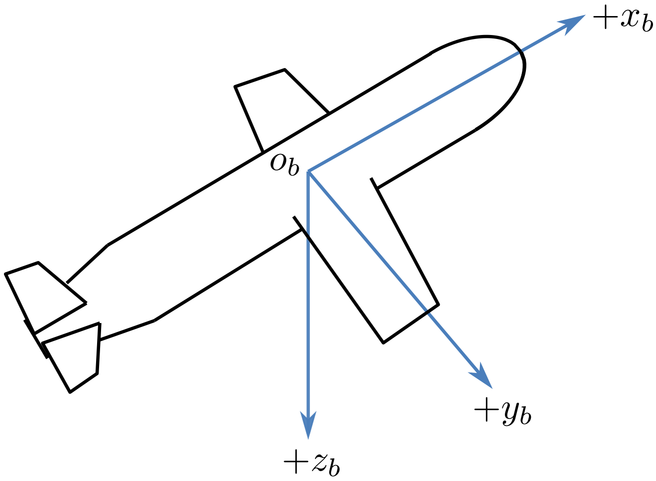

Figure 3.3: The body frame

$$\boldsymbol{r}^e_{be} = \begin{bmatrix} x^e_{be} \\ y^e_{be} \\ z^e_{be} \end{bmatrix} \qquad \boldsymbol{\Psi}^e_{be} = \begin{bmatrix} \phi^e_{be} \\ \theta^e_{be} \\ \psi^e_{be} \end{bmatrix} \qquad \boldsymbol{\nu}^b_{be} = \begin{bmatrix} u^b_{be} \\ v^b_{be} \\ w^b_{be} \end{bmatrix} \qquad \boldsymbol{\omega}^b_{be} = \begin{bmatrix} p^b_{be} \\ q^b_{be} \\ r^b_{be} \end{bmatrix}$$

Then, the missile's flight path relative to $\{e\}$ is given by the following velocity transformation:

$$\dot{\boldsymbol{r}}^e_{be} = \boldsymbol{J}_1(\boldsymbol{\Psi}^e_{be})\boldsymbol{\nu}^b_{be} \tag{3.1}$$

where $\boldsymbol{J}_1(\boldsymbol{\Psi}^e_{be})$ is a transformation matrix which is related through the functions of the Euler angles. The inverse velocity transformation can be written as:

$$\boldsymbol{\nu}^b_{be} = \boldsymbol{J}_1^{-1}(\boldsymbol{\Psi}^e_{be})\dot{\boldsymbol{r}}^e_{be} \tag{3.2}$$

Let $\boldsymbol{a}$ and $\boldsymbol{b}$ are vectors fixed in A and B frames. The vector $\boldsymbol{b}$ can be expressed in terms of the vector $\boldsymbol{a}$ with the relationship given below [27]:

$$\boldsymbol{b} = \cos(\beta)\boldsymbol{a} + (1 - \cos(\beta))\boldsymbol{\lambda}\boldsymbol{\lambda}^T\boldsymbol{a} - \sin(\beta)\boldsymbol{\lambda} \times \boldsymbol{a} \tag{3.3}$$

where $\boldsymbol{\lambda} = [\lambda_1, \lambda_2, \lambda_3]^T$ is the unit vector parallel to the axis of rotation which B is rotated about and β is the rotation angle of frame B. Equation (3.3) can be simplified as:

$$\boldsymbol{b} = \boldsymbol{C}\boldsymbol{a} \tag{3.4}$$

where $\boldsymbol{C}$ can be considered as an operator which rotates a fixed vector $\boldsymbol{a}$ to a new vector $\boldsymbol{C}\boldsymbol{a}$ and it can be expressed as:

$$\boldsymbol{C} = \cos(\beta)\boldsymbol{I} + (1 - \cos(\beta))\boldsymbol{\lambda}\boldsymbol{\lambda}^T - \sin(\beta)\boldsymbol{S}(\boldsymbol{\lambda}) \tag{3.5}$$

where $\boldsymbol{I}$ is the 3×3 identity matrix and $\boldsymbol{S}(\boldsymbol{\lambda})$ is a skew-symmetric matrix defined such that $\boldsymbol{\lambda} \times \boldsymbol{a} \triangleq \boldsymbol{S}(\boldsymbol{\lambda})\boldsymbol{a}$, that is:

$$\boldsymbol{S}(\boldsymbol{\lambda}) = \begin{bmatrix} 0 & -\lambda_3 & \lambda_2 \\ \lambda_3 & 0 & -\lambda_1 \\ -\lambda_2 & \lambda_1 & 0 \end{bmatrix} \tag{3.6}$$

By using Equation (3.5), the expressions for the matrix elements C_{ij} are obtained as:

$$\begin{aligned}
C_{11} &= (1 - \cos(\beta))\lambda_1^2 + \cos(\beta) \\
C_{22} &= (1 - \cos(\beta))\lambda_2^2 + \cos(\beta) \\
C_{33} &= (1 - \cos(\beta))\lambda_3^2 + \cos(\beta) \\
C_{12} &= (1 - \cos(\beta))\lambda_1\lambda_2 + \lambda_3 \sin(\beta) \\
C_{21} &= (1 - \cos(\beta))\lambda_2\lambda_1 - \lambda_3 \sin(\beta) \\
C_{23} &= (1 - \cos(\beta))\lambda_2\lambda_3 + \lambda_1 \sin(\beta) \\
C_{32} &= (1 - \cos(\beta))\lambda_3\lambda_2 - \lambda_1 \sin(\beta) \\
C_{31} &= (1 - \cos(\beta))\lambda_3\lambda_1 + \lambda_2 \sin(\beta) \\
C_{13} &= (1 - \cos(\beta))\lambda_1\lambda_3 - \lambda_2 \sin(\beta)
\end{aligned} \tag{3.7}$$

Principal Rotations

By substituting $\boldsymbol{\lambda} = [1, 0, 0]^T$, $\boldsymbol{\lambda} = [0, 1, 0]^T$ and $\boldsymbol{\lambda} = [0, 0, 1]^T$ matrices into Equation (3.7), respectively, the principal rotation matrices are obtained. These rotation matrices are:

$$\boldsymbol{C}_{x,\phi} = \begin{bmatrix} 1 & 0 & 0 \\ 0 & \mathrm{c}\phi & \mathrm{s}\phi \\ 0 & -\mathrm{s}\phi & \mathrm{c}\phi \end{bmatrix} \qquad \boldsymbol{C}_{y,\theta} = \begin{bmatrix} \mathrm{c}\theta & 0 & -\mathrm{s}\theta \\ 0 & 1 & 0 \\ \mathrm{s}\theta & 0 & \mathrm{c}\theta \end{bmatrix} \qquad \boldsymbol{C}_{z,\psi} = \begin{bmatrix} \mathrm{c}\psi & \mathrm{s}\psi & 0 \\ -\mathrm{s}\psi & \mathrm{c}\psi & 0 \\ 0 & 0 & 1 \end{bmatrix}$$

where $\mathrm{c}\cdot = \cos(\cdot)$ and $\mathrm{s}\cdot = \sin(\cdot)$. The notation $\boldsymbol{C}_{i,\alpha}$ denotes a rotation angle α about the i-axis. All $\boldsymbol{C}_{i,\alpha}$ satisfy the property given below:

Property 3.2.1 (Coordinate Transformation Matrix:) *A coordinate transformation matrix from the set of all* 3×3 *rotation matrices satisfies:*

$$\boldsymbol{C}\boldsymbol{C}^T = \boldsymbol{C}^T\boldsymbol{C} = \boldsymbol{I}$$

$$det\boldsymbol{C} = 1$$

which implies that $\boldsymbol{C}$ *is orthogonal. Then, the inverse coordinate transformation matrix can be found as:* $\boldsymbol{C}^{-1} = \boldsymbol{C}^T$

Linear Velocity Transformation

Usually the transformation matrix $\boldsymbol{J}_1(\boldsymbol{\Psi}^e_{be})$ is defined by three rotations. It should be noted that the order of the rotation sequence is not arbitrary. In guidance and control literature, the common approach is to use xyz-convention specified in terms of Euler angles for rotations. According to this convention, if ψ, θ, ϕ angle rotations are applied to $\{e\}$ frame about its z_e, y_e, x_e axes to obtain a frame which is parallel to $\{b\}$, the following rotation sequence is written as:

$$\boldsymbol{J}_1(\boldsymbol{\Psi}^e_{be}) = \boldsymbol{C}^T_{z,\psi}\boldsymbol{C}^T_{y,\theta}\boldsymbol{C}^T_{x,\phi} \tag{3.8}$$

and it implies that:

$$\boldsymbol{J}_1(\boldsymbol{\Psi}^e_{be}) = \begin{bmatrix} \mathrm{c}\psi\mathrm{c}\theta & -\mathrm{s}\psi\mathrm{c}\phi + \mathrm{c}\psi\mathrm{s}\theta\mathrm{s}\phi & \mathrm{s}\psi\mathrm{s}\phi + \mathrm{c}\psi\mathrm{c}\phi\mathrm{s}\theta \\ \mathrm{s}\psi\mathrm{c}\theta & \mathrm{c}\psi\mathrm{c}\phi + \mathrm{s}\phi\mathrm{s}\theta\mathrm{s}\psi & -\mathrm{c}\psi\mathrm{s}\phi + \mathrm{s}\theta\mathrm{s}\psi\mathrm{c}\phi \\ -\mathrm{s}\theta & \mathrm{c}\theta\mathrm{s}\phi & \mathrm{c}\theta\mathrm{c}\phi \end{bmatrix} \tag{3.9}$$

where $\boldsymbol{J}_1(\boldsymbol{\Psi}_{be}^e)$ represents the transformation matrix from the body frame $\{b\}$ to the Earth-fixed frame $\{e\}$.

Angular Velocity Transformation

The relationship between the angular velocity vector $\boldsymbol{\omega}_{be}^b$ and the Euler rate vector $\dot{\boldsymbol{\Psi}}_{be}^e$ can be defined with a transformation matrix $\boldsymbol{J}_2(\boldsymbol{\Psi}_{be}^e)$ as:

$$\dot{\boldsymbol{\Psi}}_{be}^e = \boldsymbol{J}_2(\boldsymbol{\Psi}_{be}^e)\boldsymbol{\omega}_{be}^b \tag{3.10}$$

One way to derive the transformation matrix $\boldsymbol{J}_2(\boldsymbol{\Psi}_{be}^e)$ is firstly writing the relationship given below:

$$\boldsymbol{\omega}_{be}^b = \begin{bmatrix} \dot{\phi} \\ 0 \\ 0 \end{bmatrix} + \boldsymbol{C}_{x,\phi} \begin{bmatrix} 0 \\ \dot{\theta} \\ 0 \end{bmatrix} + \boldsymbol{C}_{x,\phi}\boldsymbol{C}_{y,\theta} \begin{bmatrix} 0 \\ 0 \\ \dot{\psi} \end{bmatrix} = \boldsymbol{J}_2^{-1}(\boldsymbol{\Psi}_{be}^e)\dot{\boldsymbol{\Psi}}_{be}^e \tag{3.11}$$

When this expression is expanded, it is obtained that:

$$\boldsymbol{J}_2^{-1}(\boldsymbol{\Psi}_{be}^e) = \begin{bmatrix} 1 & 0 & -\mathrm{s}\theta \\ 0 & \mathrm{c}\phi & \mathrm{c}\theta\mathrm{s}\phi \\ 0 & -\mathrm{s}\phi & \mathrm{c}\theta\mathrm{c}\phi \end{bmatrix} \Rightarrow \boldsymbol{J}_2(\boldsymbol{\Psi}_{be}^e) = \begin{bmatrix} 1 & \mathrm{s}\phi\mathrm{t}\theta & \mathrm{c}\phi\mathrm{t}\theta \\ 0 & \mathrm{c}\phi & -\mathrm{s}\phi \\ 0 & \mathrm{s}\phi/\mathrm{c}\theta & \mathrm{c}\phi/\mathrm{c}\theta \end{bmatrix} \tag{3.12}$$

where $\mathrm{s}\cdot = \sin(\cdot)$, $\mathrm{c}\cdot = \cos(\cdot)$ and $\mathrm{t}\cdot = \tan(\cdot)$.

It should be noted that $\boldsymbol{J}_2(\boldsymbol{\Psi}_{be}^e)$ is undefined for $\theta = \pm 90°$ and that $\boldsymbol{J}_2(\boldsymbol{\Psi}_{be}^e)$ does not satisfy the Property 3.2.1. As a result, $\boldsymbol{J}_2^{-1}(\boldsymbol{\Psi}_{be}^e) \neq \boldsymbol{J}_2^T(\boldsymbol{\Psi}_{be}^e)$. Two possible solutions can be applied for that case. The first is switching between two Euler angle representations with different singularities that describe kinematic equations. The second is using quaternion representation.

In conclusion, the kinematic equations can be written as:

$$\begin{bmatrix} \dot{\boldsymbol{r}}_{be}^e \\ \dot{\boldsymbol{\Psi}}_{be}^e \end{bmatrix} = \begin{bmatrix} \boldsymbol{J}_1(\boldsymbol{\Psi}_{be}^e) & \mathbf{0}_{3\times3} \\ \mathbf{0}_{3\times3} & \boldsymbol{J}_2(\boldsymbol{\Psi}_{be}^e) \end{bmatrix} \begin{bmatrix} \boldsymbol{\nu}_{be}^b \\ \boldsymbol{\omega}_{be}^b \end{bmatrix} \tag{3.13}$$

3.3 Rigid Body Kinetics

6 DOF nonlinear dynamic motion equations of a rigid body can be defined in vectorial form as following [22]:

$$\boldsymbol{M}_{RB}\dot{\boldsymbol{\nu}} + \boldsymbol{C}_{RB}(\boldsymbol{\nu})\boldsymbol{\nu} = \boldsymbol{\tau}_{RB} \tag{3.14}$$

Here, $\boldsymbol{M}_{RB}$ represents the the rigid body mass matrix, $\boldsymbol{C}_{RB}$ represents the rigid body Coriolis and centripetal matrix due to the rotation of $\{b\}$ about inertial frame, which is $\{e\}$ in this study. $\boldsymbol{\tau}_{RB}$ is vector of total external forces and moments acting on the rigid body.

Newton-Euler formulation and vectorial mechanics will be used to derive the rigid body motion equations. In this scope, defining the vectors without reference to a coordinate frame is convenient. The velocity of the origin of the body frame with respect to the Earth-fixed frame is a vector $\vec{\nu}_{be}$ which is defined by its magnitude and the direction. The vector $\vec{\nu}_{be}$ decomposed in an inertial reference frame can be denoted as $\boldsymbol{\nu}^{i}_{be}$.

The following body-fixed reference points are the points wherein the motion equations will be represented:

CO: Origin o_b of the body frame

CG: Center of gravity

The position vector from CO to CG is defined as $\vec{r}_g$. This vector becomes $\vec{r}_g = \vec{0}$ if these points coincide.

3.3.1 Newton-Euler Equations of Motion about CG

Newton's second law relates mass m, acceleration $\dot{\vec{\nu}}_{gi}$ and force $\vec{f}_g$ according to:

$$m\dot{\vec{\nu}}_{gi} = \vec{f}_g \tag{3.15}$$

where $\vec{\nu}_{gi}$ is the velocity of the CG with respect to an inertial frame.

Euler's First and Second Axioms

It is possible to describe Newton's second law in terms of conservation of both linear momentum and angular momentum. These results are known as Euler's first and second axioms, respectively:

$$\frac{{}^{i}d}{dt}\vec{p}_g = \vec{f}_g \qquad \vec{p}_g = m\vec{\nu}_{gi} \tag{3.16}$$

$$\frac{{}^{i}d}{dt}\vec{h}_g = \vec{m}_g \qquad \vec{h}_g = I_g\vec{\omega}_{bi} \tag{3.17}$$

where $\vec{p}_g$ and $\vec{h}_g$ are the linear and angular momentums, $\vec{f}_g$ and $\vec{m}_g$ are the forces and moments acting on the CG point, $\vec{\nu}_{gi}$ and $\vec{\omega}_{bi}$ are the linear and angular velocities of $\{b\}$ with respect to an inertial frame, and I_g is the inertia dyadic about the CG. ${}^{i}d/dt$ is used to denote time differentiation in an inertial frame.

The main assumptions for the derivation of motion equations are that the missile is a rigid body and the Earth-fixed frame, $\{e\}$, which is defined in Section 3.2.1 is inertial. Then,

$$\vec{\nu}_{gi} \approx \vec{\nu}_{ge} \tag{3.18}$$

$$\vec{\omega}_{bi} \approx \vec{\omega}_{be} \tag{3.19}$$

The time derivative of a vector $\vec{a}$, in a moving reference frame $\{b\}$ can be expressed as:

$$\frac{{}^{i}d}{dt}\vec{a} = \frac{{}^{b}d}{dt}\vec{a} + \vec{\omega}_{bi} \times \vec{a} \tag{3.20}$$

where time differentiation in $\{b\}$ is written as:

$$\dot{\vec{a}} := \frac{{}^{b}d}{dt}\vec{a} \tag{3.21}$$

3.3.1.1 Translational Motion about CG

Since $\vec{r}_g$ is defined as the position vector from CO to CG, it can be stated that:

$$\vec{r}_{gi} = \vec{r}_{bi} + \vec{r}_g \tag{3.22}$$

Then, because of the assumption that $\{e\}$ is inertial, Equation (3.22) can be written as:

$$\vec{r}_{ge} = \vec{r}_{be} + \vec{r}_g \tag{3.23}$$

By using Equation (3.20), time differentiation of $\vec{r}_{ge}$ in a moving reference frame $\{b\}$ provides:

$$\vec{\nu}_{ge} = \vec{\nu}_{be} + (\frac{{}^{b}d}{dt}\vec{r}_g + \vec{\omega}_{be} \times \vec{r}_g) \tag{3.24}$$

The following equation can be written for a rigid body:

$$\frac{{}^{b}d}{dt}\vec{r}_g = 0 \tag{3.25}$$

such that

$$\vec{\nu}_{ge} = \vec{\nu}_{be} + \vec{\omega}_{be} \times \vec{r}_g \tag{3.26}$$

From Equation (3.16) it follows that:

$$
\begin{aligned}
\vec{f}_g &= \frac{{}^i d}{dt}(m\vec{\nu}_{gi}) \\
&= \frac{{}^i d}{dt}(m\vec{\nu}_{ge}) \\
&= \frac{{}^b d}{dt}(m\vec{\nu}_{ge}) + m\vec{\omega}_{be} \times \vec{\nu}_{ge} \\
&= m(\dot{\vec{\nu}}_{ge} + \vec{\omega}_{be} \times \vec{\nu}_{ge})
\end{aligned}
\tag{3.27}
$$

By expressing the vectors in $\{b\}$, translational motion in CG is written as:

$$
m[\dot{\boldsymbol{\nu}}_{ge}^b + \boldsymbol{S}(\boldsymbol{\omega}_{be}^b)\boldsymbol{\nu}_{ge}^b] = \boldsymbol{f}_g^b \tag{3.28}
$$

where $\boldsymbol{S}(\boldsymbol{\omega}_{be}^b)\boldsymbol{\nu}_{ge}^b = \boldsymbol{\omega}_{be}^b \times \boldsymbol{\nu}_{ge}^b$

3.3.1.2 Rotational Motion about CG

From Equation (3.17), it can be written that:

$$
\begin{aligned}
\vec{m}_g &= \frac{{}^i d}{dt}(I_g\vec{\omega}_{bi}) \\
&= \frac{{}^i d}{dt}(I_g\vec{\omega}_{be}) \\
&= \frac{{}^b d}{dt}(I_g\vec{\omega}_{be}) + \vec{\omega}_{be} \times (I_g\vec{\omega}_{be}) \\
&= I_g\dot{\vec{\omega}}_{be} - (I_g\vec{\omega}_{be}) \times \vec{\omega}_{be}
\end{aligned}
\tag{3.29}
$$

Then, the following expression is written:

$$
\boldsymbol{I}_g\dot{\boldsymbol{\omega}}_{be}^b - \boldsymbol{S}(\boldsymbol{I}_g\boldsymbol{\omega}_{be}^b)\boldsymbol{\omega}_{be}^b = \boldsymbol{m}_g^b \tag{3.30}
$$

where $\boldsymbol{S}(\boldsymbol{I}_g\boldsymbol{\omega}_{be}^b)\boldsymbol{\omega}_{be}^b = (\boldsymbol{I}_g\boldsymbol{\omega}_{be}^b) \times \boldsymbol{\omega}_{be}^b$. The definition of the inertia matrix $\boldsymbol{I}_g \in \mathbb{R}^{3\times 3}$

about CG is given as:

$$\boldsymbol{I}_g := \begin{bmatrix} I_x & -I_{xy} & -I_{xz} \\ -I_{yx} & I_y & -I_{yz} \\ -I_{zx} & -I_{zy} & I_z \end{bmatrix}, \qquad \boldsymbol{I}_g = \boldsymbol{I}_g^T > 0 \tag{3.31}$$

where I_x, I_y and I_z are the moments of inertia about the x, y, z axes of body frame, and $I_{xy} = I_{yx}, I_{xz} = I_{zx}$ and $I_{yz} = I_{zy}$ are the products of inertia defined as:

$$I_x = \int_V (y^2 + z^2)\rho_m dV; \qquad I_{xy} = \int_V xy\rho_m dV = \int_V yx\rho_m dV = I_{yx}$$

$$I_y = \int_V (x^2 + z^2)\rho_m dV; \qquad I_{xz} = \int_V xz\rho_m dV = \int_V zx\rho_m dV = I_{zx}$$

$$I_z = \int_V (x^2 + y^2)\rho_m dV; \qquad I_{yz} = \int_V yz\rho_m dV = \int_V zy\rho_m dV = I_{zy}$$

where ρ_m is the mass density of the body.

3.3.1.3 Equations of Motion about CG

The representation of the Newton-Euler equations (3.28) and (3.30) can be given in matrix form as:

$$\boldsymbol{M}_{RB}^{CG} \begin{bmatrix} \dot{\boldsymbol{\nu}}_{ge}^b \\ \dot{\boldsymbol{\omega}}_{be}^b \end{bmatrix} + \boldsymbol{C}_{RB}^{CG} \begin{bmatrix} \boldsymbol{\nu}_{ge}^b \\ \boldsymbol{\omega}_{be}^b \end{bmatrix} = \begin{bmatrix} \boldsymbol{f}_g^b \\ \boldsymbol{m}_g^b \end{bmatrix} \tag{3.32}$$

or

$$\underbrace{\begin{bmatrix} m\boldsymbol{I}_{3\times 3} & \boldsymbol{0}_{3\times 3} \\ \boldsymbol{0}_{3\times 3} & \boldsymbol{I}_g \end{bmatrix}}_{\boldsymbol{M}_{RB}^{CG}} \begin{bmatrix} \dot{\boldsymbol{\nu}}_{ge}^b \\ \dot{\boldsymbol{\omega}}_{be}^b \end{bmatrix} + \underbrace{\begin{bmatrix} m\boldsymbol{S}(\boldsymbol{\omega}_{be}^b) & \boldsymbol{0}_{3\times 3} \\ \boldsymbol{0}_{3\times 3} & -\boldsymbol{S}(\boldsymbol{I}_g\boldsymbol{\omega}_{be}^b) \end{bmatrix}}_{\boldsymbol{C}_{RB}^{CG}} \begin{bmatrix} \boldsymbol{\nu}_{ge}^b \\ \boldsymbol{\omega}_{be}^b \end{bmatrix} = \begin{bmatrix} \boldsymbol{f}_g^b \\ \boldsymbol{m}_g^b \end{bmatrix} \tag{3.33}$$

3.3.2 Newton-Euler Equations of Motion about CO

In order to formulate Newton's laws in CO, the equations of motion about CG can be transformed to CO using coordinate tranformation. It can be stated that:

$$\begin{aligned} \boldsymbol{\nu}_{ge}^{b} &= \boldsymbol{\nu}_{be}^{b} + \boldsymbol{\omega}_{be}^{b} \times \boldsymbol{r}_{g}^{b} \\ &= \boldsymbol{\nu}_{be}^{b} - \boldsymbol{r}_{g}^{b} \times \boldsymbol{\omega}_{be}^{b} \\ &= \boldsymbol{\nu}_{be}^{b} + \boldsymbol{S}^{T}(\boldsymbol{r}_{g}^{b})\boldsymbol{\omega}_{be}^{b} \end{aligned} \tag{3.34}$$

Then,

$$\begin{bmatrix} \boldsymbol{\nu}_{ge}^{b} \\ \boldsymbol{\omega}_{be}^{b} \end{bmatrix} = \boldsymbol{H}(\boldsymbol{r}_{g}^{b}) \begin{bmatrix} \boldsymbol{\nu}_{be}^{b} \\ \boldsymbol{\omega}_{be}^{b} \end{bmatrix} \tag{3.35}$$

where $\boldsymbol{r}_{g}^{b} = [x_g, y_g, z_g]^T$, is the vector from CO to CG, and $\boldsymbol{H}(\boldsymbol{r}_{g}^{b}) \in \mathbb{R}^{3\times3}$ is a transformation matrix:

$$\boldsymbol{H}(\boldsymbol{r}_{g}^{b}) := \begin{bmatrix} \boldsymbol{I}_{3\times3} & \boldsymbol{S}^{T}(\boldsymbol{r}_{g}^{b}) \\ \boldsymbol{0}_{3\times3} & \boldsymbol{I}_{3\times3} \end{bmatrix}, \qquad \boldsymbol{H}^{T}(\boldsymbol{r}_{g}^{b}) = \begin{bmatrix} \boldsymbol{I}_{3\times3} & \boldsymbol{0}_{3\times3} \\ \boldsymbol{S}(\boldsymbol{r}_{g}^{b}) & \boldsymbol{I}_{3\times3} \end{bmatrix} \tag{3.36}$$

While performing this transformation angular velocity does not change. Transforming Equation (3.32) from CG to CO using Equation (3.35) provides:

$$\boldsymbol{H}^{T}(\boldsymbol{r}_{g}^{b})\boldsymbol{M}_{RB}^{CG}\boldsymbol{H}(\boldsymbol{r}_{g}^{b}) \begin{bmatrix} \dot{\boldsymbol{\nu}}_{be}^{b} \\ \dot{\boldsymbol{\omega}}_{be}^{b} \end{bmatrix} + \boldsymbol{H}^{T}(\boldsymbol{r}_{g}^{b})\boldsymbol{C}_{RB}^{CG}\boldsymbol{H}(\boldsymbol{r}_{g}^{b}) \begin{bmatrix} \boldsymbol{\nu}_{be}^{b} \\ \boldsymbol{\omega}_{be}^{b} \end{bmatrix} = \boldsymbol{H}^{T}(\boldsymbol{r}_{g}^{b}) \begin{bmatrix} \boldsymbol{f}_{g}^{b} \\ \boldsymbol{m}_{g}^{b} \end{bmatrix} \tag{3.37}$$

Then, two new matrices are defined in CO such that:

$$\boldsymbol{M}_{RB}^{CO} := \boldsymbol{H}^{T}(\boldsymbol{r}_{g}^{b})\boldsymbol{M}_{RB}^{CG}\boldsymbol{H}(\boldsymbol{r}_{g}^{b}) \tag{3.38}$$

$$\boldsymbol{C}_{RB}^{CO} := \boldsymbol{H}^{T}(\boldsymbol{r}_{g}^{b})\boldsymbol{C}_{RB}^{CG}\boldsymbol{H}(\boldsymbol{r}_{g}^{b}) \tag{3.39}$$

When these expressions are expanded, it is obtained that:

$$\boldsymbol{M}_{RB}^{CO} = \begin{bmatrix} m\boldsymbol{I}_{3\times3} & -m\boldsymbol{S}(\boldsymbol{r}_g^b) \\ m\boldsymbol{S}(\boldsymbol{r}_g^b) & \boldsymbol{I}_g - m\boldsymbol{S}^2(\boldsymbol{r}_g^b) \end{bmatrix} \tag{3.40}$$

$$\boldsymbol{C}_{RB}^{CO} = \begin{bmatrix} m\boldsymbol{S}(\boldsymbol{\omega}_{be}^b) & -m\boldsymbol{S}(\boldsymbol{\omega}_{be}^b)\boldsymbol{S}(\boldsymbol{r}_g^b) \\ m\boldsymbol{S}(\boldsymbol{r}_g^b)\boldsymbol{S}(\boldsymbol{\omega}_{be}^b) & -\boldsymbol{S}((\boldsymbol{I}_g - m\boldsymbol{S}^2(\boldsymbol{r}_g^b))\boldsymbol{\omega}_{be}^b) \end{bmatrix} \tag{3.41}$$

where the following relationship is used:

$$m\boldsymbol{S}(\boldsymbol{r}_g^b)\boldsymbol{S}(\boldsymbol{\omega}_{be}^b)\boldsymbol{S}^T(\boldsymbol{r}_g^b)\boldsymbol{\omega}_{be}^b - \boldsymbol{S}(\boldsymbol{I}_g\boldsymbol{\omega}_{be}^b)\boldsymbol{\omega}_{be}^b \equiv \boldsymbol{S}((\boldsymbol{I}_g - m\boldsymbol{S}^2(\boldsymbol{r}_g^b))\boldsymbol{\omega}_{be}^b)\boldsymbol{\omega}_{be}^b \tag{3.42}$$

3.3.2.1 Translational Motion about CO

By using Equation (3.37) with matrices (3.40) and (3.41) the following can be written:

$$m[\dot{\boldsymbol{\nu}}_{be}^b + \boldsymbol{S}^T(\boldsymbol{r}_g^b)\dot{\boldsymbol{\omega}}_{be}^b + \boldsymbol{S}(\boldsymbol{\omega}_{be}^b)\boldsymbol{\nu}_{be}^b + \boldsymbol{S}(\boldsymbol{\omega}_{be}^b)\boldsymbol{S}^T(\boldsymbol{r}_g^b)\boldsymbol{\omega}_{be}^b] = \boldsymbol{f}_g^b \tag{3.43}$$

Because of the fact that the translational motion is independent of the point at which the external force, $\boldsymbol{f}_g^b = \boldsymbol{f}_b^b$, is applied, and using $\boldsymbol{S}^T(\boldsymbol{a})\boldsymbol{b} = -\boldsymbol{S}(\boldsymbol{a})\boldsymbol{b} = \boldsymbol{S}(\boldsymbol{b})\boldsymbol{a}$ it follows that:

$$m[\dot{\boldsymbol{\nu}}_{be}^b + \dot{\boldsymbol{\omega}}_{be}^b \times \boldsymbol{r}_g^b + \boldsymbol{\omega}_{be}^b \times \boldsymbol{\nu}_{be}^b + \boldsymbol{\omega}_{be}^b \times (\boldsymbol{\omega}_{be}^b \times \boldsymbol{r}_g^b)] = \boldsymbol{f}_b^b \tag{3.44}$$

3.3.2.2 Rotational Motion about CO

According to the parallel-axes theorem, the inertia matrix $\boldsymbol{I}_b = \boldsymbol{I}_b^T \in \mathbb{R}^{3\times3}$ about an arbitrary origin o_b is given by

$$\boldsymbol{I}_b = \boldsymbol{I}_g - m\boldsymbol{S}^2(\boldsymbol{r}_g^b) = \boldsymbol{I}_g - m(\boldsymbol{r}_g^b(\boldsymbol{r}_g^b)^T - (\boldsymbol{r}_g^b)^T\boldsymbol{r}_g^b\boldsymbol{I}_{3\times3}) \tag{3.45}$$

where the inertia matrix about the body's center of gravity is given as $\boldsymbol{I}_g = \boldsymbol{I}_g^T \in \mathbb{R}^{3\times 3}$ [28].

Using the parallel-axes theorem the lower-right elements in (3.40) and (3.41) can be rewritten:

$$\begin{aligned} \boldsymbol{I}_g + m\boldsymbol{S}(\boldsymbol{r}_g^b)\boldsymbol{S}^T(\boldsymbol{r}_g^b) &= \boldsymbol{I}_g - m\boldsymbol{S}^2(\boldsymbol{r}_g^b) \\ &= \boldsymbol{I}_b \end{aligned} \tag{3.46}$$

while the quadratic term in Equation (3.41) gives:

$$\boldsymbol{S}(\boldsymbol{r}_g^b)\boldsymbol{S}(\boldsymbol{\omega}_{be}^b)\boldsymbol{S}^T(\boldsymbol{r}_g^b)\boldsymbol{\omega}_{be}^b = -\boldsymbol{S}(\boldsymbol{\omega}_{be}^b)\boldsymbol{S}^2(\boldsymbol{r}_g^b)\boldsymbol{\omega}_{be}^b \tag{3.47}$$

such that

$$m\boldsymbol{S}(\boldsymbol{r}_g^b)\boldsymbol{S}(\boldsymbol{\omega}_{be}^b)\boldsymbol{S}^T(\boldsymbol{r}_g^b)\boldsymbol{\omega}_{be}^b + \boldsymbol{S}(\boldsymbol{\omega}_{be}^b)\boldsymbol{I}_g\boldsymbol{\omega}_{be}^b = \boldsymbol{S}(\boldsymbol{\omega}_{be}^b)\boldsymbol{I}_b\boldsymbol{\omega}_{be}^b \tag{3.48}$$

Then, the rotational motion about CO is given by the last row in Equation (3.37):

$$\boldsymbol{I}_b\dot{\boldsymbol{\omega}}_{be}^b + \boldsymbol{S}(\boldsymbol{\omega}_{be}^b)\boldsymbol{I}_b\boldsymbol{\omega}_{be}^b + m\boldsymbol{S}(\boldsymbol{r}_g^b)\dot{\boldsymbol{\nu}}_{be}^b + m\boldsymbol{S}(\boldsymbol{r}_g^b)\boldsymbol{S}(\boldsymbol{\omega}_{be}^b)\boldsymbol{\nu}_{be}^b = \boldsymbol{m}_b^b \tag{3.49}$$

where the moment about CO is

$$\begin{aligned} \boldsymbol{m}_b^b &= \boldsymbol{m}_g^b + \boldsymbol{r}_g^b \times \boldsymbol{f}_g^b \\ &= \boldsymbol{m}_g^b + \boldsymbol{S}(\boldsymbol{r}_g^b)\boldsymbol{f}_g^b \end{aligned} \tag{3.50}$$

Equation (3.49) can be rewritten as:

$$\boldsymbol{I}_b\dot{\boldsymbol{\omega}}_{be}^b + \boldsymbol{\omega}_{be}^b \times \boldsymbol{I}_b\boldsymbol{\omega}_{be}^b + m\boldsymbol{r}_g^b \times (\dot{\boldsymbol{\nu}}_{be}^b + \boldsymbol{\omega}_{be}^b \times \boldsymbol{\nu}_{be}^b) = \boldsymbol{m}_b^b \tag{3.51}$$

3.3.3 Rigid Body Equations of Motion

According to the notation of motion variables given in Section 3.2 and the definiton of $\boldsymbol{r}_g^b = [x_g, y_g, z_g]^T$, which is the distance vector from CO to CG, Equations (3.44) and (3.51) become:

$$
\begin{aligned}
m[\dot{u} - \nu r + wq - x_g(q^2 + r^2) + y_g(pq - \dot{r}) + z_g(pr + \dot{q})] &= X \\
m[\dot{v} - wp + ur - y_g(r^2 + p^2) + z_g(qr - \dot{p}) + x_g(qp + \dot{r})] &= Y \\
m[\dot{w} - uq + vp - z_g(p^2 + q^2) + x_g(rp - \dot{q}) + y_g(rq + \dot{p})] &= Z \\
I_x\dot{p} + (I_z - I_y)qr - (\dot{r} + pq)I_{xz} + (r^2 - q^2)I_{yz} + (pr - \dot{q})I_{xy} & \\
+m[y_g(\dot{w} - uq + vp) - z_g(\dot{v} - wp + ur)] &= L \\
I_y\dot{q} + (I_x - I_z)rp - (\dot{p} + qr)I_{xy} + (p^2 - r^2)I_{zx} + (qp - \dot{r})I_{yz} & \\
+m[z_g(\dot{u} - vr + wq) - x_g(\dot{w} - uq + vp)] &= M \\
I_z\dot{r} + (I_y - I_x)pq - (\dot{q} + rp)I_{yz} + (q^2 - p^2)I_{xy} + (rq - \dot{p})I_{zx} & \\
+m[x_g(\dot{v} - wp + ur) - y_g(\dot{u} - vr + wq)] &= N
\end{aligned}
\tag{3.52}
$$

Here, the first three equations are related with the translational motion and the last three equations are related with the rotational motion.

Vectorial Representation

It was stated in Equation (3.14) that the rigid body kinetics can be described in vector form as:

$$\boldsymbol{M}_{RB}\dot{\boldsymbol{\nu}} + \boldsymbol{C}_{RB}(\boldsymbol{\nu})\boldsymbol{\nu} = \boldsymbol{\tau}_{RB}$$

The rigid body system inertia matrix $\boldsymbol{M}_{RB}$ is unique and satisfies

$$\boldsymbol{M}_{RB} = \boldsymbol{M}_{RB}^T > 0, \qquad \dot{\boldsymbol{M}}_{RB} = \boldsymbol{0}_{6\times 6} \tag{3.53}$$

where

$$
\begin{aligned}
\boldsymbol{M}_{RB} &= \begin{bmatrix} m\boldsymbol{I}_{3\times 3} & -m\boldsymbol{S}(\boldsymbol{r}_g^b) \\ m\boldsymbol{S}(\boldsymbol{r}_g^b) & \boldsymbol{I}_b \end{bmatrix} \\
&= \begin{bmatrix} m & 0 & 0 & 0 & mz_g & -my_g \\ 0 & m & 0 & -mz_g & 0 & mx_g \\ 0 & 0 & m & my_g & -mx_g & 0 \\ 0 & -mz_g & my_g & I_x & -I_{xy} & -I_{xz} \\ mz_g & 0 & -mx_g & -I_{yx} & I_y & -I_{yz} \\ -my_g & mx_g & 0 & -I_{zx} & -I_{zy} & I_z \end{bmatrix}
\end{aligned}
\tag{3.54}
$$

The matrix $\boldsymbol{C}_{RB}$ in Equation (3.14) is related to the Coriolis vector term $\boldsymbol{\omega}_{be}^b \times \boldsymbol{\nu}_{be}^b$ and the centripetal vector term $\boldsymbol{\omega}_{be}^b \times (\boldsymbol{\omega}_{be}^b \times \boldsymbol{r}_g^b)$. $\boldsymbol{C}_{RB}$ can be defined as:

$$
\boldsymbol{C}_{RB}(\boldsymbol{\nu}) = \left[\begin{matrix} 0 & 0 & 0 \\ 0 & 0 & 0 \\ 0 & 0 & 0 \\ -m(y_g q + z_g r) & m(y_g p + w) & m(z_g p - v) \\ m(x_g q - w) & -m(z_g r + x_g p) & m(z_g q + u) \\ m(x_g r + v) & m(y_g r - u) & -m(x_g p + y_g q) \end{matrix}\right.
$$
$$
\left.\begin{matrix} m(y_g q + z_g r) & -m(x_g q - w) & -m(x_g r + v) \\ -m(y_g p + w) & m(z_g r + x_g p) & -m(y_g r - u) \\ -m(z_g p - v) & -m(z_g q + u) & m(x_g p + y_g q) \\ 0 & -I_{yz} q - I_{xz} p + I_z r & I_{yz} r + I_{xy} p - I_y q \\ I_{yz} q + I_{xz} p - I_z r & 0 & -I_{xz} r - I_{xy} q + I_x p \\ -I_{yz} r - I_{xy} p + I_y q & I_{xz} r + I_{xy} q - I_x p & 0 \end{matrix}\right]
\tag{3.55}
$$

When the origin CO coincides with CG, this results with $\boldsymbol{r}_g^b = [0,0,0]^T$, $\boldsymbol{I}_b = \boldsymbol{I}_g$. Moreover, if the body axes (x_b, y_b, z_b) coincide with the principal axes of inertia, then, $\boldsymbol{I}_g = diag\{I_x^{cg}, I_y^{cg}, I_z^{cg}\}$. With these assumptions, the matrices $\boldsymbol{M}_{RB}$ and $\boldsymbol{C}_{RB}$ are simplifed as below:

$$
\begin{aligned}
\boldsymbol{M}_{RB} &= \begin{bmatrix} m\boldsymbol{I}_{3\times3} & \mathbf{0}_{3\times3} \\ \mathbf{0}_{3\times3} & \boldsymbol{I}_g \end{bmatrix} \\
&= \begin{bmatrix} m & 0 & 0 & 0 & 0 & 0 \\ 0 & m & 0 & 0 & 0 & 0 \\ 0 & 0 & m & 0 & 0 & 0 \\ 0 & 0 & 0 & I_x & 0 & 0 \\ 0 & 0 & 0 & 0 & I_y & 0 \\ 0 & 0 & 0 & 0 & 0 & I_z \end{bmatrix}
\end{aligned} \tag{3.56}
$$

$$
\boldsymbol{C}_{RB}(\boldsymbol{\nu}) = \begin{bmatrix} 0 & 0 & 0 & 0 & mw & -mv \\ 0 & 0 & 0 & -mw & 0 & mu \\ 0 & 0 & 0 & mv & -mu & 0 \\ 0 & mw & -mv & 0 & I_z r & -I_y q \\ -mw & 0 & mu & -I_z r & 0 & I_x p \\ mv & -mu & 0 & I_y q & -I_x p & 0 \end{bmatrix} \tag{3.57}
$$

3.4 Aerodynamic and Hydrodynamic Forces and Moments

In [23], it is stated that a commonly used assumption in hydrodynamics is that there are two main sources of hydrodynamic forces and moments which are "Radiation-Induced Forces" and "Froude-Kriloff and Diffraction Forces". While the former is generated when the body oscillates with wave excitation frequency in the absence of incident waves, sources of the latter are environmental disturbances such as ocean currents, waves, and wind. In the scope of this study, the environmental disturbances are neglected for both underwater and air motion. Then, radiation-induced forces can be considered as the only force and moment generating factor for hydrodynamics.

Three factors can be considered as the sources of radiation-induced forces:

(1) Added mass due to the inertia of the surrounding fluid,

(2) Hydrodynamic damping,

(3) Gravitational and buoyancy forces.

These components are described and mathematically expressed in the following sections. Hydrodynamic damping will be represented together with aerodynamic forces and moments in Section 3.4.2.

3.4.1 Added Mass and Inertia

The motion of a rigid body in fluid results with that the fluid surrounding the body is accelerated together with the body. As a result of this, a force is needed to achieve this acceleration where the fluid reacts with a force that is equal in magnitude and opposite in direction. This reaction force is named as added mass contribution. The hydrodynamic added mass force along x_b-axis as a result of linear acceleration $\dot{u}$ in the x_b direction is written as [29]:

$$X_A = -X_{\dot{u}}\dot{u}, \qquad where \quad X_{\dot{u}} = \frac{\partial X}{\partial \dot{u}} \tag{3.58}$$

Using the same approach, all added mass elements which relate the force and moment components to the linear and angular accelerations can be found. Then, all these elements can be written in an (6x6) inertia matrix, which is also named as the added mass matrix, $\boldsymbol{M}_A \in \mathbb{R}^{6\times 6}$ as:

$$\boldsymbol{M}_A = -\begin{bmatrix} X_{\dot{u}} & X_{\dot{v}} & X_{\dot{w}} & X_{\dot{p}} & X_{\dot{q}} & X_{\dot{r}} \\ Y_{\dot{u}} & Y_{\dot{v}} & Y_{\dot{w}} & Y_{\dot{p}} & Y_{\dot{q}} & Y_{\dot{r}} \\ Z_{\dot{u}} & Z_{\dot{v}} & Z_{\dot{w}} & Z_{\dot{p}} & Z_{\dot{q}} & Z_{\dot{r}} \\ K_{\dot{u}} & K_{\dot{v}} & K_{\dot{w}} & K_{\dot{p}} & K_{\dot{q}} & K_{\dot{r}} \\ M_{\dot{u}} & M_{\dot{v}} & M_{\dot{w}} & M_{\dot{p}} & M_{\dot{q}} & M_{\dot{r}} \\ N_{\dot{u}} & N_{\dot{v}} & N_{\dot{w}} & N_{\dot{p}} & N_{\dot{q}} & N_{\dot{r}} \end{bmatrix} \tag{3.59}$$

Since the added mass properties are related to the body's geometry, some properties may be held. In this work, since the missile's underwater configuration have symmetries in the xy-plane and xz-plane of body frame, $\boldsymbol{M}_A$ reduces to [30]:

$$\boldsymbol{M}_A \triangleq - \begin{bmatrix} X_{\dot{u}} & 0 & 0 & 0 & 0 & 0 \\ 0 & Y_{\dot{v}} & 0 & 0 & 0 & Y_{\dot{r}} \\ 0 & 0 & Z_{\dot{w}} & 0 & Z_{\dot{q}} & 0 \\ 0 & 0 & 0 & K_{\dot{p}} & 0 & 0 \\ 0 & 0 & M_{\dot{w}} & 0 & M_{\dot{q}} & 0 \\ 0 & N_{\dot{v}} & 0 & 0 & 0 & N_{\dot{r}} \end{bmatrix} \tag{3.60}$$

The added mass also has an added Coriolis and centripetal contribution [29]. For a rigid body moving in an ideal fluid the hydrodynamic Coriolis and centripetal matrix $\boldsymbol{C}_A(\boldsymbol{\nu})$ can be written as:

$$\boldsymbol{C}_A(\boldsymbol{\nu}) = \begin{bmatrix} 0 & 0 & 0 & 0 & -a_3 & a_2 \\ 0 & 0 & 0 & a_3 & 0 & -a_1 \\ 0 & 0 & 0 & -a_2 & a_1 & 0 \\ 0 & -a_3 & a_2 & 0 & -b_3 & b_2 \\ a_3 & 0 & -a_1 & b_3 & 0 & -b_1 \\ -a_2 & a_1 & 0 & -b_2 & b_1 & 0 \end{bmatrix} \tag{3.61}$$

where

$$\begin{aligned} a_1 &= X_{\dot{u}}u + X_{\dot{v}}v + X_{\dot{w}}w + X_{\dot{p}}p + X_{\dot{q}}q + X_{\dot{r}}r \\ a_2 &= Y_{\dot{u}}u + Y_{\dot{v}}v + Y_{\dot{w}}w + Y_{\dot{p}}p + Y_{\dot{q}}q + Y_{\dot{r}}r \\ a_3 &= Z_{\dot{u}}u + Z_{\dot{v}}v + Z_{\dot{w}}w + Z_{\dot{p}}p + Z_{\dot{q}}q + Z_{\dot{r}}r \\ b_1 &= K_{\dot{u}}u + K_{\dot{v}}v + K_{\dot{w}}w + K_{\dot{p}}p + K_{\dot{q}}q + K_{\dot{r}}r \\ b_2 &= M_{\dot{u}}u + M_{\dot{v}}v + M_{\dot{w}}w + M_{\dot{p}}p + M_{\dot{q}}q + M_{\dot{r}}r \\ b_3 &= N_{\dot{u}}u + N_{\dot{v}}v + N_{\dot{w}}w + N_{\dot{p}}p + N_{\dot{q}}q + N_{\dot{r}}r \end{aligned} \tag{3.62}$$

Since the missile's underwater configuration have symmetries in the xy-plane and

xz-plane of body frame, a_i, b_i parameters for $i = 1, 2, 3$ and $\boldsymbol{C}_A(\boldsymbol{\nu})$ reduce to:

$$\begin{aligned}
a_1 &= X_{\dot{u}} u \\
a_2 &= Y_{\dot{v}} v + Y_{\dot{r}} r \\
a_3 &= Z_{\dot{w}} w + Z_{\dot{q}} q \\
b_1 &= K_{\dot{p}} p \\
b_2 &= M_{\dot{w}} w + M_{\dot{q}} q \\
b_3 &= N_{\dot{v}} v + N_{\dot{r}} r
\end{aligned} \tag{3.63}$$

$$\boldsymbol{C}_A(\boldsymbol{\nu}) = \begin{bmatrix}
0 & 0 & 0 & 0 & -(Z_{\dot{w}} w + Z_{\dot{q}} q) & Y_{\dot{v}} v + Y_{\dot{r}} r \\
0 & 0 & 0 & Z_{\dot{w}} w + Z_{\dot{q}} q & 0 & -X_{\dot{u}} u \\
0 & 0 & 0 & -(Y_{\dot{v}} v + Y_{\dot{r}} r) & X_{\dot{u}} u & 0 \\
0 & -(Z_{\dot{w}} w + Z_{\dot{q}} q) & Y_{\dot{v}} v + Y_{\dot{r}} r & 0 & -(N_{\dot{v}} v + N_{\dot{r}} r) & M_{\dot{w}} w + M\dot{q} q \\
Z_{\dot{w}} w + Z_{\dot{q}} q & 0 & -(X_{\dot{u}} u) & N_{\dot{v}} v + N_{\dot{r}} r & 0 & -K_{\dot{p}} p \\
-(Y_{\dot{v}} v + Y_{\dot{r}} r) & X_{\dot{u}} u & 0 & -(M_{\dot{w}} w + M\dot{q} q) & K_{\dot{p}} p & 0
\end{bmatrix} \tag{3.64}$$

In conclusion, the rigid body kinetics which is given in Equation (3.14) can be rewritten as:

$$\boldsymbol{M}\dot{\boldsymbol{\nu}} + \boldsymbol{C}(\boldsymbol{\nu})\boldsymbol{\nu} = \boldsymbol{\tau}_{RB} \tag{3.65}$$

where

$$\boldsymbol{M} \triangleq \boldsymbol{M}_{RB} + \boldsymbol{M}_A; \qquad \boldsymbol{C}(\boldsymbol{\nu}) \triangleq \boldsymbol{C}_{RB}(\boldsymbol{\nu}) + \boldsymbol{C}_A(\boldsymbol{\nu}) \tag{3.66}$$

It should be noted that the $\boldsymbol{M}_A$ and $\boldsymbol{C}_A(\boldsymbol{\nu})$ matrices are equated to zero for the missile's motion in air.

3.4.2 Representation of Aerodynamic and Hydrodynamic Forces and Moments

The contributions of aerodynamic and hydrodynamic forces and moments can be represented in vectorial form as:

$$\boldsymbol{\tau}_{A/H} = \begin{bmatrix} QAC_x \\ QAC_y \\ QAC_z \\ QAdC_l \\ QAdC_m \\ QAdC_n \end{bmatrix} \tag{3.67}$$

where C_x, C_y, C_z are force coefficients, C_l, C_m, C_n are moment coefficients, Q is dynamic pressure, A is reference area, d is reference length. Dynamic pressure is defined as:

$$Q = \frac{1}{2}\rho V^2 \tag{3.68}$$

where V is the magnitude of the total velocity of the missile and can be found by the formula:

$$V = \sqrt{u^2 + v^2 + w^2} \tag{3.69}$$

ρ is the water or air density. According to the International Standard Atmosphere model and assuming that the sea level is at 0-meter altitude and the upper altitude limit is 20000 meters, ρ can be calculated as:

$$\rho = \left\{ \begin{matrix} \rho_{water} & for & h < 0m \\ \rho_{air}(\frac{T}{T_0})^{(\frac{g}{LR}-1)} & for & 0 \leq h \leq 11000m \\ \rho_{air}(\frac{T}{T_0})^{(\frac{g}{LR}-1)} e^{(\frac{g}{RT}(11000-h))} & for & h > 11000m \end{matrix} \right\} \tag{3.70}$$

where ρ_{water} is sea water density ($1023kg/m^3$), T is ambient temperature given with Equation (3.75), ρ_{air} is air density at sea level ($1.225kg/m^3$), T_0 is absolute temperature at mean sea level ($288.15K$), g is acceleration due to gravity ($9.80665m/s^2$), L is lapse rate ($0.0065K/m$), R is characteristic gas constant ($287.0531J.kg^{-1}.K^{-1}$) and h is altitude.

Before describing the force and moment coefficients in detail, some flight parameters should be defined. Two of these parameters; angle of attack, α, and sideslip angle, β, are shown in Figure 3.4. Angle of attack and sideslip angle are used to represent the angular relationship between the total velocity vector $\boldsymbol{V}_T$ and the body frame. They are defined as:

$$\alpha = \tan^{-1}\left(\frac{w}{u}\right) \tag{3.71}$$

$$\beta = \sin^{-1}\left(\frac{v}{V}\right) \tag{3.72}$$

Another important flight parameter is Mach number, which is a relative representation of the total velocity with respect to the speed of sound. It can be defined as:

$$M = \frac{V}{C} \tag{3.73}$$

where C is speed of sound. Speed of sound can be defined as:

$$C = \sqrt{\gamma R T} \tag{3.74}$$

where γ is the specific heat ratio of air, which is 1.4 and T is the ambient temperature.

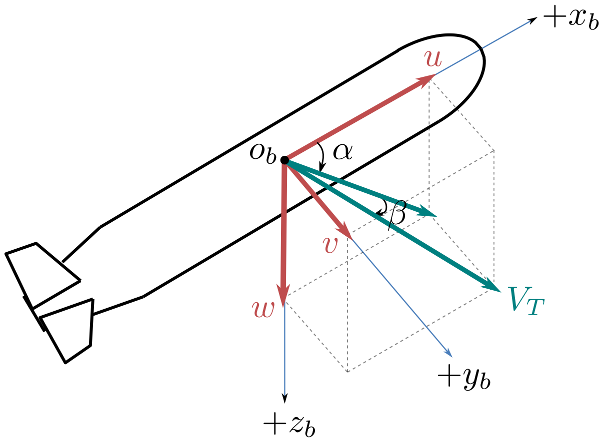

Figure 3.4: Angle of attack (α) and sideslip angle (β)

Using International Standard Atmoshpere Model, given that the altitude is between 0-20000 meters range, ambient temperature is:

$$T = \begin{Bmatrix} T_0 - Lh & for \quad h \leq 11000m \\ T_0 - 11000h & for \quad h > 11000m \end{Bmatrix} \tag{3.75}$$

In this study, when it is needed to represent the missile's underwater velocity in terms of Mach number, speed of sound at sea level will be used.

In practice, force coefficients C_x, C_y, C_z and moment coefficients C_l, C_m, C_n may depend on different flight parameters such as α, $\dot{\alpha}$, β, $\dot{\beta}$, Mach, angular velocities (p, q, r) or aileron, elevator, and rudder surface deflections $(\delta_a, \delta_e, \delta_r)$ [31], and can be defined as a nonlinear function of these parameters as:

$$C_i = C_i(M, \alpha, \beta, \delta_a, \delta_e, \delta_r, p, q, r, \dot{\alpha}, \dot{\beta}) \qquad for \quad i = x, y, z, l, m, n \tag{3.76}$$

The commonly used tools for calculation of force and moment coefficients do not provide the explicit nonlinear functions for the coefficients. Thus, in order to develop a 6 DOF nonlinear simulation environment by using the obtained database from these tools, dependencies of the coefficients on flight parameters can be represented by superposition. Moreover, for control design studies where the equations of motion will be linearized or simplified as it is possible, force and moment coefficients are also simplified with this representation which is constructed with superposition. This representation is given as following:

$$
\begin{aligned}
C_i = C_i(M, \alpha, \beta, \delta_a, \delta_e, \delta_r, p, q, r, \dot{\alpha}, \dot{\beta}) = C_{i0}(\beta, M, \alpha) + C_{i\delta_a}(\beta, M, \alpha)\delta_a + \\
C_{i\delta_e}(\beta, M, \alpha)\delta_e + C_{i\delta_r}(\beta, M, \alpha)\delta_r + \\
C_{ip}(\beta, M, \alpha)p\frac{d}{2V} + C_{iq}(\beta, M, \alpha)q\frac{d}{2V} + C_{ir}(\beta, M, \alpha)r\frac{d}{2V} \\
for \qquad i = x, y, z, l, m, n
\end{aligned}
\tag{3.77}
$$

The dynamic derivatives are multiplied by $\frac{d}{2V}$ in order to make the final product dimensionless. Aerodynamic/hydrodynamic derivatives can be expressed as following:

$$
C_{ij} = \frac{\partial C_i}{\partial j}|_{j=j_0} \qquad j = \alpha, \beta, \delta_a, \delta_e, \delta_r, p, q, r \tag{3.78}
$$

In this study, Missile DATCOM software will be used in the next chapter to calculate force and moment coefficients. This tool provides a tabulated coefficient database for predefined values of angle of attack, sideslip angle, Mach number and control surface deflections. Thus, in accordance with the generated database by Missile DATCOM, for a specific $(\beta_0, \delta_0, M_0, \alpha_0)$ point of the database, non-dimensional form of forces and moment coefficients, for decoupled longitudinal and lateral motion can be written in linear form as:

$$
\begin{aligned}
C_x &= C_{x\alpha}\alpha + C_{x\delta_e}\delta_e + C_{xq}q\frac{d}{2V} \\
C_y &= C_{y\beta}\beta + C_{y\delta_a}\delta_a + C_{y\delta_r}\delta_r + C_{yp}p\frac{d}{2V} + C_{yr}r\frac{d}{2V} \\
C_z &= C_{z\alpha}\alpha + C_{z\delta_e}\delta_e + C_{zq}q\frac{d}{2V} \\
C_l &= C_{l\beta}\beta + C_{l\delta_a}\delta_a + C_{l\delta_r}\delta_r + C_{lp}p\frac{d}{2V} + C_{lr}r\frac{d}{2V} \\
C_m &= C_{m\alpha}\alpha + C_{m\delta_e}\delta_e + C_{mq}q\frac{d}{2V} \\
C_n &= C_{n\beta}\beta + C_{n\delta_a}\delta_a + C_{n\delta_r}\delta_r + C_{np}p\frac{d}{2V} + C_{nr}r\frac{d}{2V}
\end{aligned}
\tag{3.79}
$$

3.5 Gravitational and Buoyancy Forces and Moments

The gravitational and buoyancy forces are called restoring forces in hydrostatic terminology. Then, through this study $\boldsymbol{\tau}_R$ will be used to denote restoring forces. The procedure in [24] to derive this force and moment contribution can be followed here. Let the gravitational force $\boldsymbol{f}_g^b$ acts through the center of gravity (CG) defined by the vector $\boldsymbol{r}_g^b := [x_g, y_g, z_g]^T$ with respect to the center of the body frame (CO) and the buoyancy force $\boldsymbol{f}_b^b$ acts through the center of buoyancy (CB) defined by the vector $\boldsymbol{r}_b^b := [x_b, y_b, z_b]^T$. Both vectors are referred to the body-fixed reference point CO.

Let m be the mass of the missile, ∇ the volume of fluid displaced by the missile, g the acceleration of gravity (along the z-axis of the Earth-fixed frame) and ρ_{water} is the sea water density. Then, the submerged weight of the body, W, and buoyancy force, B, can be written as:

$$
W = mg, \qquad B = \rho_{water} g \nabla \tag{3.80}
$$

These forces act in the vertical plane of the Earth-fixed frame. Hence,

$$\boldsymbol{f}_g^e = \begin{bmatrix} 0 \\ 0 \\ W \end{bmatrix} \qquad and \qquad \boldsymbol{f}_b^e = -\begin{bmatrix} 0 \\ 0 \\ B \end{bmatrix} \tag{3.81}$$

Using the transformation matrix given in Equation (3.9), gravitational and buoyancy force in the body frame can be written as:

$$\begin{aligned} \boldsymbol{f}_g^b &= \boldsymbol{J}_1(\boldsymbol{\Psi}_{be}^e)^{-1}\boldsymbol{f}_g^e \\ \boldsymbol{f}_b^b &= \boldsymbol{J}_1(\boldsymbol{\Psi}_{be}^e)^{-1}\boldsymbol{f}_b^e \end{aligned} \tag{3.82}$$

Then, restoring force and moment in the body frame can be expressed in vectorial form as:

$$\begin{aligned} \boldsymbol{\tau}_R &= \begin{bmatrix} \boldsymbol{f}_g^b + \boldsymbol{f}_b^b \\ \boldsymbol{r}_g^b \times \boldsymbol{f}_g^b + \boldsymbol{r}_b^b \times \boldsymbol{f}_b^b \end{bmatrix} \\ &= \begin{bmatrix} \boldsymbol{J}_1(\boldsymbol{\Psi}_{be}^e)^{-1}(\boldsymbol{f}_g^e + \boldsymbol{f}_b^e) \\ \boldsymbol{r}_g^b \times \boldsymbol{J}_1(\boldsymbol{\Psi}_{be}^e)^{-1}\boldsymbol{f}_g^e + \boldsymbol{r}_b^b \times \boldsymbol{J}_1(\boldsymbol{\Psi}_{be}^e)^{-1}\boldsymbol{f}_b^e \end{bmatrix} \end{aligned} \tag{3.83}$$

Expanding this expression yields

$$\boldsymbol{\tau}_R = \begin{bmatrix} (B-W)\sin(\theta) \\ (W-B)\cos(\theta)\sin(\phi) \\ (W-B)\cos(\theta)\cos(\phi) \\ (y_gW - y_bB)\cos(\theta)\cos(\phi) - (z_gW - z_bB)\cos(\theta)\sin(\phi) \\ -(z_gW - z_bB)\sin(\theta) - (x_gW - x_bB)\cos(\theta)\cos(\phi) \\ (x_gW - x_bB)\cos(\theta)\sin(\phi) + (y_gW - y_bB)\sin(\theta) \end{bmatrix} \tag{3.84}$$

When the origin CO coincides with CG, this implies that $\boldsymbol{r}_g^b = [0,0,0]^T$. Moreover, according to the information provided about the missile physical properties in Section

2.5 , $\boldsymbol{r}_b^b := [x_b, 0, 0]^T$. Then, restoring force and moment vector takes the following form:

$$\boldsymbol{\tau}_R = \begin{bmatrix} (B-W)\sin(\theta) \\ (W-B)\cos(\theta)\sin(\phi) \\ (W-B)\cos(\theta)\cos(\phi) \\ 0 \\ x_b B\cos(\theta)\cos(\phi) \\ -x_b B\cos(\theta)\sin(\phi) \end{bmatrix} \tag{3.85}$$

3.6 Thrust Forces and Moments

The thrust forces and moments which act on the missile body are produced by a booster motor and cruise engine which are detailed in Chapter 2. During the launch and boost phases of the flight, the booster motor provides the thrust forces and moments. Having jettisoned the booster motor, a cruise engine is used to obtain desired thrust force in cruise and terminal phases. Firstly, considering the booster motor propulsion, force and moment vector $\boldsymbol{\tau}_T$ can be defined as:

$$\boldsymbol{\tau}_T = [\boldsymbol{\tau}_{T1}^T, \boldsymbol{\tau}_{T2}^T]^T \tag{3.86}$$

where

$$\boldsymbol{\tau}_1 = \begin{bmatrix} T\cos(\theta_T)\cos(\psi_T) \\ T\sin(\psi_T) \\ -T\sin(\theta_T)\cos(\psi_T) \end{bmatrix} \tag{3.87}$$

Here, T is total thrust, θ_T is thrust deflection in pitch plane and ψ_T is thrust deflection in yaw plane. The application of $\boldsymbol{\tau}_1$ on the missile body is shown in Figure 2.3

Moment term, $\boldsymbol{\tau}_2$, of $\boldsymbol{\tau}_T$ can be defined as:

$$
\begin{aligned}
\boldsymbol{\tau}_2 &= \boldsymbol{l}_T \times \tau_1 \\
&= \begin{bmatrix} 0 & -l_z & l_y \\ l_z & 0 & -l_x \\ -l_y & l_x & 0 \end{bmatrix} \boldsymbol{\tau}_1 \\
&= \begin{bmatrix} -Tl_y \sin(\theta_T)\cos(\psi_T) - Tl_z \sin(\psi_T) \\ Tl_z \cos(\theta_T)\cos(\psi_T) + Tl_x \sin(\theta_T)\cos(\psi_T) \\ -Tl_y \cos(\theta_T)\cos(\psi_T) + Tl_x \sin(\psi_T) \end{bmatrix}
\end{aligned}
\tag{3.88}
$$

where l_x, l_y, l_z are the components of $\boldsymbol{l}_T$, which is the moment arm of booster thrust vector. If it is assumed that the thrust is applied at a point of x_b axis of the body frame, then $\boldsymbol{l}_T = [l_x, 0, 0]$. Moreover, since the allowed θ_T and ψ_T will be small, the resulting thrust force and moment vector can be simplified as:

$$
\boldsymbol{\tau}_T = \begin{bmatrix} T \\ T\psi_T \\ -T\theta_T \\ 0 \\ Tl_x\theta_T \\ Tl_x\psi_T \end{bmatrix} \tag{3.89}
$$

It should be noted that the given expression for $\boldsymbol{\tau}_T$ can also be used to model the cruise engine's thrust forces and moments. However, assuming the ideal case, since there will not be a thrust deflection for the cruise engine, θ_T and ψ_T will be zero. Thus, in the case that the cruise engine thrust is applied at a point of x_b axis of the body frame, which is the case in this study, $\boldsymbol{\tau}_2$ will be zero and the cruise engine only generates a force in the x_b axis.

3.7 Conclusion

So far in this chapter, having derived the 6 DOF nonlinear rigid body equations of motion, the forces and moments which act on the missile body were defined. Then, the rigid body kinetics given in Equation (3.14), can be described for the missile in this work as:

$$\boldsymbol{M}\dot{\boldsymbol{\nu}} + \boldsymbol{C}(\boldsymbol{\nu})\boldsymbol{\nu} = \boldsymbol{\tau}_{A/H} + \boldsymbol{\tau}_T + \boldsymbol{\tau}_R \tag{3.90}$$

where $\boldsymbol{M}$ and $\boldsymbol{C}$ are the total rigid body mass matrix and the total rigid body Coriolis and centripetal matrix where both of them also include added mass terms. $\boldsymbol{\tau}_{A/H}$, $\boldsymbol{\tau}_T$ and $\boldsymbol{\tau}_R$ are aerodynamic/hydrodynamic, thrust and restoring forces and moment vectors. The explicit definitions of these parameters were given previously in the corresponding sections.

CHAPTER 4

DERIVATION OF HYDRODYNAMIC AND AERODYNAMIC PARAMETERS

4.1 Introduction

Having expressed the aerodynamic and hydrodynamic forces and moments in Chapter 3, numerical values of hydrodynamic and aerodynamic parameters that are involved in these expressions should be derived. For this purpose, added mass parameters and hydrodynamic/aerodynamic force and moment coefficients are calculated in this chapter.

4.2 Added Mass Parameters

The added mass parameters are the parameters which are included in the added mass matrix and Coriolis and centripetal matrix related to added mass effect. Due to the simplifications of these matrices because of the physical properties of the missile, the parameters to be found reduce to $X_{\dot{u}}$, $Y_{\dot{v}}$, $Y_{\dot{r}}$, $Z_{\dot{w}}$, $Z_{\dot{q}}$, $K_{\dot{p}}$, $M_{\dot{w}}$, $M_{\dot{q}}$, $N_{\dot{v}}$, $N_{\dot{r}}$.

Axial added mass parameter, $X_{\dot{u}}$, can be estimated with the procedure followed in [30]. In this method, the missile shape in Flight Mode 1 is approximated by an ellipsoid. Then, the axial added mass of an ellipsoid can be found as [32]:

$$X_{\dot{u}} = -\gamma\left(\frac{4}{3}\right)\rho_{water}\pi\left(\frac{l_m}{2}\right)\left(\frac{d_m}{2}\right)^2 \tag{4.1}$$

where l_m is the missile length, d_m is the missile diameter and γ is an empirical parameter whose value depends on the ratio of the missile length to diameter. This relationship is given in Table 4.1 [32].

l_m/d_m	0.01	0.1	0.2	0.4	0.6	0.8	1.0
γ	-	6.148	3.008	1.428	0.9078	0.6514	0.5000
l_m/d_m	1.5	2.0	2.5	3.0	5.0	7.0	10.0
γ	0.3038	0.2100	0.1563	0.1220	0.05912	0.03585	0.02071

Table 4.1: γ for axial added mass parameter calculation

Physical parameters of the first flight mode provide $l_m/d_m = 6.1806/0.5175 = 11.9432$ ratio. Although the upper limit of l_m/d_m ratio in Table 4.1 is 10.0, by using linear extrapolation, γ can be estimated as 0.0119. Then, $X_{\dot{u}}$ is found as:

$$X_{\dot{u}} = -0.0119\left(\frac{4}{3}\right)1023\pi\left(\frac{6.1806}{2}\right)\left(\frac{0.5175}{2}\right)^2 = -10.5294 \tag{4.2}$$

Rolling added mass parameter, $K_{\dot{p}}$, can be assumed to be zero since the physical configuration in underwater has no fin or another control surface on the cylindrical shape of the missile.

$$K_{\dot{p}} \approx 0 \tag{4.3}$$

Remaining added mass parameters can be found using strip theory. This theory is based on computing 2-D hydrodynamic coefficients for added mass for each strip of a body and then summing over the length of the body to obtain the 3-D coefficients [24]. The added mass per unit length of a single cylindrical slice can be calculated as [33]:

$$m_a(x) = \pi\rho_{water}r^2(x) \tag{4.4}$$

where $r(x)$ is the radius of the missile as a function of the length, which is given in Equation (2.1). According to this definition and using the symmetry properties of the missile, added mass parameters can be calculated as below [30]:

$$
\begin{aligned}
Y_{\dot{v}} &= -\int_{tail}^{nose} m_a(x)dx \\
Z_{\dot{w}} &= Y_{\dot{v}} \\
M_{\dot{w}} &= -\int_{tail}^{nose} x m_a(x)dx \\
N_{\dot{v}} &= -M_{\dot{w}} \\
Y_{\dot{r}} &= N_{\dot{v}} \\
Z_{\dot{q}} &= M_{\dot{w}} \\
M_{\dot{q}} &= -\int_{tail}^{nose} x^2 m_a(x)dx \\
N_{\dot{r}} &= M_{\dot{q}}
\end{aligned}
\tag{4.5}
$$

As a result, all the calculated added mass parameters are given in Table 4.2.

Parameter	Value	Unit
$X_{\dot{u}}$	-10.5294	kg
$Y_{\dot{v}}$	-1296.5	kg
$Y_{\dot{r}}$	-99.4382	kgm/rad
$Z_{\dot{w}}$	-1296.5	kg
$Z_{\dot{q}}$	99.4382	kgm/rad
$K_{\dot{p}}$	0	kgm^2/rad
$M_{\dot{w}}$	99.4382	kgm
$M_{\dot{q}}$	-3936.7	kgm^2/rad
$N_{\dot{v}}$	-99.4382	kgm
$N_{\dot{r}}$	-3936.7	kgm^2/rad

Table 4.2: Added mass parameters

4.3 Hydrodynamic and Aerodynamic Force and Moment Coefficients

During the design of marine or air vehicles, different methods are used to obtain force and moment coefficients. In the preliminary phases of the design, where it may be needed to estimate coefficients quickly and economically with a predictive accuracy, usually, computer programs can be utilized. For the further design phases, where it is needed to achieve more accurate values of the coefficients, some methods which are based on experiments such as wind tunnel tests or system identification can be used. In this thesis, Missile DATCOM software is used to obtain non-dimensional force and moment coefficients of the missile's different configuration for three different flight modes [34].

Mainly two sets of inputs are provided to Missile DATCOM. While the first set describes the physical properties of the missile, the second set defines the flight conditions at which the coefficients are calculated. These conditions are discrete values of angle of attack, sideslip angle, and Mach number. They can be considered as the samples of possible flight envelope of the missile. In addition to them, for the second and third flight modes where the tail fins are deployed and used to generate control surface deflections; elevator, rudder and aileron deflections are provided as inputs. In Table 4.3 these flight conditions including control surface deflections are given.

Some of the coefficients can be considered as more critical for flight control than the others since they are directly related to the stability and control effectiveness [35]. Thus, the change of some of the important non-dimensional force and moment coefficients with respect to the flight conditions is given in Appendix A.

Flight Mode	Flight Variable	Values	Unit
1	α	$\pm\{0, 2, 4, 6, 8, 10, 15, 20, 25, 30, 35,$ $40, 50, 60, 70, 90, 110, 130, 150\}$	deg
	β	$\pm\{0, 5\}$	deg
	$Mach$	$\{0.02, 0.06, 0.1, 0.15, 0.2\}$	
2	α	$\pm\{0, 2, 4, 6, 8, 10, 15,$ $20, 25, 30, 35, 40\}$	deg
	β	$\pm\{0, 5\}$	deg
	$Mach$	$\{0.1, 0.2, 0.3, 0.4, 0.5,$ $0.6, 0.7, 0.8, 0.9\}$	
	$\delta_a, \delta_e, \delta_r$	$\{(0, 0, 0), (\pm 10, 0, 0),$ $(0, \pm 10, 0), (0, 0, \pm 10)\}$	deg
3	α	$\pm\{0, 2, 4, 6, 8, 10, 15,$ $20, 25, 30, 35, 40\}$	deg
	β	$\pm\{0, 5\}$	deg
	$Mach$	$\{0.1, 0.2, 0.3, 0.4, 0.5,$ $0.6, 0.7, 0.8, 0.9\}$	
	$\delta_a, \delta_e, \delta_r$	$\{(0, 0, 0), (\pm 10, 0, 0),$ $(0, \pm 10, 0), (0, 0, \pm 10)\}$	deg

Table 4.3: The flight conditions at which the force and moment coefficients are calculated

CHAPTER 5

MINIMUM-ENERGY GUIDANCE AND CONTROL DESIGN FOR LAUNCH AND BOOST PHASES

5.1 Introduction

According to the mission profile described in this study; having launched the missile from a submarine, launch phase and boost phase should successfully be completed to proceed with the cruise phase. The success of the launch phase and boost phase can be defined as follows: for a given initial launch condition, achieving desired water-exit condition at the end of the launch phase, then, with the obtained water-exit condition, achieving desired flight condition at the end of boost phase. In order to achieve the desired range or increase the range of launch and boost phases, it is crucial to use available energy for thrust generation efficiently. The total energy need of launch and boost phases can change according to the initial and final flight conditions of these phases and also with the total planned completion time. So, a control and guidance scheme to be applied should take into account these factors to increase missile range for the phases before the cruise. In practice, desired flight conditions at the end of the boost phase can be determined with mission objectives or system constraints. For instance, to be able to start the cruise engine, it may be necessary that the missile should be in a predefined region of speed-altitude envelope. Moreover, the initial success of cruise autopilots may depend on the flight conditions at the beginning of the cruise phase. Therefore, effective usage of available energy to increase missile range gives also the flexibility to the system designer to accomplish some other goals.

In this study, the energy optimizing guidance and control problem of launch and boost phases are approached as a minimum-effort optimal control problem. In this approach, firstly, simplified equations of motion are obtained for both launch and boost phases. Then, the minimum-effort optimal control problem is formulated mathematically. In that formulation, energy associative cost function to be minimized is determined as the integral of the square of the applied thrust. To numerically solve the formulated infinite dimensional optimal control problems, they are treated as finite dimensional parameter optimization problems. Optimal control solutions for different water-exit pitch angle scenarios are obtained. After that, the effect of other initial and final conditions on cost and flight results are investigated and optimal conditions that result with minimum energy scenarios are found. Finally, the cost analysis for overall design is stated, and the mission profiles for horizontal and vertical launch cases which need minimum energy are described.

5.2 Simplified Equations of Motion

Simplification of the nonlinear equations of motion for launch and boost phases is aimed for several reasons. Firstly, for both of the phases, no control is desired in the lateral plane. Assuming that there is not any lateral motion or a disturbance which may induce it, longitudinal dynamics can be decoupled from lateral dynamics. Then, it will be sufficient only to consider the control effort of longitudinal dynamics. Secondly, since the optimal control solutions will be found using optimization, the performance of the optimization algorithm decreases as the model complexity increases. So, to decrease the computation time of optimization algorithms, it is advantageous to have simpler models. In addition to the decoupling of longitudinal and lateral dynamics, further simplifications are done by using fitting methods to calculate the hydrodynamic and aerodynamic coefficients, instead of using multidimensional interpolation methods on the aerodynamic/hydrodynamic database, which need the longer computation time than that of fitting methods.

In this section, nonlinear equations of motion for the launch and boost phases are simplified. Then, the simplified model accuracy is tested with respect to the results of the nonlinear model.

5.2.1 Simplified Equations of Motion for Launch Phase

In this phase, control action only consists of changing booster thrust magnitude. As it is previously explained in Chapter 2, due to the relationship between the center of buoyancy and the center of gravity, when the missile is at rest in underwater, a positive pitching moment occurs. Then, if an appropriate thrust profile is applied, while the missile is being carried up to the sea surface, attitude and water-exit velocity can also be controlled. In this phase, no control is desired in the lateral plane. By assuming any disturbance for lateral motion, longitudinal motion can be decoupled from lateral motion. In conclusion, the following assumptions can be made to simplify the dynamics of the launch phase:

- Thrust deflection angles θ_T and ψ_T are zero.
- Roll rate, p, yaw rate, r, and sideslip angle, β, are zero.
- Side body velocity, v, is zero.
- Among body velocities, forward velocity is the dominant component, i.e., $u >> v$ and $u >> w$.

Hence, using Equation (3.90), equations of motion related to longitudinal dynamics become:

$$\begin{aligned} X &= m\dot{u} - X_{\dot{u}}\dot{u} + mwq - Z_{\dot{w}}qw - Z_{\dot{q}}q^2 \\ Z &= m\dot{w} - Z_{\dot{w}}\dot{w} - Z_{\dot{q}}\dot{q} - mqu + X_{\dot{u}}uq \\ M &= I_y\dot{q} - M_{\dot{w}}\dot{w} - M_{\dot{q}}\dot{q} + Z_{\dot{w}}wu + Z_{\dot{q}}qu - X_{\dot{u}}uw \end{aligned} \tag{5.1}$$

Moreover, with the assumptions above force and moment terms are simplified as:

$$\begin{aligned} X &= QA(C_{x0} + C_{xq}\frac{d}{2u}q) + T - (W - B)\sin(\theta) \\ Z &= QA(C_{z0} + C_{zq}\frac{d}{2u}q) + (W - B)\cos(\theta) \\ M &= QAd(C_{m0} + C_{mq}\frac{d}{2u}q) + x_b B\cos(\theta) \end{aligned} \tag{5.2}$$

Substituting Equation (5.2) into Equation (5.1) gives:

$$
\begin{aligned}
\dot{u} &= \frac{QAC_{x0} + QAC_{xq}\frac{d}{2u}q + T - (W-B)\sin(\theta) - mwq + Z_{\dot{w}}wq + Z_{\dot{q}}q^2}{m - X_{\dot{u}}} \\
\dot{w} &= \frac{QAC_{z0} + QAC_{zq}\frac{d}{2u}q + (W-B)\cos(\theta) + mqu + Z_{\dot{q}}\dot{q} - X_{\dot{u}}qu}{m - Z_{\dot{w}}} \\
\dot{q} &= \frac{QAdC_{m0} + QAC_{mq}\frac{d^2}{2u}q + x_b B\cos(\theta) + M_{\dot{w}}\dot{w} - Z_{\dot{w}}wu - Z_{\dot{q}}qu + X_{\dot{u}}uw}{I_y - M_{\dot{q}}}
\end{aligned}
\tag{5.3}
$$

The states related to height, z, and pitch angle, θ, can be defined as:

$$
\begin{aligned}
\dot{\theta} &= q \\
\dot{z} &= -\sin(\theta)u + \cos(\theta)w
\end{aligned}
\tag{5.4}
$$

In conclusion, longitudinal dynamics of the missile in launch phase can be defined as,

$$\dot{\boldsymbol{x}} = \boldsymbol{h}(\boldsymbol{x}, \boldsymbol{u}) \tag{5.5}$$

where the state vector $\boldsymbol{x}$ and control vector $\boldsymbol{u}$ are,

$$
\begin{aligned}
\boldsymbol{x} &= [u(t), w(t), q(t), \theta(t), z(t)]^T \\
\boldsymbol{u} &= [T(t)]
\end{aligned}
\tag{5.6}
$$

and $\boldsymbol{h}(\boldsymbol{x}, \boldsymbol{u})$ is the vector of expressions given in right-hand side of Equation (5.3) and Equation (5.4).

5.2.1.1 Comparison Between the Simplified Model and the Nonlinear Model

To verify the assumptions made and see how the simplified system which is given in Equation (5.5) approximates to the reference 6 DOF nonlinear dynamics, some scenarios with different control inputs and initial conditions are simulated, and results are compared. These scenarios are explained and the obtained comparison results are given below.

- Scenario 1: Application of maximum thrust

In this scenario, the initial forward velocity is 10 m/s. Initial pitch angle, pitch rate, and down velocity values are chosen to be zero. The motion starts from a depth of 100 meters. A constant thrust of 30 kN is applied from the beginning until the missile reaches to the sea surface. So, the initial state vector and applied control input in this scenario are:

$$\begin{aligned} \boldsymbol{x_0} &= [10, 0, 0, 0, 100]^T \\ \boldsymbol{u} &= [30000] \end{aligned} \tag{5.7}$$

Comparison of the results for the simplified and the 6 DOF nonlinear dynamics for Scenario 1 is given in Figure 5.1

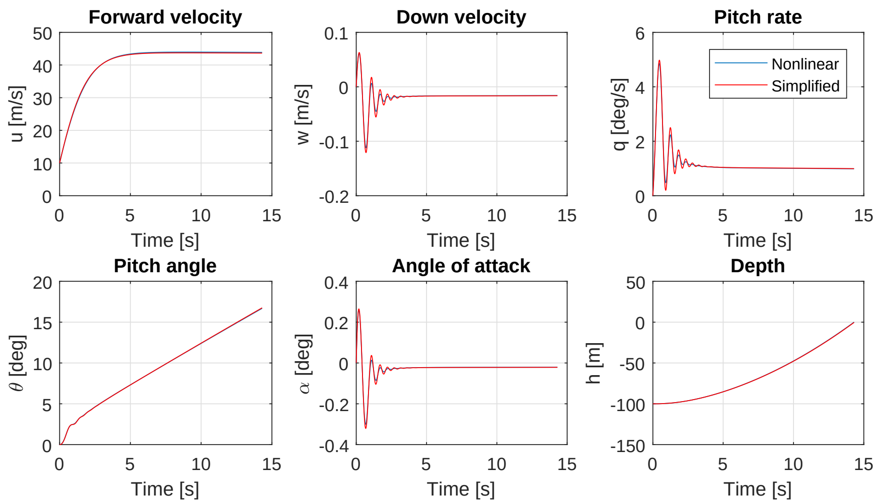

Figure 5.1: Launch phase nonlinear and simplified model comparison for Scenario 1

- Scenario 2: Application of low thrust

This scenario is the same with the first scenario except that a constant thrust of 4 kN is applied from the beginning until the missile reaches to the sea surface. So, the initial state vector and applied control input in this scenario are:

$$\begin{aligned} \boldsymbol{x_0} &= [10, 0, 0, 0, 100]^T \\ \boldsymbol{u} &= [4000] \end{aligned} \tag{5.8}$$

Comparison of the results for Scenario 2 is given in Figure 5.2

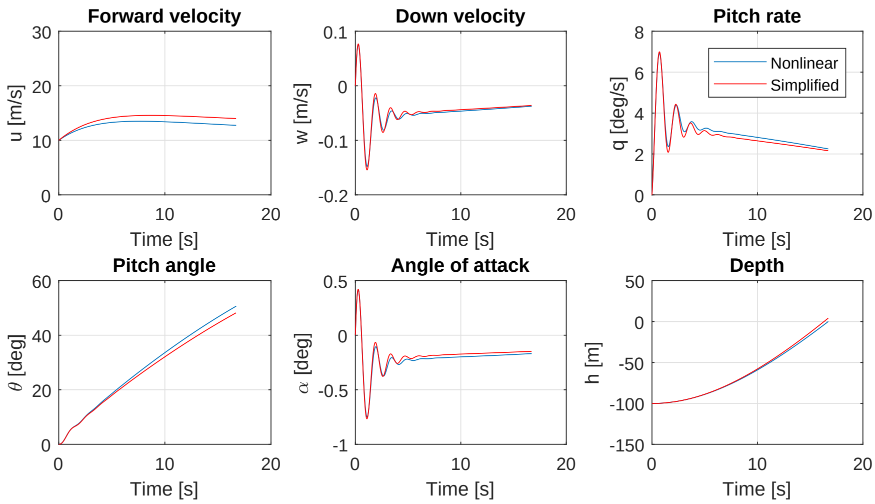

Figure 5.2: Launch phase nonlinear and simplified model comparison for Scenario 2

- Scenario 3: Application of low thrust with non-zero initial attitude

This scenario is the same with the second scenario except that the initial pitch angle is changed to 45 degrees from 0 degrees. So, the initial state vector and applied control input in this scenario are:

$$\begin{aligned} \boldsymbol{x_0} &= [10, 0, 0, 45, 100]^T \\ \boldsymbol{u} &= [4000] \end{aligned} \tag{5.9}$$

Comparison of the results for Scenario 3 is given in Figure 5.3

- Scenario 4: Application of increasing thrust with non-zero initial attitude

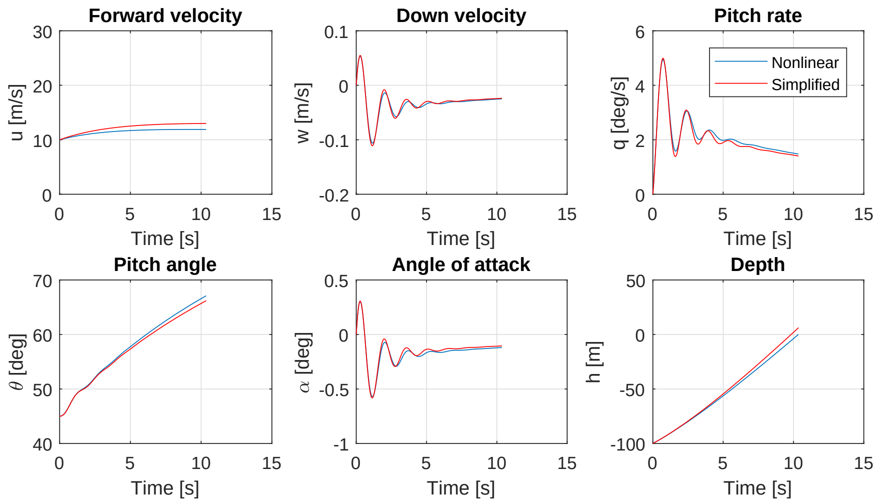

Figure 5.3: Launch phase nonlinear and simplified model comparison for Scenario 3

This scenario is the same with the third scenario except that the initial depth is 200 meters, and the applied thrust linearly increases from 1 kN to 30 kN in 15 seconds. So, the initial state vector and applied control input in this scenario are:

$$\begin{aligned} \boldsymbol{x_0} &= [10, 0, 0, 45, 200]^T \\ \boldsymbol{u} &= [\frac{29000}{15}t + 1000] \end{aligned} \tag{5.10}$$

Comparison of the results for Scenario 4 is given in Figure 5.4

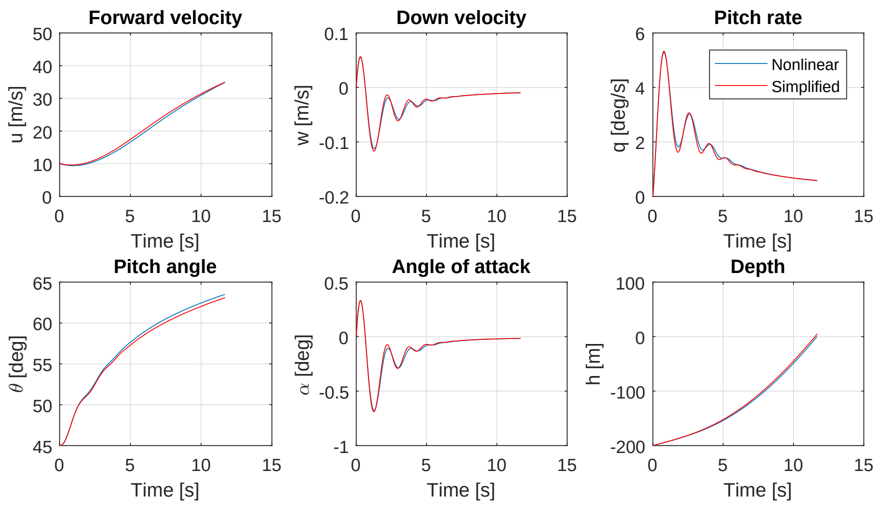

Figure 5.4: Launch phase nonlinear and simplified model comparison for Scenario 4

The comparison figures show that down velocity, pitch rate, and depth values are nearly the same for nonlinear and simplified dynamics. In low thrust scenarios, some small deviations are observed in the forward velocity. Also, for all cases, some deviation for pitch angle exists, and it may increase as simulation time increases since the integral error of pitch rate accumulates. However, the differences are in acceptable levels, and it can be concluded that the simplified model for launch phase is accurate enough relative to the derived nonlinear model and it can be used in optimal control design.

5.2.2 Simplified Equations of Motion for Boost Phase

In this phase, control action consists of changing both booster thrust magnitude and thrust deflection. Attitude control of this phase will be achieved using thrust vector control. As in the case of the launch phase, no control is desired in the lateral plane for boost phase. By assuming any disturbance for lateral motion, longitudinal motion can be decoupled from lateral motion. In conclusion, the following assumptions can be made to simplify the dynamics of the launch phase:

- Roll rate, p, yaw rate, r, and sideslip angle, β, are zero.
- Side body velocity, v, is zero.
- Among body velocities, forward velocity is the dominant component, i.e., $u >> v$ and $u >> w$.

Then, using Equation (3.90), equations of motion related to longitudinal dynamics for boost phase become:

$$\begin{aligned} X &= m\dot{u} + mwq \\ Z &= m\dot{w} - mqu \\ M &= I_y\dot{q} \end{aligned} \tag{5.11}$$

Force and moment terms are simplified as:

$$
\begin{aligned}
X &= QA(C_{x0} + C_{xq}\frac{d}{2u}q) + T - W\sin(\theta) \\
Z &= QA(C_{z0} + C_{zq}\frac{d}{2u}q) - T\theta_T + W\cos(\theta) \\
M &= QAd(C_{m0} + C_{mq}\frac{d}{2u}q) + Tl_x\theta_T
\end{aligned}
\tag{5.12}
$$

Substituting Equation (5.12) into Equation (5.11) gives:

$$
\begin{aligned}
\dot{u} &= \frac{QAC_{x0} + QAC_{xq}\frac{d}{2u}q + T - W\sin(\theta) - mwq}{m} \\
\dot{w} &= \frac{QAC_{z0} + QAC_{zq}\frac{d}{2u}q - T\theta_T + W\cos(\theta) + mqu}{m} \\
\dot{q} &= \frac{QAdC_{m0} + QAC_{mq}\frac{d^2}{2u}q + Tl_x\theta_T}{I_y}
\end{aligned}
\tag{5.13}
$$

The states for height and pitch angle can be defined as in Equation (5.4). Then, the longitudinal dynamics of the missile in boost phase can be defined as,

$$
\dot{\boldsymbol{x}} = \boldsymbol{h}(\boldsymbol{x}, \boldsymbol{u}) \tag{5.14}
$$

where the state vector $\boldsymbol{x}$ and control vector $\boldsymbol{u}$ are,

$$
\begin{aligned}
\boldsymbol{x} &= [u(t), w(t), q(t), \theta(t), z(t)]^T \\
\boldsymbol{u} &= [T(t), \theta_T(t)]^T
\end{aligned}
\tag{5.15}
$$

and $\boldsymbol{h}(\boldsymbol{x}, \boldsymbol{u})$ is the vector of expressions given in right hand side of Equation (5.13) and Equation (5.4).

5.2.2.1 Comparison Between the Simplified Model and the Nonlinear Model

Similar to the case of the launch phase, to check how the system which is given in Equation (5.14) approximates to the reference 6 DOF nonlinear dynamics under the assumptions made, some scenarios with different control inputs are simulated and results are compared. For each scenario, the appropriate command of thrust deflection in the vertical plane, $\theta_T(t)$, is calculated with the pitch angle autopilot, whose details will be given in Chapter 6. These scenarios are explained and the obtained results are given below.

- Scenario 1: From vertical to horizontal pitch attitude with constant thrust

In this scenario, the initial forward velocity is 35 m/s. The initial pitch angle is 90 degrees, pitch rate, and down velocity values are chosen to be zero. The motion starts from 0 meters altitude. A constant thrust of 30kN is applied for 15 seconds. So, the initial state vector and applied control input in this scenario are:

$$\begin{aligned} \boldsymbol{x_0} &= [35, 0, 0, 90, 0]^T \\ \boldsymbol{u} &= [30000, \theta_T(t)]^T \end{aligned} \tag{5.16}$$

Figure 5.5 shows comparison of the results for Scenario 1.

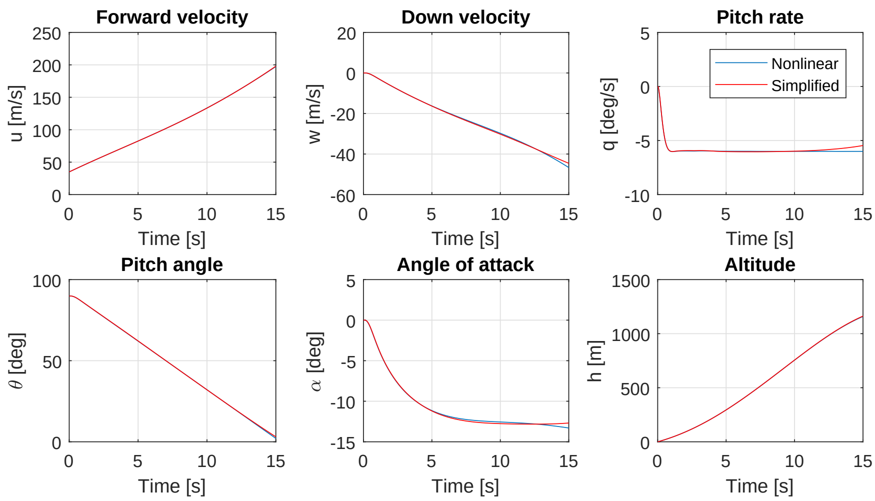

Figure 5.5: Boost phase nonlinear and simplified model comparison for Scenario 1

- Scenario 2: From vertical to horizontal pitch attitude with decreasing thrust

As different from Scenario 1, the applied thrust is not constant but linearly decreasing from 30 kN to 15 kN in 15 seconds. The initial state vector and applied control input in this scenario are:

$$\begin{aligned} \boldsymbol{x_0} &= [35, 0, 0, 90, 0]^T \\ \boldsymbol{u} &= [-1000t + 30000, \theta_T(t)]^T \end{aligned} \tag{5.17}$$

Comparison of the results for Scenario 2 is given in Figure 5.6.

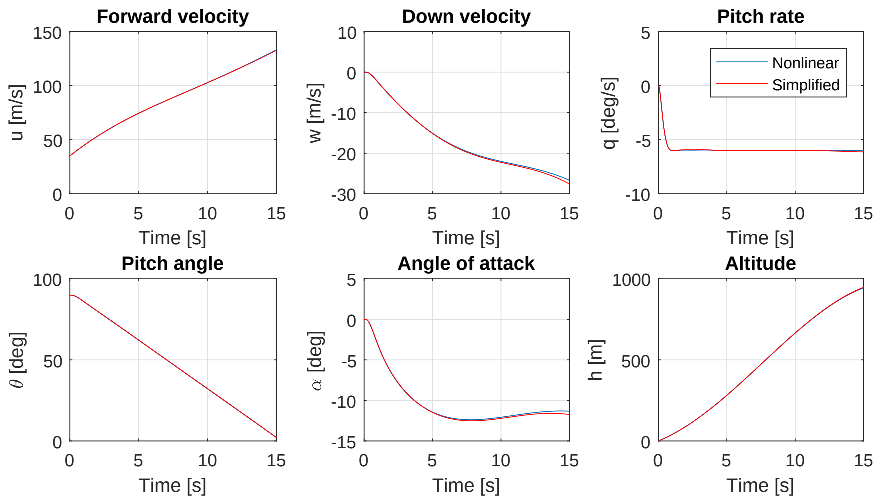

Figure 5.6: Boost phase nonlinear and simplified model comparison for Scenario 2

- Scenario 3: From 45 to 0 degrees pitch attitude with constant thrust

The difference in this scenario from the first scenario is that the initial pitch angle in this scenario is 45 degrees. The initial state vector and applied control input in this scenario are:

$$\begin{aligned} \boldsymbol{x_0} &= [35, 0, 0, 45, 0]^T \\ \boldsymbol{u} &= [30000, \theta_T(t)]^T \end{aligned} \tag{5.18}$$

Comparison of the results for Scenario 3 is given in Figure 5.7.

- Scenario 4: From 45 to 0 degrees pitch attitude with decreasing thrust

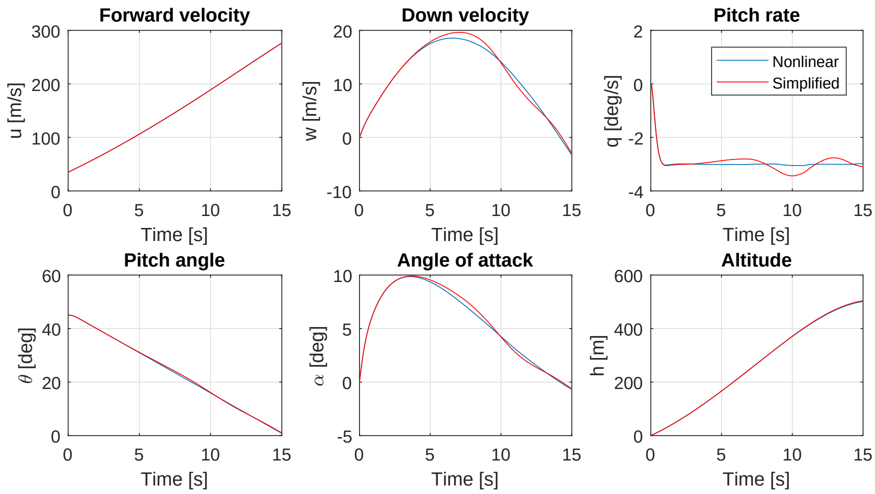

Figure 5.7: Boost phase nonlinear and simplified model comparison for Scenario 3

The only difference from Scenario 2 is that the initial pitch angle in this scenario is 45 degrees. The initial state vector and applied control input in this scenario are:

$$\begin{aligned} \boldsymbol{x_0} &= [35, 0, 0, 45, 0]^T \\ \boldsymbol{u} &= [-1000t + 30000, \theta_T(t)]^T \end{aligned} \tag{5.19}$$

Comparison of the results for Scenario 4 is given in Figure 5.8.

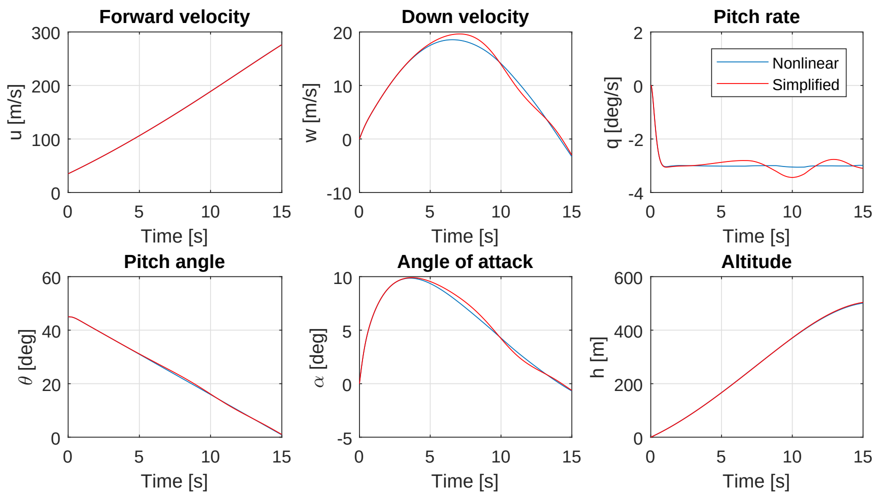

Figure 5.8: Boost phase nonlinear and simplified model comparison for Scenario 4

By examining the comparison figures, it is seen that forward velocity, pitch angle, and altitude results are close to each other for simplified and nonlinear dynamics. For down velocity, pitch rate, and angle of attack results, there are some small deviations for 45 degrees initial pitch angle scenarios. However, since the differences are in acceptable levels, it can be said that the simplified model for boost phase is accurate enough relative to the derived nonlinear model and can be used in optimal control design.

5.3 Minimum-Effort Optimal Control Problem Formulation

This class of optimal control problems can be described as finding an optimal control $\boldsymbol{u}(t)$ satisfying constraints of the form

$$M_{i-} \leq u_i(t) \leq M_{i+}, \quad i = 1, 2, ..., m \tag{5.20}$$

where $u_i(t)$ is the i^{th} control variable, m is the number of control variables M_{i-} and M_{i+} are allowed minimum and maximum values of each control variable, and which transfers a system described by

$$\dot{\boldsymbol{x}}(t) = \boldsymbol{h}(\boldsymbol{x}(t), \boldsymbol{u}(t), t) \tag{5.21}$$

from an initial state $\boldsymbol{x}(t_0)$ to a specified final state $\boldsymbol{x}(t_f)$ with a minimum expenditure of control effort [36]. Control effort to be minimized can be defined with the following performance index:

$$J(\boldsymbol{u}) = \int_{t_0}^{t_f} \left[\sum_{i=1}^{m} r_i {u_i}^2(t) \right] dt \tag{5.22}$$

where $r_i, i = 1, 2, ..., m$ are nonnegative weighting factors for control variables. For the problem considered in the thesis, performance index to be minimized is defined as

$$J(\boldsymbol{u}) = \int_{t_0}^{t_f} T^2(t) dt \tag{5.23}$$

such that the aim is to minimize the square of applied thrust through a time interval, which represent the total energy need. To solve the formulated infinite dimensional optimal control problem by numerical methods, it can be transformed into a finite dimensional optimization problem by discretization [37]. In order to apply discretization, firstly assuming $t_0 = 0$, $[t_0, t_f] = [0, t_f]$ range can be divided into N equal parts with a proper choice of time step, Δt, as:

$$N = \frac{t_f - t_0}{\Delta t} = \frac{t_f}{\Delta t} \tag{5.24}$$

Trapezoidal rule for integration yields that

$$\begin{aligned}\int_0^{t_f} F(s) &\approx \frac{F(s_0) + F(s_1)}{2}\Delta t + \frac{F(s_1) + F(s_2)}{2}\Delta t + ... + \frac{F(s_{N-1}) + F(s_N)}{2}\Delta t \\ &= \frac{\Delta t}{2}(F(s_0) + 2F(s_1) + 2F(s_2) + ... + 2F(s_{N-1}) + F(s_N))\end{aligned} \tag{5.25}$$

where s_k for $k = 0, 1, 2, ..., N$ are discrete samples of a continuous function $s(t)$ which is sampled at time instants of $t = k\Delta t$ for $k = 0, 1, 2, ..., N$. Using this approximate integral formula, performance index in Equation (5.23) can be rewritten as:

$$J(\boldsymbol{u}) = \frac{\Delta t}{2}(T_0^2 + 2(T_1^2 + ... + T_{N-1}^2) + T_N^2) \tag{5.26}$$

where T_k, $k = 0, 1, 2, ..., N$ are discrete samples of the applied thrust. Now, the problem is turned into a finite dimensional constrained optimization problem where the aim is to find the $m \times (N + 1)$ dimensional control solution,

$$\boldsymbol{u} = [\boldsymbol{u_0 u_1 ... u_{N-1} u_N}] \tag{5.27}$$

which minimizes

$$J(\boldsymbol{u}) = \frac{\Delta t}{2}(T_0^2 + 2(T_1^2 + ... + T_{N-1}^2) + T_N^2) \tag{5.28}$$

and subject to

$$\begin{aligned} &\boldsymbol{x}(t=0)=\boldsymbol{x_0}, \qquad \boldsymbol{x}(t=N\Delta t)=\boldsymbol{x_f} \\ &\boldsymbol{M_-}\leq \boldsymbol{u}\leq \boldsymbol{M_+} \end{aligned} \tag{5.29}$$

where $\boldsymbol{M_-}\in\mathbb{R}^{m\times(N+1)}$ and $\boldsymbol{M_+}\in\mathbb{R}^{m\times(N+1)}$ are the matrices that define lower and upper limits of the allowed discrete control series.

The derived constrained optimization problem formulation is specialized for launch and boost phases in the following sections.

5.3.1 Problem Formulation for Launch Phase

Since the control variable for the launch phase is the applied thrust, $T(t)$, the constrained optimization problem for this phase can be described as finding

$$u=[T_0T_1...T_{N-1}T_N] \tag{5.30}$$

which minimizes

$$J(u)=\frac{\Delta t}{2}(T_0^2+2(T_1^2+...+T_{N-1}^2)+T_N^2) \tag{5.31}$$

subject to

$$\begin{aligned} \boldsymbol{x}(t=0)&=[u(0),w(0),q(0),\theta(0),z(0)]^T \\ \boldsymbol{x}(t=t_f)&=[u(t_f),w(t_f),q(t_f),\theta(t_f),z(t_f)]^T \\ 0\leq T_k&\leq 30000 \quad for \quad k=0,1,2,...,N \end{aligned} \tag{5.32}$$

5.3.2 Problem Formulation for Boost Phase

Since the control variables for the boost phase are the applied thrust, $T(t)$, and the thrust deflection in vertical plane, $\theta_T(t)$, the constrained optimization problem for this phase can be described as of finding

$$\boldsymbol{u} = \begin{bmatrix} T_0 T_1 ... T_{N-1} T_N \\ \theta_{T0}\theta_{T1}...\theta_{TN-1}\theta_{TN} \end{bmatrix} \tag{5.33}$$

which minimizes

$$J(u) = \frac{\Delta t}{2}(T_0^2 + 2(T_1^2 + ... + T_{N-1}^2) + T_N^2) \tag{5.34}$$

subject to

$$\begin{aligned} \boldsymbol{x}(t=0) &= [u(0), w(0), q(0), \theta(0), z(0)]^T \\ \boldsymbol{x}(t=t_f) &= [u(t_f), w(t_f), q(t_f), \theta(t_f), z(t_f)]^T \\ 0 \leq & T_k \leq 30000 \quad for \quad k = 0, 1, 2, ..., N \\ -12^\circ \leq & \theta_{Tk} \leq 12^\circ \qquad for \quad k = 0, 1, 2, ..., N \end{aligned} \tag{5.35}$$

Discretization time step, Δt, is chosen as 0.2 seconds. This means that for example, in the launch phase, optimal thrust solution to be found for 15 seconds motion, is a vector with 76 elements. These elements can be regarded as parameters to be found by constrained optimization problem solvers. To solve the described constrained optimization problem for launch and boost phases, an algorithm which is based on interior-point methods is used.

5.4 Optimal Control Solutions for Launch and Boost Phases

5.4.1 Different Water-Exit Pitch Angle Scenarios

Firstly, different water-exit pitch angle scenarios are investigated. The set of possible water-exit pitch angles are chosen as $\theta = \{20, 35, 45, 55, 65, 75, 90\}$ degrees.

5.4.1.1 Launch Phase Solutions for Horizontal Launch Case

The conditions just after the launch from the submarine are assigned as the initial conditions of the system at the beginning of this phase. These conditions are described as; 10 m/s forward velocity, 100 m water depth and zero down velocity, pitch rate, and pitch angle. Desired final conditions, which are the water-exit conditions, are assumed as; 35 m/s forward velocity, 0 m water depth and one of the pitch angles from the set of $\theta = \{20, 35, 45, 55, 65, 75, 90\}$ degrees. Final pitch rate and down velocity are left as free parameters. Duration of the motion is determined as 15 seconds. Thus, seven different scenarios are investigated in this section. Initial and final conditions can be shown as

$$\begin{aligned} \boldsymbol{x_0} &= [10, 0, 0, 0, 100]^T \\ \boldsymbol{x_f} &= [35, free, free, \theta_f, 0]^T \end{aligned} \tag{5.36}$$

where θ_f is assigned to n^{th} element of the set $\{20, 35, 45, 55, 65, 75, 90\}$, for the n^{th} scenario. Obtained optimal thrust solutions are shown in Figure 5.9

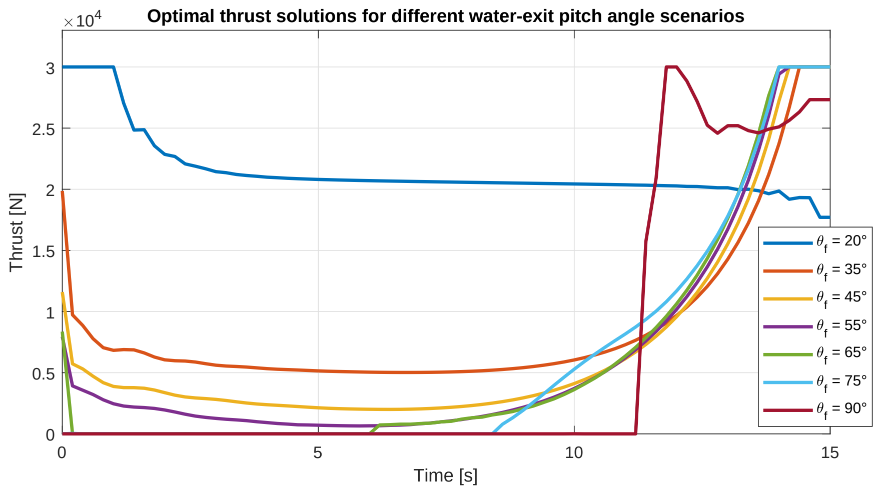

Figure 5.9: Launch phase optimal thrust solutions for different water-exit pitch angle scenarios of horizontal launch

Examining the thrust solutions, it is seen that as desired water-exit angle increases, initial thrust levels decrease. Due to the self positive pitching of the missile after the ejection with given initial conditions, for 75 and 90 degrees solutions, non-zero thrust values are observed around 10 seconds after the ejection. On the other hand, for smaller water-exit angle scenarios, it is needed to apply positive thrust values just after the ejection.

The optimal thrust solutions are applied to the missile in the 6 DOF nonlinear simulation environment. The simulations are stopped when the missile reaches to the sea surface. The forward velocity, pitch angle, angle of attack, and depth results for each scenario are shown in the following figures.

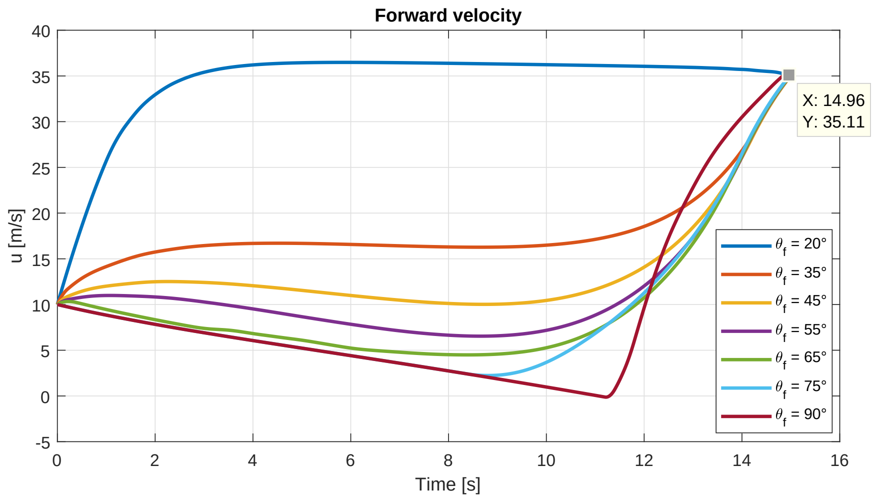

Figure 5.10: Launch phase forward velocity results for different water-exit pitch angle scenarios of horizontal launch

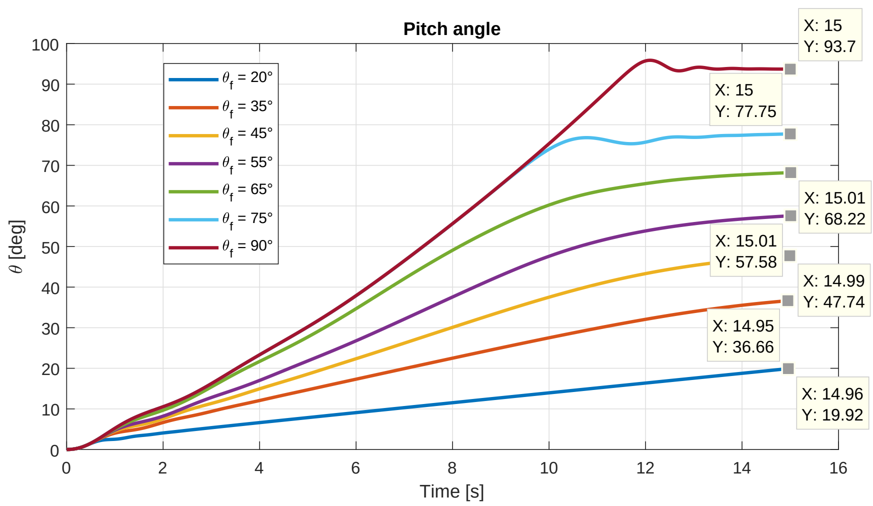

Figure 5.11: Launch phase pitch angle results for different water-exit pitch angle scenarios of horizontal launch

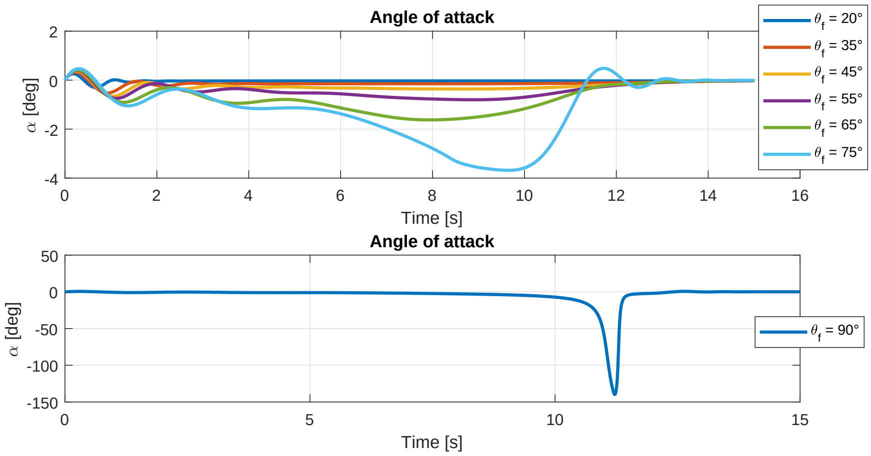

Figure 5.12: Launch phase angle of attack results for different water-exit pitch angle scenarios of horizontal launch

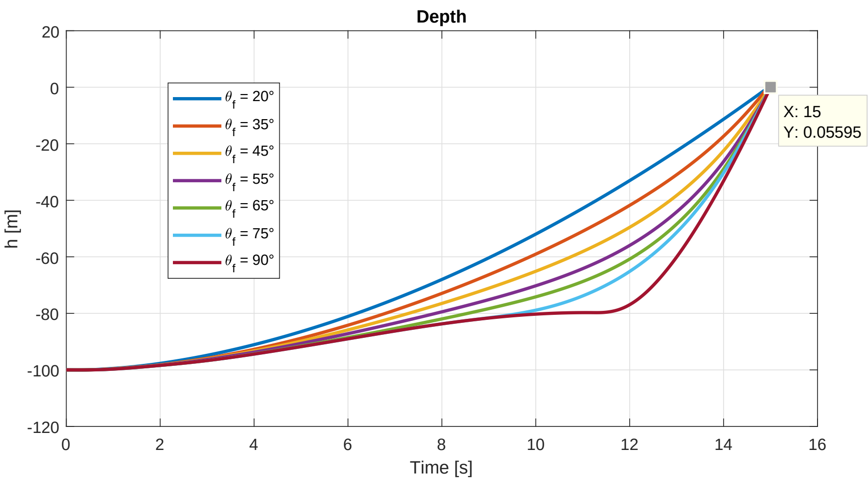

Figure 5.13: Launch phase depth results for different water-exit pitch angle scenarios of horizontal launch

In each scenario, the missile reaches to the sea surface in almost 15 seconds with the forward velocity of 35 m/s, as desired. As the angle of attack values are zero during water-exit, the total velocity of the missile is equal to the achieved forward velocity, and the total velocity vector is aligned with the positive x-axis of the missile body. Water-exit pitch angles are approximately the same as with their desired values. Although there are differences between the obtained and the desired water-exit angles, differences are in acceptable levels. The maximum relative absolute difference is observed in 45 degrees exit scenario. Realized 47.71 degrees water-exit angle corre-

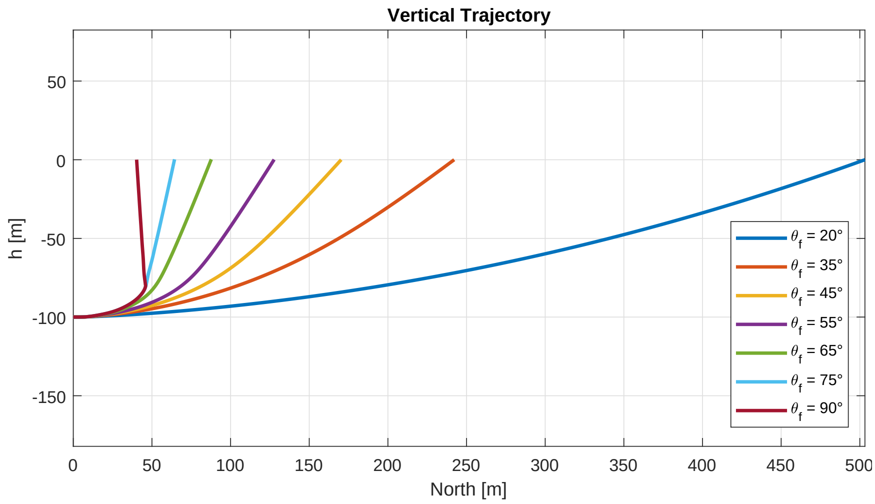

Figure 5.14: Launch phase vertical trajectory results for different water-exit pitch angle scenarios of horizontal launch

sponds to the relative difference percentage of 6.1%. This deviation is expected since the simplified launch phase model pitch angle results differ from the nonlinear launch phase model pitch angle results as it is shown in Section 5.2. Vertical trajectory results show that as the desired water-exit angle decreases, the distance covered by the missile through the north increases. This means that to achieve a smaller water-exit angle, a larger sea area around the ejection point is needed.

The cost for each thrust profile is calculated according to Equation (5.26) and given in Table 5.1. The thrust profile that results with minimum cost is found for 45 degrees water-exit angle case.

$Scenario\ no$	1	2	3	4	5	6	7
$\theta_f\ (deg)$	20	35	45	55	65	75	90
$Cost\ (\times 10^9 N^2 s)$	7.03	1.80	1.67	1.72	1.78	1.82	2.45

Table 5.1: Cost of launch phase optimal thrust solutions for different water-exit pitch angle scenarios of horizontal launch

5.4.1.2 Boost Phase Solutions

The conditions, just after the missile leaves the sea water, are assigned as the initial conditions of the system at the beginning of the boost phase. The final conditions of the launch phase can be considered as the initial conditions of the boost phase. These desired conditions are described as; 35 m/s forward velocity and zero altitude, down velocity and pitch rate. Initial pitch angle set, $\theta = \{20, 35, 45, 55, 65, 75, 90\}$, constitutes the seven different scenarios to be investigated here. Desired final conditions are assumed as; 135 m/s forward velocity, zero pitch angle, and 600 m altitude. Final pitch rate and angle of attack values are left as free parameters. The final time is fixed to 15 seconds. In conclusion, initial and final conditions can be shown as

$$\begin{aligned} \boldsymbol{x_0} &= [35, 0, 0, \theta_0, 0]^T \\ \boldsymbol{x_f} &= [135, free, free, 0, 600]^T \end{aligned} \tag{5.37}$$

where θ_0 is assigned to the n^{th} element of the set $\{20, 35, 45, 55, 65, 75, 90\}$, for the n^{th} scenario. Obtained optimal thrust, $T(t)$, and vertical thrust deflection, $\theta_T(t)$, solutions are shown in Figure 5.15 and Figure 5.16.

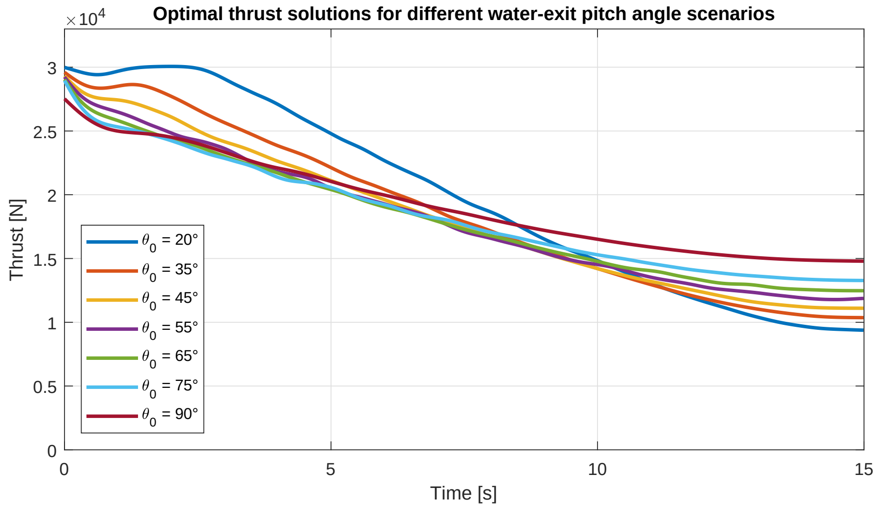

Figure 5.15: Boost phase optimal thrust solutions for different water-exit pitch angle scenarios

Examining the optimal solutions, it is seen that the thrust solutions have similar characteristics except that as the water-exit angle increases, the initial thrust levels de-

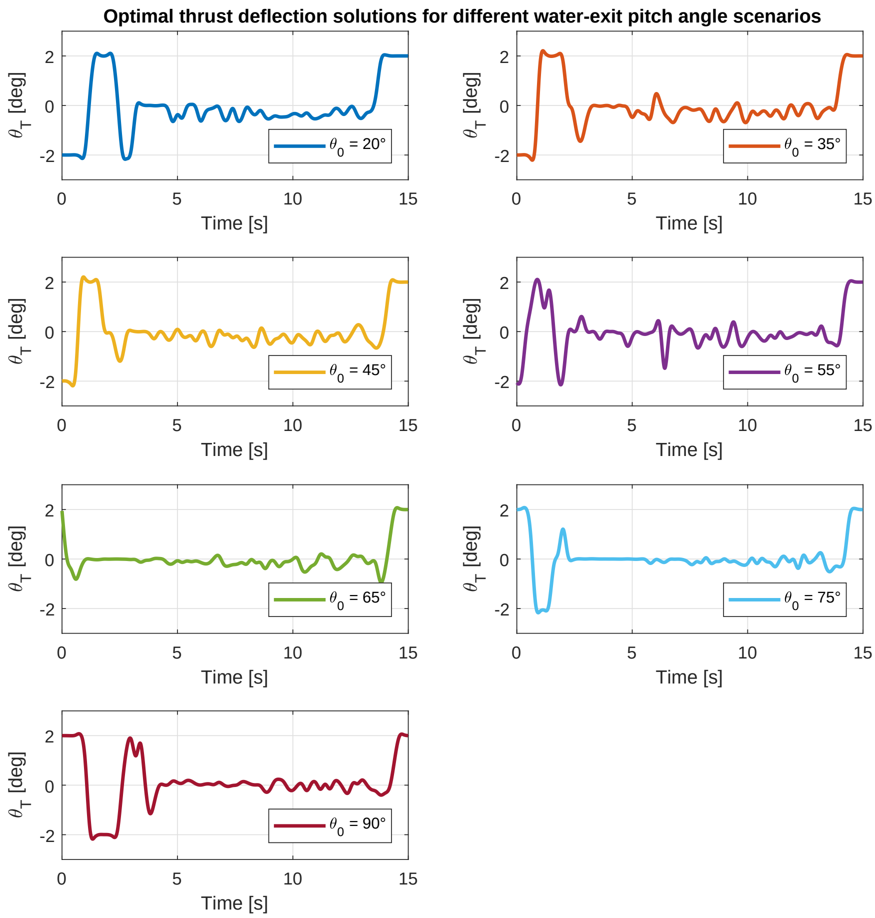

Figure 5.16: Boost phase optimal thrust deflection solutions for different water-exit pitch angle scenarios

crease and the final thrust levels increase. For water-exit angles of 20, 35, 45 and 55 degrees, thrust deflection solutions start with negative values to provide positive pitching moment. On the other hand, for water-exit angles of 65, 75 and 90 degrees, positive starting values of thrust deflection cause negative pitching moment.

Since a pitch angle autopilot, whose details are explained in Chapter 6, is designed for the boost phase, pitch angle profiles that are obtained from the simplified model can be used to guide pitch angle autopilot. Then, instead of using optimal thrust deflection solutions with an open loop control structure, a closed loop control can be achieved by using simplified model's pitch angle output to feed pitch angle autopilot of boost phase. Applying the given optimal thrust and thrust deflection to the simplified model of boost phase, pitch angle characteristic of each scenario are obtained as in Figure 5.17.

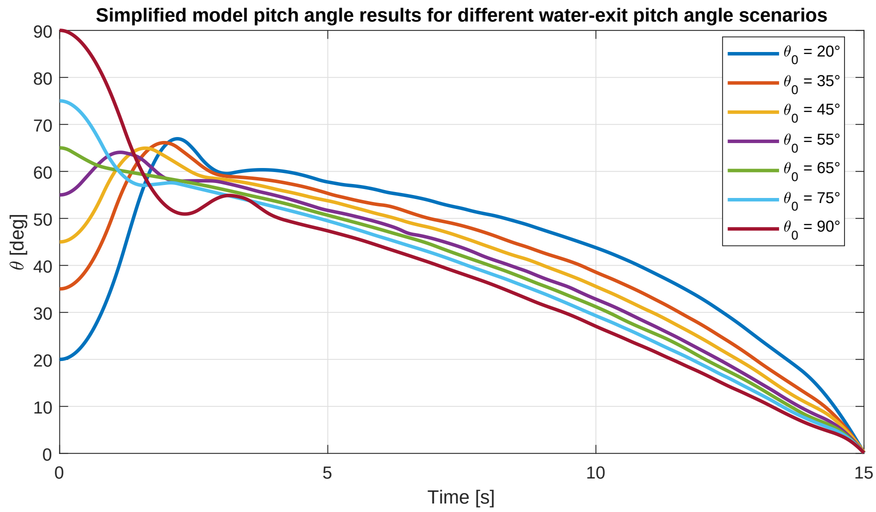

Figure 5.17: Boost phase simplified model pitch angle results for different water-exit pitch angle scenarios

The 6 DOF nonlinear model is simulated with obtained thrust profiles and pitch angle commands for pitch angle autopilot. Simulations are run for 15 seconds. The pitch angle, forward velocity, angle of attack, altitude, and vertical trajectory results for each scenario are shown in the following figures.

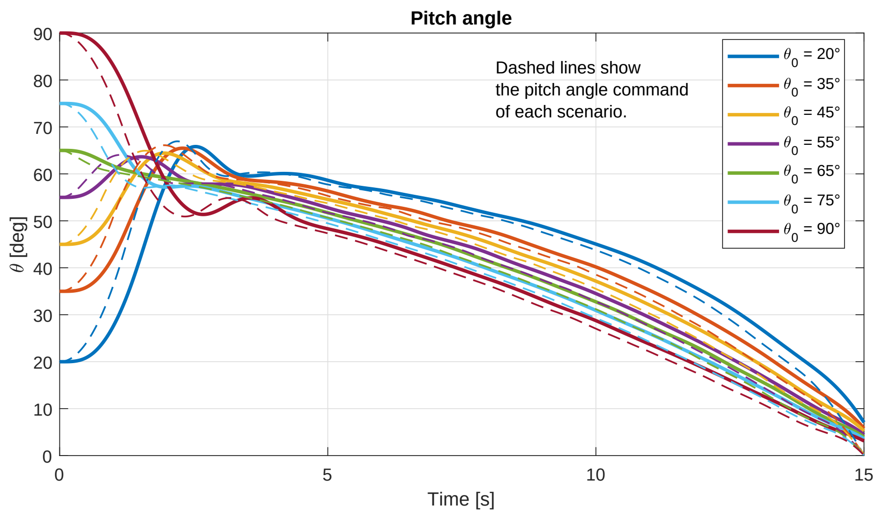

Figure 5.18: Boost phase pitch angle results for different water-exit pitch angle scenarios

Comparing the pitch angle results of the nonlinear model and the simplified model, it is seen that final pitch angle values go nearly to zero, but the exact zero value is

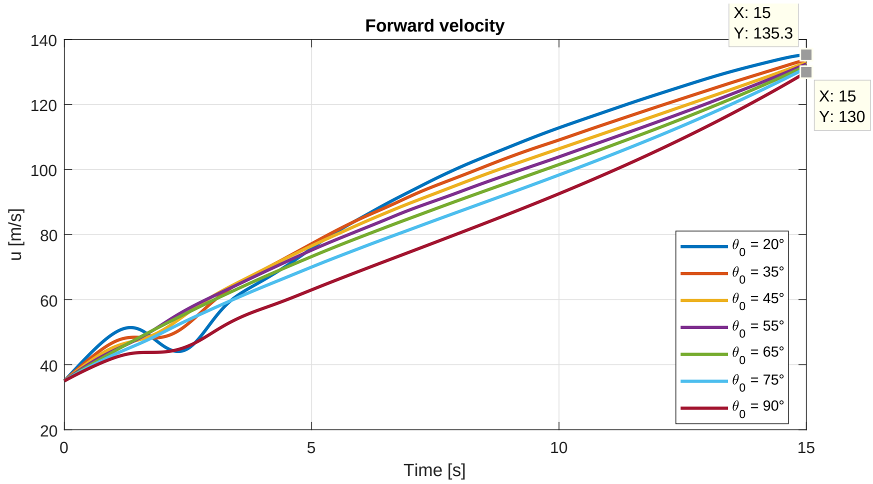

Figure 5.19: Boost phase forward velocity results for different water-exit pitch angle scenarios

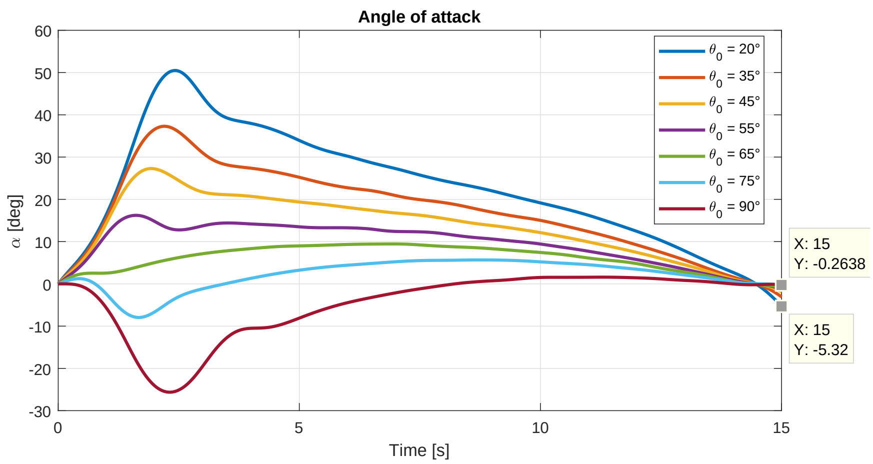

Figure 5.20: Boost phase angle of attack results for different water-exit pitch angle scenarios

not obtained. The reasons for this situation are as follows. First, pitch angle autopilot's command tracking performance is not ideal. Second, the simplified boost phase model pitch angle results differ from the nonlinear boost phase model pitch angle results. However, this deviation can be considered as acceptable by examining how the error in reference pitch angle tracking affects the achievement of other final conditions.

Final forward velocity values for different scenarios are in the range of 130 m/s and 135.3, as pretty much the same as with the desired value of 135 m/s. The maximum

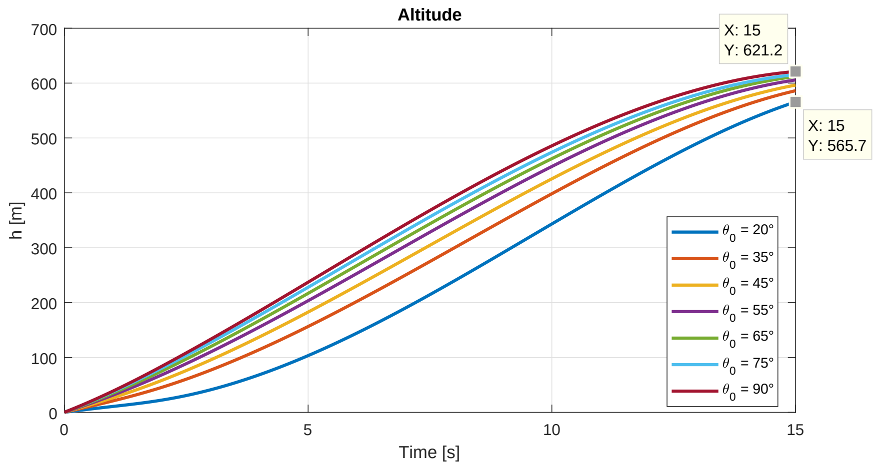

Figure 5.21: Boost phase altitude results for different water-exit pitch angle scenarios

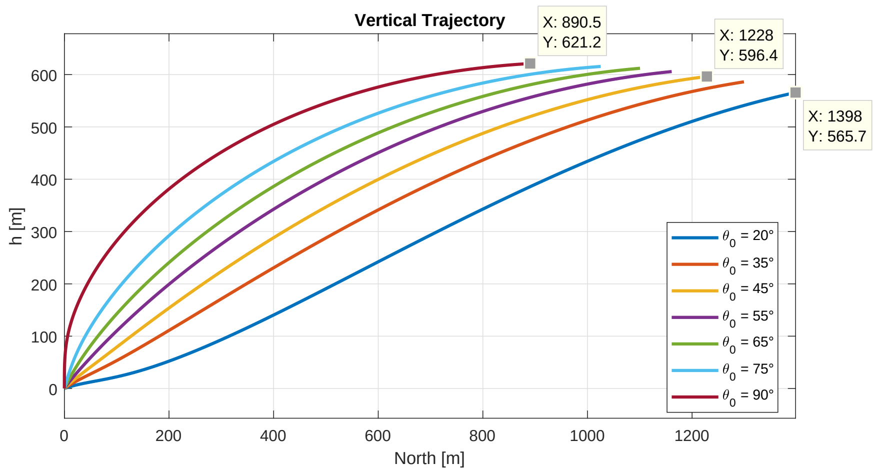

Figure 5.22: Boost phase vertical trajectory results for different water-exit pitch angle scenarios

relative absolute difference, which is seen in 90 degrees water-exit scenario, is 3.7%. Angle of attack values are approximate to zero, meaning that the total velocity vector is almost equal to the forward velocity vector. Final altitude values, where the desired final altitude is 600 meters, are in the range of 565.7-621.2 meters, meaning that relative absolute difference percentage is in the range of 3.53-5.72%, which can be regarded as acceptable. The results of vertical trajectories show that as water-exit angle decreases, the distance covered by the missile through the north increases. This means that after leaving the sea with a smaller water-exit angle, a larger air zone around the water-exit location is needed before the desired final conditions are achieved.

The cost for each scenario is given in Table 5.2. The thrust profile which has the minimum cost occurs in 65 degrees water-exit angle scenario.

$Scenario\ no$	1	2	3	4	5	6	7
$\theta_0\ (deg)$	20	35	45	55	65	75	90
$Cost\ (\times 10^9 N^2 s)$	6.75	5.82	5.46	5.30	5.27	5.35	5.76

Table 5.2: Cost of boost phase optimal thrust solutions for different water-exit pitch angle scenarios

5.4.2 Different Launch Depth Scenarios for Vertical Launch Case

For the case of vertical launching from the submarine, it is assumed that the missile leaves the water vertically with a desired forward velocity. Initial conditions are described as; 10 m/s forward velocity, 90 degrees pitch angle, water depths of $z_0 = \{100, 200, 300, 400, 500\}$ m and zero down velocity, and pitch rate. Desired final conditions are assumed as; 35m/s forward velocity, 90 degrees pitch angle, 0 m water depth. Final pitch rate and down velocity are left as free parameters. Thus, five different scenarios are presented. The final time for each scenario is found with the procedure explained: for each scenario, the magnitude of constant thrust which achieves the desired approximate final conditions is determined. Then, the motion time from launch to water-exit is determined to be used in the described five different optimal control scenarios. These final times for five scenarios are $t_f = \{3.8, 7.0, 10.0, 12.8, 15.8\}$ seconds, respectively. In conclusion, initial and final conditions can be shown as;

$$\begin{aligned} \boldsymbol{x_0} &= [10, 0, 0, 90, z_0]^T \\ \boldsymbol{x_f} &= [35, free, free, 90, 0]^T \end{aligned} \tag{5.38}$$

where z_0 is assigned to n^{th} element of the set $\{100, 200, 300, 400, 500\}$ and t_f is assigned to n^{th} element of the set $\{3.8, 7, 10, 12.8, 15.8\}$ for the n^{th} scenario. Obtained optimal thrust solutions are shown in Figure 5.23

The obtained optimal thrust results are applied in the 6 DOF nonlinear model so that

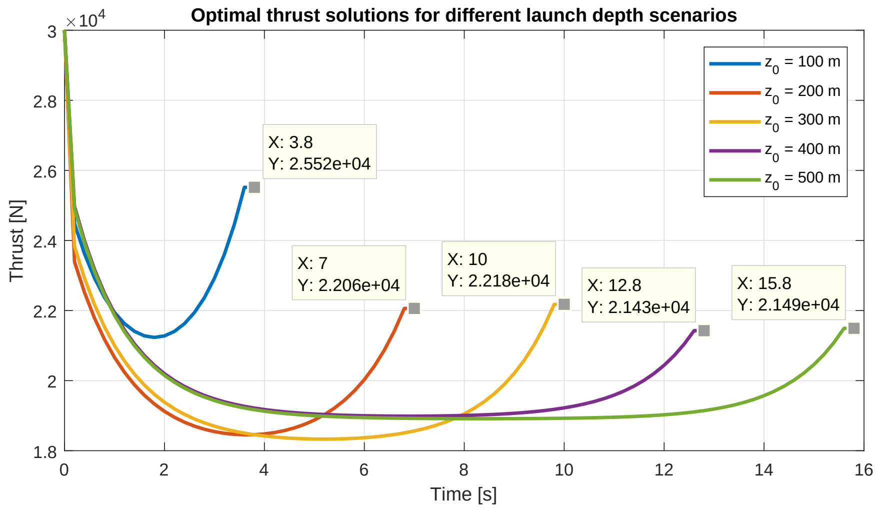

Figure 5.23: Launch phase optimal thrust solutions for different launch depth scenarios of vertical launch

the simulations are stopped when the missile reaches to the sea surface. The forward velocity and depth results for each scenario are shown in the following figures. Since the angle of attack and pitch angle results are constant as 0 and 90 degrees, they are not shown in separate figures here.

The figure of depth change shows that the motion for each scenario is almost completed in their desired final time as the missile reaches to the sea surface. Forward velocity results show that the desired final velocity of 35 m/s is also achieved almost exactly in each scenario.

The cost for each scenario is given in Table 5.3. The data shows that as the launch depth increases, the cost increases. The thrust profile which provides the minimum cost is obtained for the scenario in which the launch depth is 100 m.

$Scenario\ no$	1	2	3	4	5
$z_0\ (m)$	100	200	300	400	500
$Cost\ (\times 10^9 N^2 s)$	1.99	2.78	3.86	5.09	6.15

Table 5.3: Cost of launch phase optimal thrust solutions for different launch depth scenarios of vertical launch

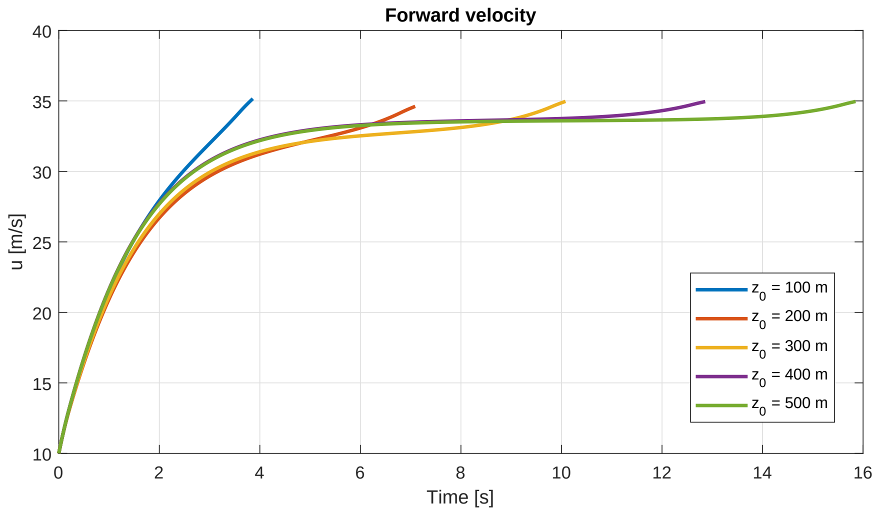

Figure 5.24: Launch phase forward velocity results for different launch depth scenarios of vertical launch

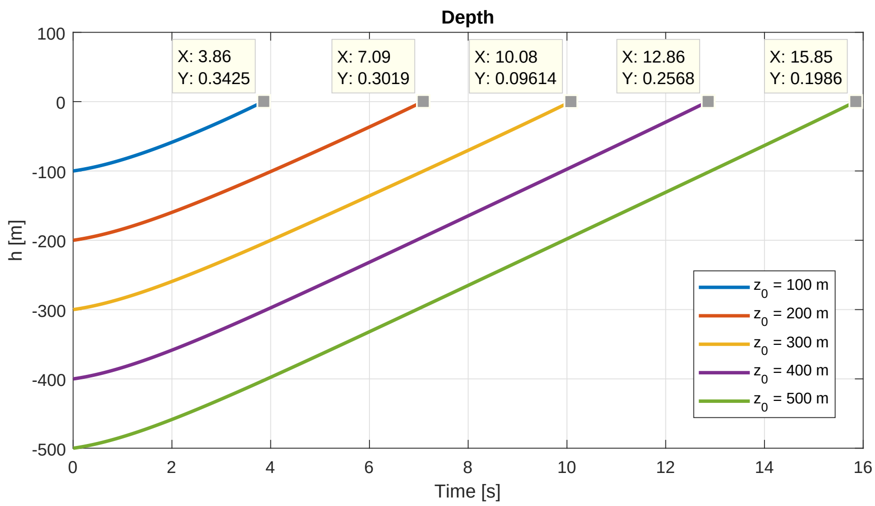

Figure 5.25: Launch phase depth results for different launch depth scenarios of vertical launch

5.4.3 Cost Analysis for Different Water-Exit Pitch Angle Scenarios of Horizontal Launch and Different Launch Depth Scenarios of Vertical Launch

In the previous sections, the cost of different water-exit scenarios for launch and boost phases were given. Minimum cost scenarios among them are 45 degrees water-exit scenario of the launch phase and 65 degrees water-exit scenario of the boost phase. Considering the fact that the boost phase follows the launch phase, optimal thrust solutions for launch and boost phases are combined, and the minimum cost calculation is made by using these combined thrust profiles.

To accomplish a vertical water-exit mission, the missile can be launched horizontally or vertically from the submarine. Since vertical water-exit scenario of horizontal and vertical launch options can provide different costs, their costs can also be compared to find optimal vertical water-exit mission cost for a set of fixed initial and final conditions.

Combined optimal thrust solutions which are found for horizontal launch phase and boost phase for different water-exit pitch angle scenarios are shown in Figure 5.26.

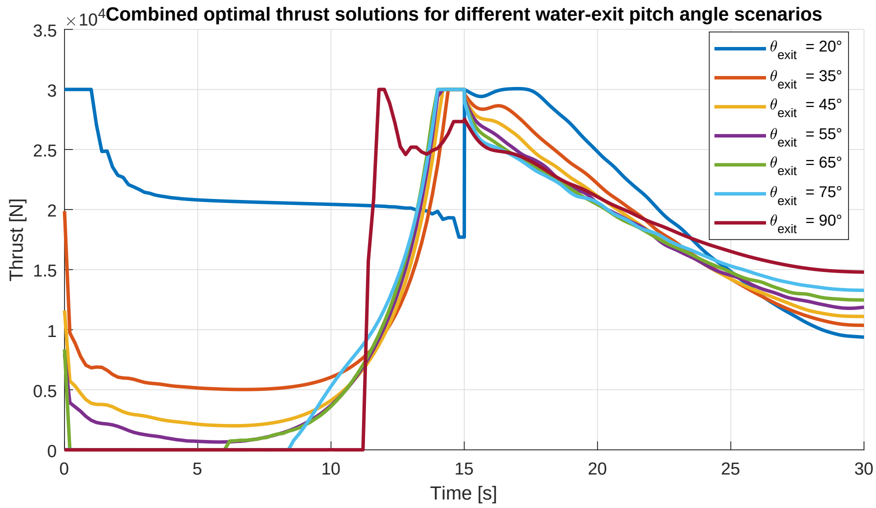

Figure 5.26: Combined launch and boost phase optimal thrust solutions for different water-exit pitch angle scenarios

In Figure 5.27, the costs of the optimal thrust profiles which are given in Figure 5.26, are shown for each different water-exit pitch angle case. In addition to them, the launch phase cost for a vertical launch from 100 m depth, and total energy need as the sum of vertical launch phase and boost phase costs are also shown. The data of total costs is given in Table 5.4.

According to the data of total costs, the following conclusions can be made. For the previously defined initial and final conditions of launch phase and boost phases, 55 degrees water-exit angle scenario needs the minimum total cost, which is $7.01 \times 10^9 N^2 s$. This cost is also less than the total cost of a vertical launch and boost phase,

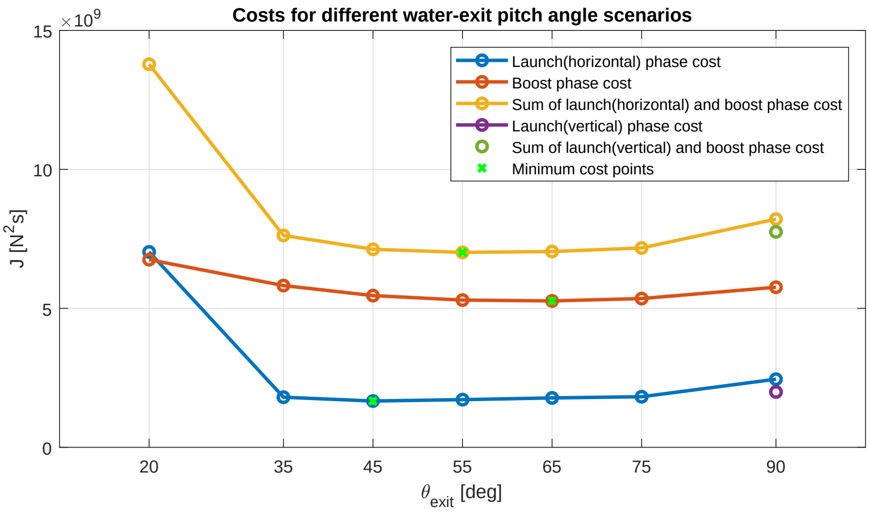

Figure 5.27: Costs of launch and boost phase optimal thrust solutions for different water-exit pitch angle scenarios

$Scenario\ no$	1	2	3	4	5	6	7
$\theta_{exit}\ (deg)$	20	35	45	55	65	75	90
$Total\ launch(horizontal)$ $and\ boost$ $phase\ costs\ (\times 10^9 N^2 s)$	13.78	7.62	7.13	7.01	7.05	7.17	8.21
$Total\ launch(vertical)$ $and\ boost$ $phase\ costs\ (\times 10^9 N^2 s)$	-	-	-	-	-	-	7.75

Table 5.4: Total costs of launch and boost phase optimal thrust solutions for different water-exit pitch angle scenarios

which is $7.75 \times 10^9 N^2 s$. For the vertical water-exit case, total cost of the vertical launch and boost phase, which is $7.75 \times 10^9 N^2 s$, is less than the total cost of the horizontal launch and boost phase, which is $8.21 \times 10^9 N^2 s$. Thus, for the given initial and final conditions of launch and boost phases, the following deductions can be made:

- Among other examined water-exit angles, horizontal launch scenario aiming 55 degrees water-exit angle needs minimum energy.
- If vertical water-exit is desired, vertical launch from the submarine needs less

energy than that of horizontal launch from the submarine.

5.4.4 Effects of Other Initial and Final Conditions on Cost

The effect of desired water-exit angle on total cost and flight results are investigated in previous sections. In these scenarios, initial and final conditions of forward velocity, time and depth/altitude are fixed. In this section, it is examined how the variations of these conditions affect the cost and flight results. For the launch phase, variations in final forward velocity, initial depth and final time are investigated. For the boost phase, variations in final forward velocity, final altitude and final time are investigated. For all of the cases, cost results for water-exit scenarios of $\theta_{exit} = \{20, 55, 90\}$ are tabulated and shown in the figures. Optimal thrust solutions and the nonlinear 6 DOF simulation results are also given for $\theta_{exit} = 55$ scenarios.

5.4.4.1 Variations in Launch Phase Conditions

Final Forward Velocity Variations

In this case, different final forward velocity scenarios for each water-exit pitch angle of $\theta_f = \{20, 55, 90\}$ are examined. Initial condition is $\boldsymbol{x_0} = [10, 0, 0, 0, 100]^T$ and final conditions are $\boldsymbol{x_f} = [u_f, free, free, \theta_f, 0]^T$. The set of $u_f = \{30, 33, 35, 38\}$ is searched for $\theta_f = 55$ case and the set of $u_f = \{30, 33, 35, 38, 40\}$ is searched for $\theta_f = \{20, 90\}$ cases. The upper limit of the first u_f set is 38 m/s, since it is the largest value that there is still a feasible thrust solution for $\theta_f = 55$ case. Final time is fixed to 15 seconds.

For $\theta_f = 55$ case, obtained optimal thrust solutions, cost change with final forward velocity and the 6 DOF nonlinear simulation results are shown in Figure 5.28. Cost change with final forward velocity for $\theta_f = \{20, 90\}$ cases are shown in Figure 5.29. The data of costs for different final velocities for $\theta_f = \{20, 55, 90\}$ cases are given in Table 5.5.

Results show that as final forward velocity increases, the total energy need increases.

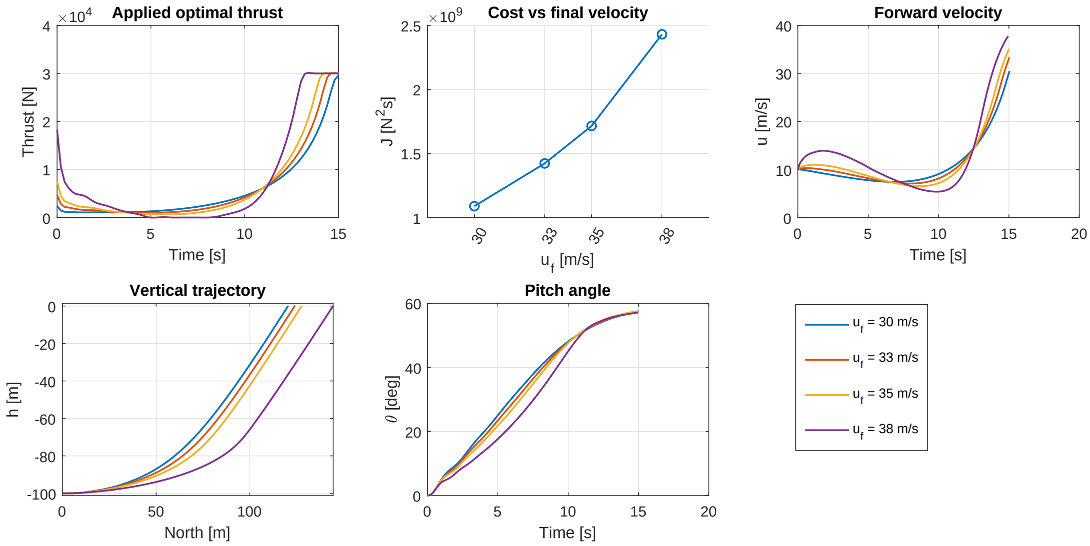

Figure 5.28: Launch phase different final forward velocity scenarios for $\theta_f = 55$ case

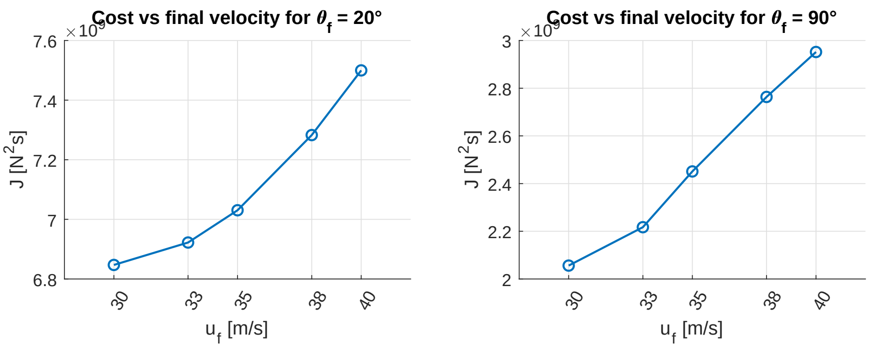

Figure 5.29: Launch phase cost change with final forward velocity for $\theta_f = \{20, 90\}$ cases

$\theta_f(deg)$	20				
$u_f(m/s)$	30	33	35	38	40
$J(\times 10^9 N^2 s)$	6.85	6.92	7.03	7.28	7.50
$\theta_f(deg)$	55				
$u_f(m/s)$	30	33	35	38	-
$J(\times 10^9 N^2 s)$	1.09	1.42	1.72	2.43	-
$\theta_f(deg)$	90				
$u_f(m/s)$	30	33	35	38	40
$J(\times 10^9 N^2 s)$	2.06	2.22	2.45	2.76	2.95

Table 5.5: Launch phase costs for different final velocities for $\theta_f = \{20, 55, 90\}$ cases

Initial Depth Variations

In this case, different initial depth scenarios for each water-exit pitch angle of $\theta_f = \{20, 55, 90\}$ are examined. Initial condition is $\boldsymbol{x_0} = [10, 0, 0, 0, z_0]^T$ and final conditions are $\boldsymbol{x_f} = [35, free, free, \theta_f, 0]^T$. Different sets of z_0 are searched for $\theta_f = \{20, 55, 90\}$ cases. These sets are determined as initial depth values such that there are feasible thrust solutions for them. Final time is fixed to 15 seconds.

For $\theta_f = 55$ case, obtained optimal thrust solutions, cost change with final forward velocity and the 6 DOF nonlinear simulation results are shown in Figure 5.30. Cost change with initial depth for $\theta_f = \{20, 90\}$ cases are shown in Figure 5.31.The data of costs for different initial depths for $\theta_f = \{20, 55, 90\}$ cases are given in Table 5.6.

Results show that it cannot be said that as initial depth increases, the cost increases or decreases. However, there are optimal initial depth values among the searched launch depths, which promise minimum energy need for the examined water-exit angle scenarios.

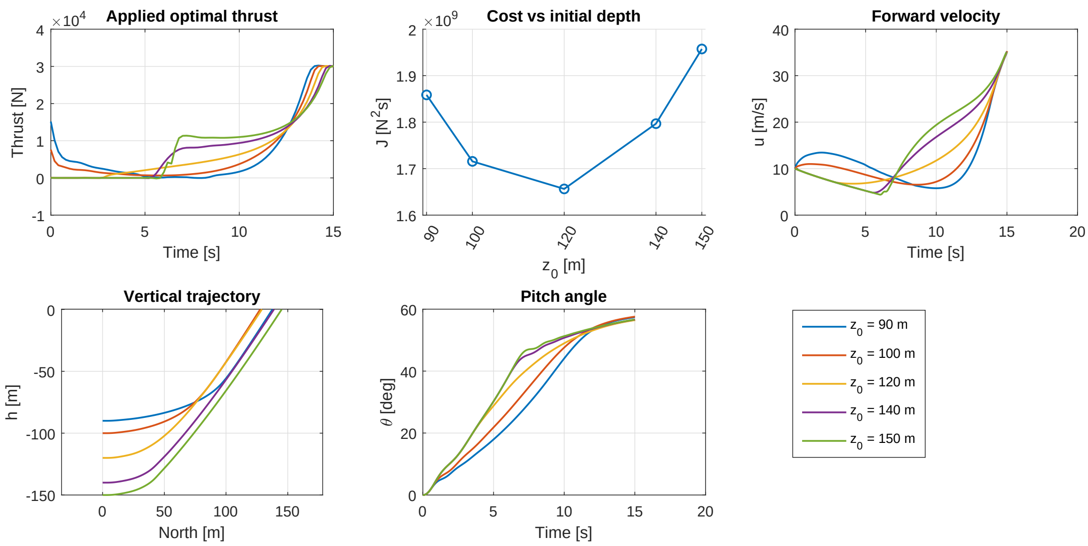

Figure 5.30: Launch phase different initial depth scenarios for $\theta_f = 55$ case

Final Time Variations

In this case, different final time scenarios for each water-exit pitch angle of $\theta_f =$

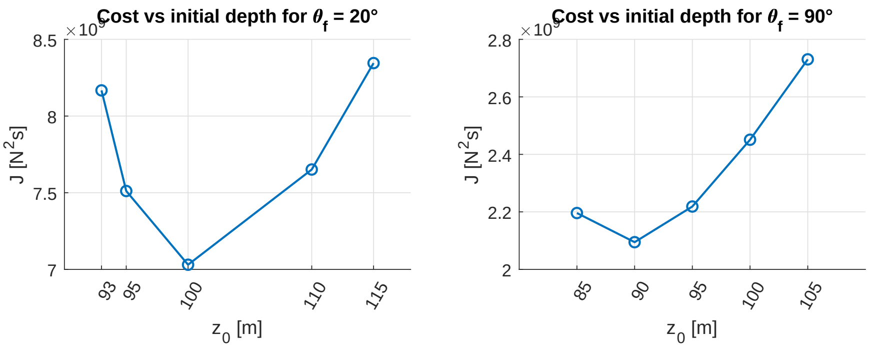

Figure 5.31: Launch phase cost change with initial depth for $\theta_f = \{20, 90\}$ cases

$\theta_f(deg)$	20				
$z_0(m)$	93	95	100	110	115
$J(\times 10^9 N^2 s)$	8.17	7.51	7.03	7.65	8.35
$\theta_f(deg)$	55				
$z_0(m)$	90	100	120	140	150
$J(\times 10^9 N^2 s)$	1.86	1.72	1.66	1.80	1.96
$\theta_f(deg)$	90				
$z_0(m)$	85	90	95	100	105
$J(\times 10^9 N^2 s)$	2.20	2.10	2.22	2.45	2.73

Table 5.6: Launch phase costs for different initial depths for $\theta_f = \{20, 55, 90\}$ cases

$\{20, 55, 90\}$ are examined. Initial condition is $\boldsymbol{x_0} = [10, 0, 0, 0, 100]^T$ and final conditions are $\boldsymbol{x_f} = [35, free, free, \theta_f, 0]^T$. Different sets of t_f are searched for $\theta_f = \{20, 55, 90\}$ cases. These sets are determined as final time values such that there are feasible thrust solutions for them.

For $\theta_f = 55$ case, obtained optimal thrust solutions, cost change with final time and the 6 DOF nonlinear simulation results are shown in Figure 5.32. Cost change with final time for $\theta_f = \{20, 90\}$ cases are shown in Figure 5.33. The data of costs for different final times for $\theta_f = \{20, 55, 90\}$ cases are given in Table 5.7.

Results show that it cannot be said that as final time increases, the cost increases or decreases. However, there are optimal final time values among the searched final time sets, which promise minimum energy need for the examined water-exit angle scenarios.

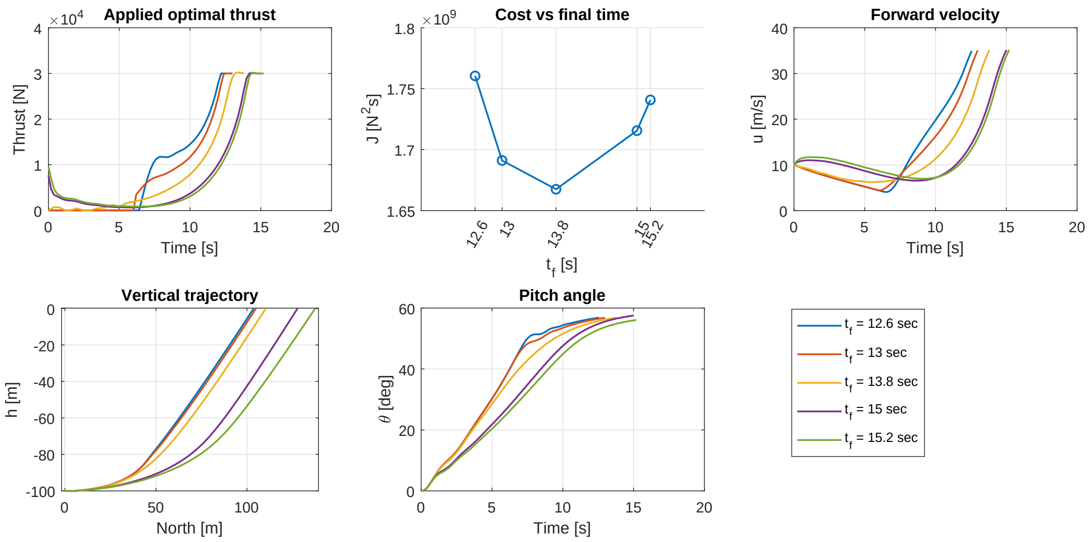

Figure 5.32: Launch phase different final time scenarios for $\theta_f = 55$ case

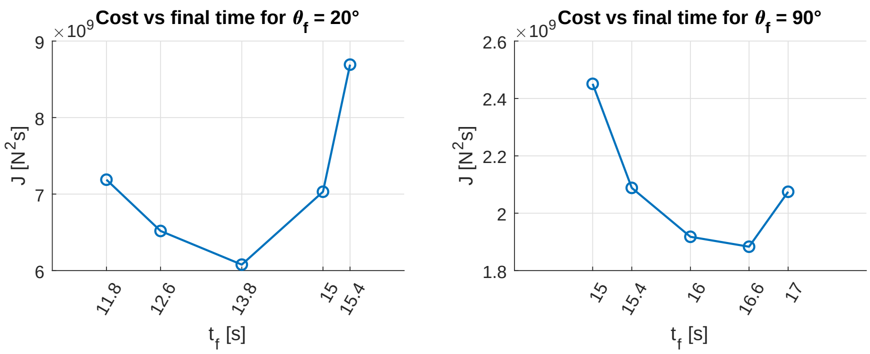

Figure 5.33: Launch phase cost change with final time for $\theta_f = \{20, 90\}$ cases

$\theta_f(deg)$	20				
$t_f(s)$	11.8	12.6	13.8	15.0	15.4
$J(\times 10^9 N^2 s)$	7.19	6.52	6.08	7.03	8.69
$\theta_f(deg)$	55				
$t_f(s)$	12.6	13.0	13.8	15.0	15.2
$J(\times 10^9 N^2 s)$	1.76	1.69	1.67	1.72	1.74
$\theta_f(deg)$	90				
$t_f(s)$	15.0	15.4	16.0	16.6	17.0
$J(\times 10^9 N^2 s)$	2.45	2.09	1.92	1.88	2.08

Table 5.7: Launch phase costs for different final time for $\theta_f = \{20, 55, 90\}$ cases

5.4.4.2 Variations in Boost Phase Conditions

Final Forward Velocity Variations

In this case, different final forward velocity scenarios for each water-exit pitch angle of $\theta_0 = \{20, 55, 90\}$ are examined. Initial condition is $\boldsymbol{x_0} = [35, 0, 0, \theta_0, 0]^T$ and final conditions are $\boldsymbol{x_f} = [u_f, free, free, 0, 600]^T$. Different sets of u_f are searched for $\theta_0 = \{20, 55, 90\}$ cases. These sets are determined as final forward velocity values such that there are feasible thrust and thrust deflection solutions for them.

For $\theta_0 = 55$ case, obtained optimal thrust solutions, cost change with final time and the 6 DOF nonlinear simulation results are shown in Figure 5.34. Cost change with final forward velocity for $\theta_0 = \{20, 90\}$ cases are shown in Figure 5.35. The data of costs for different final velocities for $\theta_0 = \{20, 55, 90\}$ cases are given in Table 5.8.

Results show that as final forward velocity increases, the cost increases.

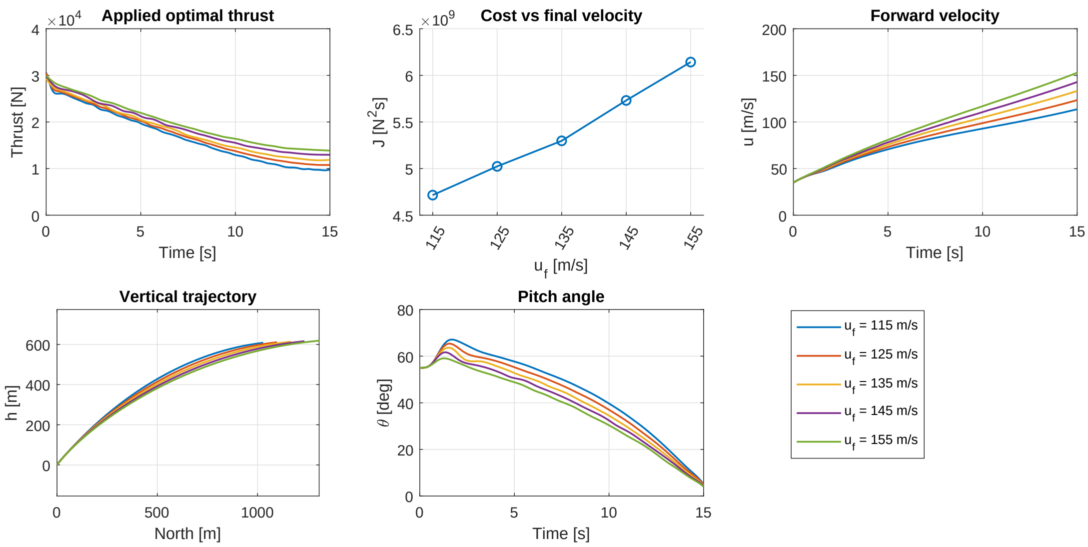

Figure 5.34: Boost phase different final forward velocity scenarios for $\theta_0 = 55$ case

Final Altitude Variations

In this case, different final altitude scenarios for each water-exit pitch angle of $\theta_0 = \{20, 55, 90\}$ are examined. Initial condition is $\boldsymbol{x_0} = [35, 0, 0, \theta_0, 0]^T$ and final con-

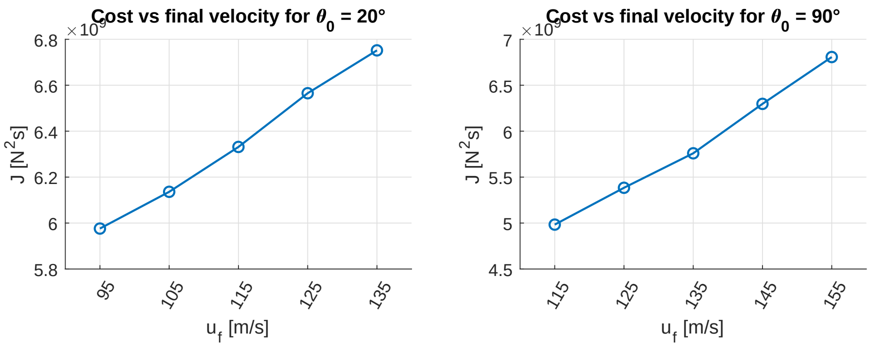

Figure 5.35: Boost phase cost change with final forward velocity for $\theta_0 = \{20, 90\}$ cases

$\theta_0 (deg)$	20				
$u_f (m/s)$	95	105	115	125	135
$J(\times 10^9 N^2 s)$	5.98	6.14	6.33	6.57	6.75
$\theta_0 (deg)$	55				
$u_f (m/s)$	115	125	135	145	155
$J(\times 10^9 N^2 s)$	4.72	5.02	5.30	5.73	6.14
$\theta_0 (deg)$	90				
$u_f (m/s)$	115	125	135	145	155
$J(\times 10^9 N^2 s)$	4.98	5.38	5.76	6.30	6.81

Table 5.8: Boost phase costs for different final velocities for $\theta_0 = \{20, 55, 90\}$ cases

ditions are $\boldsymbol{x_f} = [135, free, free, 0, z_f]^T$. Different sets of z_f are searched for $\theta_0 = \{20, 55, 90\}$ cases. These sets are determined as final altitude values such that there are feasible thrust and thrust deflection solutions for them.

For $\theta_0 = 55$ case, obtained optimal thrust solutions, cost change with final altitude and the 6 DOF nonlinear simulation results are shown in Figure 5.36. Cost change with final altitude for $\theta_0 = \{20, 90\}$ cases are shown in Figure 5.37. The data of costs for different final altitudes for $\theta_0 = \{20, 55, 90\}$ cases are given in Table 5.9.

Results show that as final altitude increases, the cost increases.

Final Time Variations

In this case, different final time scenarios for each water-exit pitch angle of $\theta_0 =$

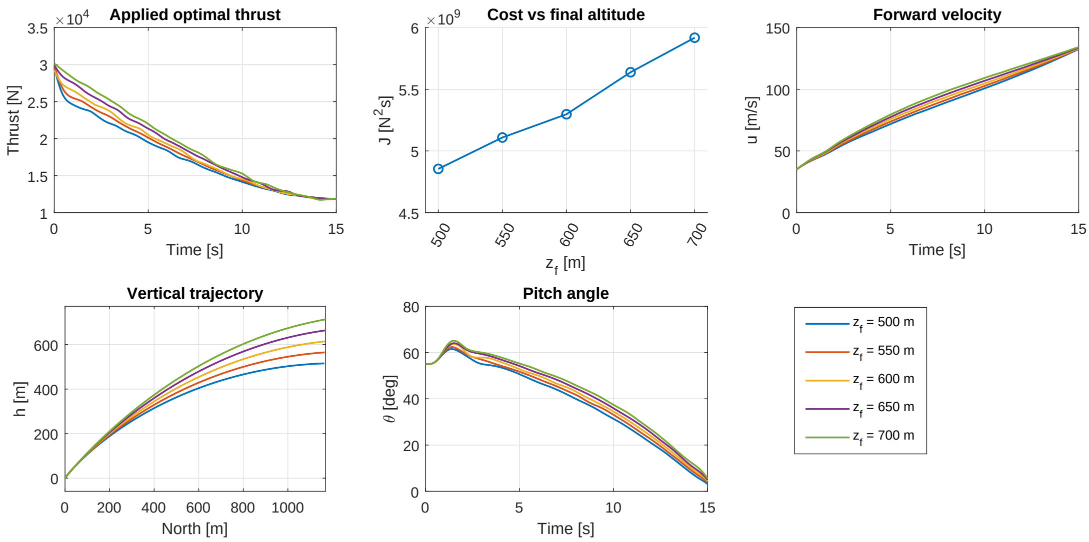

Figure 5.36: Boost phase different final altitude scenarios for $\theta_0 = 55$ case

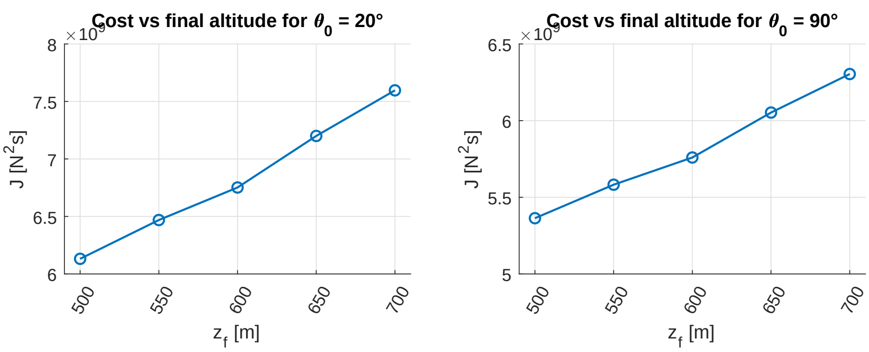

Figure 5.37: Boost phase cost change with final altitude for $\theta_0 = \{20, 90\}$ cases

$\theta_0(deg)$	20				
$z_f(m)$	500	550	600	650	700
$J(\times 10^9 N^2 s)$	6.13	6.47	6.75	7.20	7.60
$\theta_0(deg)$	55				
$z_f(m)$	500	550	600	650	700
$J(\times 10^9 N^2 s)$	4.86	5.11	5.30	5.64	5.92
$\theta_0(deg)$	90				
$z_f(m)$	500	550	600	650	700
$J(\times 10^9 N^2 s)$	5.36	5.58	5.76	6.05	6.30

Table 5.9: Boost phase costs for different final altitudes for $\theta_0 = \{20, 55, 90\}$ cases

$\{20, 55, 90\}$ are examined. Initial condition is $\boldsymbol{x_0} = [35, 0, 0, \theta_0, 0]^T$ and final conditions are $\boldsymbol{x_f} = [135, free, free, 0, 600]^T$. Different sets of t_f are searched for $\theta_0 = \{20, 55, 90\}$ cases. These sets are determined as final time values such that there are feasible thrust and thrust deflection solutions for them.

For $\theta_0 = 55$ case, obtained optimal thrust solutions, cost change with time and the 6 DOF nonlinear simulation results are shown in Figure 5.38. Cost change with final time for $\theta_0 = \{20, 90\}$ cases are shown in Figure 5.39. The data of costs for different final time for $\theta_0 = \{20, 55, 90\}$ cases are given in Table 5.10.

Results show that as final time increases, the cost decreases.

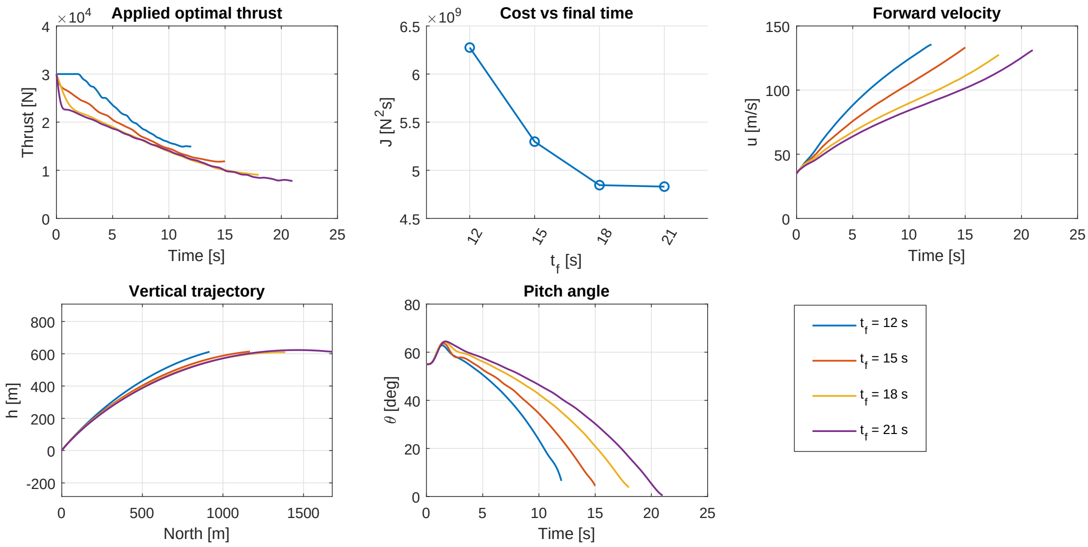

Figure 5.38: Boost phase different final time scenarios for $\theta_0 = 55$ case

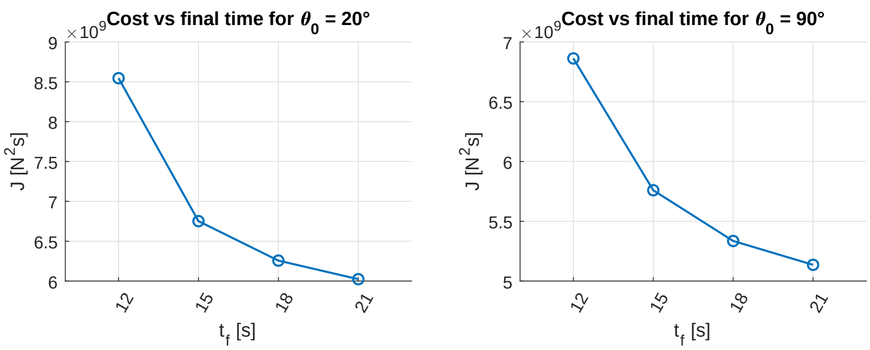

Figure 5.39: Boost phase cost change with final time for $\theta_0 = \{20, 90\}$ cases

$\theta_0(deg)$	20			
$t_f(s)$	12	15	18	21
$J(\times 10^9 N^2 s)$	8.55	6.75	6.26	6.02
$\theta_0(deg)$	55			
$t_f(s)$	12	15	18	21
$J(\times 10^9 N^2 s)$	6.28	5.30	4.85	4.83
$\theta_0(deg)$	90			
$t_f(s)$	12	15	18	21
$J(\times 10^9 N^2 s)$	6.86	5.76	5.34	5.14

Table 5.10: Boost phase costs for different final time for $\theta_0 = \{20, 55, 90\}$ cases

5.4.5 Determination of Optimal Conditions for Launch and Boost Phases

So far, it is looked into how the initial and final conditions of the launch and boost phases affect the total cost and flight results. Using some evidence of that investigation as a starting point, these initial and final conditions can be optimized to obtain a mission profile which needs minimum energy. In the following sections; firstly, optimal initial depth, final forward velocity, and final time conditions are found for the launch phase of horizontal launch. Secondly, optimal final altitude, final forward velocity, and final time conditions are found for the boost phase. These optimal values are found for the water-exit angle set of $\{45, 55, 65\}$ degrees. Then, analyzing the horizontal launch phase and boost phase optimal costs for different water-exit angles together, the optimal water-exit angle is determined. Besides that, optimal initial depth, final forward velocity, and final time conditions are determined for the launch phase of vertical launch.

5.4.5.1 Optimal Conditions for Launch Phase

Horizontal Launch Case

To find optimal final forward velocity value, first the initial conditions are fixed to standard horizontal launch phase conditions, which is $\boldsymbol{x_0} = [10, 0, 0, 0, 100]^T$. As different from the previous cases, final forward velocity is considered as a parameter to be found by optimal control solver. Instead of searching only discrete samples of applied thrust, the optimization algorithm is implemented to search both applied thrust and final forward velocity which minimizes the performance index. Other final conditions are determined as; pitch angle set of $\{45, 55, 65\}$ degrees, zero altitude and free choice of pitch rate and down velocity. It is seen that in the results, independent of the final pitch angle, this method gives the optimal final forward velocity as its allowed minimum value provided to the optimal control solver. This result is consistent with the observation made in Section 5.4.4.1, which states that as final forward velocity increases, the total energy need increases. So, optimal final forward velocity value can be selected according to another limiting factor related to the system or the mission. In this work, it is fixed to 35 m/s.

Different final time conditions are investigated to find optimal final time value. Initial conditions are fixed to $\boldsymbol{x_0} = [10, 0, 0, 0, 100]^T$. Final conditions are fixed to $\boldsymbol{x_f} = [35, free, free, \theta_f, 0]^T$ where θ_f is an element of the set $\{45, 55, 65\}$. Cost change with final time for each water-exit pitch angle scenario are shown in Figure 5.40. The plotted data on the figure is also given in Table 5.11. The final times which provide minimum cost are 13.8, 13.8 and 14.2 seconds for 45, 55 and 65 degrees water-exit pitch angle scenarios, respectively.

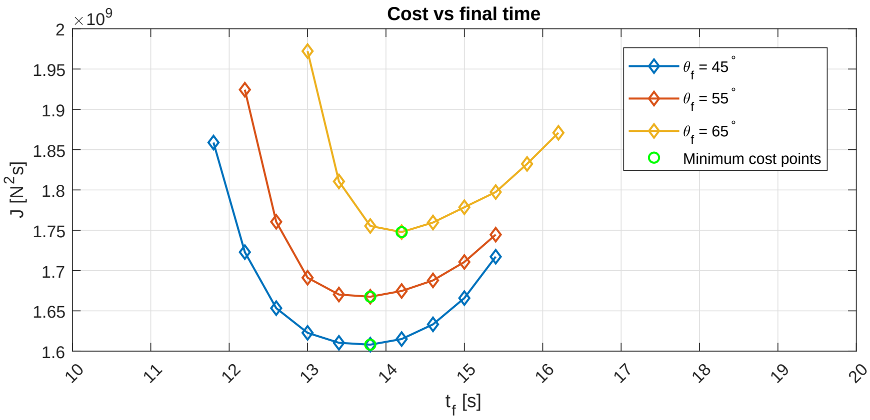

Figure 5.40: Launch phase cost change with final time for $\theta_f = \{45, 55, 65\}$ cases

Optimal initial depth values are searched for the previously found final time values, which provide minimum cost, and in the neighborhood of them. The procedure followed to find optimal final forward velocity is used here, but this time, optimal con-

$\theta_f(deg)$	45									
$t_f(s)$	11.8	12.2	12.6	13.0	13.4	13.8	14.2	14.6	15.0	15.4
$J(\times 10^9 N^2 s)$	1.859	1.723	1.653	1.623	1.610	1.608	1.615	1.633	1.666	1.717
$\theta_f(deg)$	55									
$t_f(s)$	12.2	12.6	13.0	13.4	13.8	14.2	14.6	15.0	15.4	-
$J(\times 10^9 N^2 s)$	1.924	1.761	1.691	1.670	1.668	1.675	1.688	1.711	1.745	-
$\theta_f(deg)$	65									
$t_f(s)$	13.0	13.4	13.8	14.2	14.6	15.0	15.4	15.8	16.2	-
$J(\times 10^9 N^2 s)$	1.972	1.811	1.755	1.748	1.760	1.779	1.797	1.832	1.871	-

Table 5.11: Launch phase costs for different final time, for fixed initial depth, for $\theta_f = \{45, 55, 65\}$ cases

trol solver is implemented to search for applied thrust and initial depth which minimizes the performance index. Initial condition is fixed to $\boldsymbol{x_0} = [10, 0, 0, 0, z_0]^T$ where z_0 is to be found by optimal control solver. Final conditions are fixed to $\boldsymbol{x_f} = [35, free, free, \theta_f, 0]^T$ where θ_f is an element of the set $\{45, 55, 65\}$. In Figure 5.41, cost change with final time for each water-exit pitch angle scenario with fixed initial depth and optimal initial depth are given. The cost data for different water-exit pitch angles with optimal initial depth values are also given in Table 5.12. From the table, it is seen that for given final conditions, the final time and initial depth values which provide minimum cost are, 13.8 seconds and 101.78 meters, 15.2 seconds and 118.75 meters, 18.6 seconds and 149.29 meters for 45, 55 and 65 degrees water-exit pitch angle scenarios, respectively.

Among three different water-exit pitch angle scenarios whose cost is optimal with respect to the initial depth, final forward velocity and final time, 45 degrees pitch angle scenario provides minimum cost. However, to decide which water-exit pitch angle should be chosen as optimal for complete mission profile, it must be analyzed together with boost phase results of the next section.

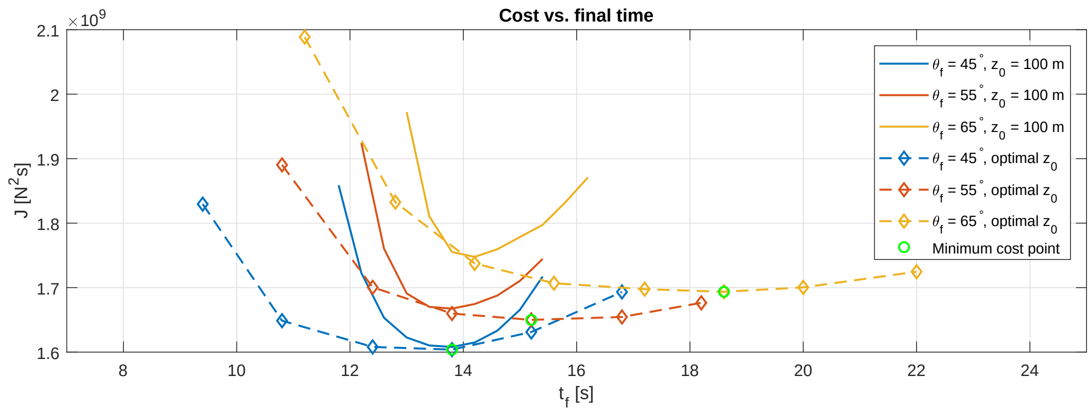

Figure 5.41: Launch phase cost change with final time, for fixed and optimal initial depth, for $\theta_f = \{45, 55, 65\}$ cases

$\theta_f(deg)$	45							
$t_f(s)$	9.4	10.8	12.4	13.8	15.2	16.8	-	-
$z_0(m)$	55.41	70.60	88.93	101.78	112.12	128.22	-	-
$J(\times 10^9 N^2 s)$	1.830	1.649	1.608	1.604	1.631	1.693	-	-
$\theta_f(deg)$	55							
$t_f(s)$	10.8	12.4	13.8	15.2	16.8	18.2	-	-
$z_0(m)$	67.05	88.42	105.38	118.75	131.63	146.15	-	-
$J(\times 10^9 N^2 s)$	1.890	1.701	1.660	1.650	1.655	1.677	-	-
$\theta_f(deg)$	65							
$t_f(s)$	11.2	12.8	14.2	15.6	17.2	18.6	20.0	22.0
$z_0(m)$	60.83	85.84	104.46	121.037	138.77	149.29	163.26	185.57
$J(\times 10^9 N^2 s)$	2.089	1.833	1.738	1.707	1.698	1.694	1.700	1.725

Table 5.12: Launch phase costs for different final time, for optimal initial depth, for $\theta_f = \{45, 55, 65\}$ cases

Vertical Launch Case

When final forward velocity and initial depth values are considered as parameters to be found by optimal control solver, it is seen that the final forward velocity and initial depth values which provide minimum cost are found as their allowed minimum values provided to the optimal control solver. So, final forward velocity and initial depth values are fixed to 35 m/s and 100 meters.

To find the final time value which results with the minimum cost, different final time scenarios are analyzed for initial condition $\boldsymbol{x_0} = [10, 0, 0, 90, 100]^T$ and final condition $\boldsymbol{x_0} = [35, 0, 0, 90, 0]^T$. Cost change with final time for each scenario is shown in Figure 5.42. Cost data for different final time values are also given in Table 5.13. So, the optimal thrust profile that causes 5 seconds of underwater motion results with the minimum energy need.

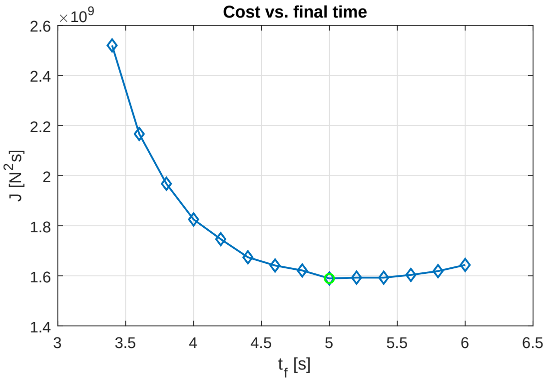

Figure 5.42: Launch (vertical) phase cost change with final time

$\theta_f(deg)$	90						
$t_f(s)$	3.4	3.6	3.8	4.0	4.2	4.4	4.6
$J(\times 10^9 N^2 s)$	2.520	2.167	1.968	1.825	1.747	1.674	1.641
$t_f(s)$	4.8	5.0	5.2	5.4	5.6	5.8	6.0
$J(\times 10^9 N^2 s)$	1.621	1.589	1.593	1.593	1.604	1.619	1.643

Table 5.13: Launch (vertical) phase cost for different final time

5.4.5.2 Optimal Conditions for Boost Phase

In order to find optimal final forward velocity and final altitude values, they are considered as parameters to be found by optimal control solver. The solver is implemented such that it finds discrete samples of applied thrust, thrust deflection, final forward velocity and final altitude values which minimizes the performance index. Initial conditions are defined as $\boldsymbol{x_0} = [35, 0, 0, \theta_0, 0]^T$ where θ_0 is an element of the set $\{45, 55, 65\}$. Final pitch angle condition is fixed to zero, where final pitch rate and down velocity are left as free parameters. In the results, regardless of the initial pitch angle, optimal final forward velocity and final altitude values are found as their allowed minimum values provided to the optimal control solver. This result is consistent with the observation made in Section 5.4.4.2 which states that as final forward velocity increases, the total energy need increases and as final altitude increases, total energy need increases. So, optimal final forward velocity and final altitude values can be selected according to another limiting factor related to the system or the mission. An example of this limiting factor is that, at the beginning of the cruise phase, the missile may need to be in a certain altitude-speed envelope to start the cruise engine. In this work, final forward velocity and final altitude conditions of boost phase are fixed to 135 m/s and 600 m.

The effect of variations in final time on cost is analyzed in Section 5.4.4.2, for the initial condition $\boldsymbol{x_0} = [35, 0, 0, \theta_0, 0]^T$, where θ_0 is an element of the set $\{20, 55, 90\}$, and for the final condition $\boldsymbol{x_f} = [135, 0, 0, 0, 600]^T$. It is observed that as final time increases in an interval such that there is still a feasible optimal control solution, total energy need decreases. So, upper limit of the final time for $\theta_0 = \{45, 55, 65\}$ cases at which there is a feasible solution, can be determined as the optimal final time values. These values are found as 18, 21 and 21 seconds for 45, 55 and 65 degrees water-exit pitch angle cases, respectively. Obtained minimum cost data for different water-exit pitch angles and final time are given in Table 5.14.

Among the three different water-exit pitch angle scenarios whose cost is optimal with respect to the final forward velocity, final altitude and final time, 65 degrees pitch angle scenario provides minimum cost. However, to decide which water-exit pitch angle should be chosen as optimal for complete mission profile, in the next section, it is analyzed together with launch phase results.

$\theta_0(deg)$	45	55	65
$t_f(s)$	18	21	21
$J(\times 10^9 N^2 s)$	5.1551	4.8299	4.8228

Table 5.14: Boost phase minimum costs for $\theta_f = \{45, 55, 65\}$ cases

5.5 Cost Analysis for Overall Design

So far, the optimal inital and final conditions for the launch and boost phases are determined for different water-exit pitch angle scenarios. To decide the optimal water-exit pitch angle condition, the minimum costs obtained for water-exit angles of $\{45, 55, 65\}$ degrees for both launch and boost phases are analyzed in this part. In Figure 5.43, left hand side shows launch phase cost change with final time for optimal initial depth and optimal final forward velocity. Right hand side shows the sum of boost phase minimum costs that are given in Table 5.14 with the costs in left hand side.

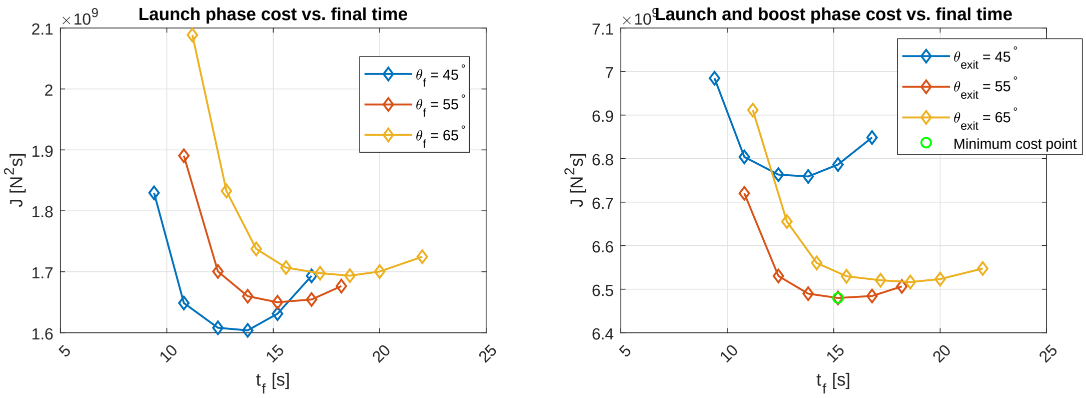

Figure 5.43: Launch phase (in the left) and launch and boost phases (in the right) cost change with final time, for optimal initial depth, for $\theta_f = \{45, 55, 65\}$ cases

So, it is concluded that when launch phase minimum costs and boost phase minimum costs for water-exit pitch angles of $\{45, 55, 65\}$ degrees are added to each other, the minimum cost occurs at 55 degrees water-exit pitch angle.

Optimal thrust profiles which accomplish the minimum energy scenarios for horizontal launch and vertical launch, to be described below, are given in Figure 5.44. The costs related to the given thrust profiles are shown in Table 5.15.

	Launch phase cost($10^9 N^2 s$)	Boost phase cost($10^9 N^2 s$)	Total cost($10^9 N^2 s$)
Horizontal launch case	1.6500	4.8299	6.4799
Vertical launch case	1.5895	5.1358	6.7253

Table 5.15: Optimal costs for horizontal and vertical launch

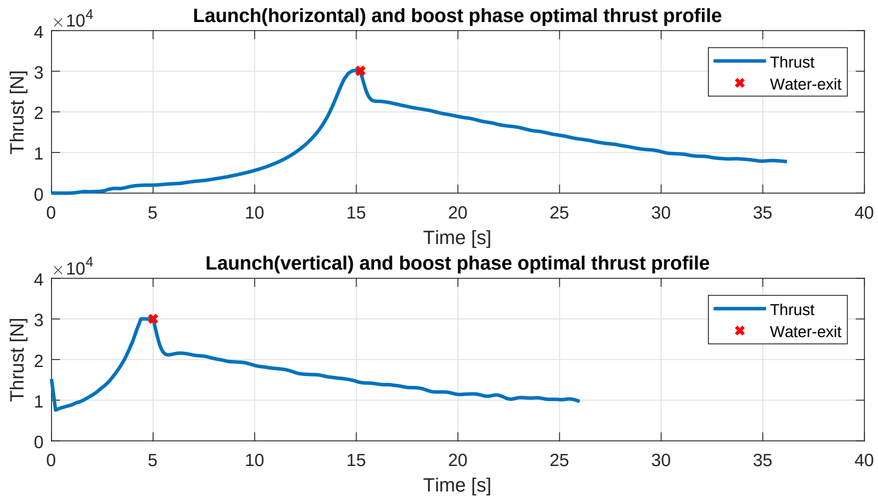

Figure 5.44: Launch (horizontal and vertical) and boost phase optimal thrust solutions

In conclusion, to obtain the minimum total energy scenario for the launch and boost phases, the following initial and final conditions can be defined.

For horizontal launch case, the optimal initial and final conditions of the launch phase which lasts 15.2 seconds are

$$\begin{aligned} \boldsymbol{x_0} &= [10, 0, 0, 0, 118.75]^T \\ \boldsymbol{x_f} &= [35, free, free, 55, 0]^T \end{aligned} \tag{5.39}$$

where the optimal initial and final conditions of the boost phase which lasts 21 seconds are

$$\begin{aligned} \boldsymbol{x_0} &= [35, 0, 0, 55, 0]^T \\ \boldsymbol{x_f} &= [135, free, free, 0, 600]^T \end{aligned} \tag{5.40}$$

For vertical launch case, the optimal initial and final conditions of the launch phase which lasts 5 seconds are

$$\begin{aligned} \boldsymbol{x_0} &= [10, 0, 0, 90, 100]^T \\ \boldsymbol{x_f} &= [35, free, free, 90, 0]^T \end{aligned} \tag{5.41}$$

where the optimal initial and final conditions of the boost phase which lasts 21 seconds are

$$\begin{aligned} \boldsymbol{x_0} &= [35, 0, 0, 90, 0]^T \\ \boldsymbol{x_f} &= [135, free, free, 0, 600]^T \end{aligned} \tag{5.42}$$

In other words, the mission profile for horizontal and vertical launch which need minimum total energy can be described as follows:

For a horizontal launch starting with 10 m/s forward velocity, zero pitch angle, pitch rate and down velocity, the missile is launched at a depth of 118.75 meters to reach the sea surface with 35 m/s forward velocity and 55 degrees pitch angle in 15.2 seconds. Then, boost phase ends with 135 m/s forward velocity, zero pitch angle at 600 m altitude, in 21 seconds.

For a vertical launch starting with 10 m/s forward velocity, zero pitch rate and down velocity at a depth of 100 m, the missile reaches to the sea surface with 35 m/s forward velocity in 5 seconds. Then, boost phase ends with 135 m/s forward velocity, zero pitch angle at 600 m altitude, in 21 seconds.

5.6 Conclusion

In this chapter, firstly, simplified dynamics are obtained for both launch and boost phases, and the mathematical formulations for minimum-effort optimal control problem are presented. To numerically solve the formulated infinite dimensional optimal control problems, they are treated as finite dimensional parameter optimization problems. Optimal control solutions for different water-exit pitch angle scenarios are obtained. After that, the effect of the initial and final conditions on total energy need and simulation results are investigated, and the optimal conditions that result with minimum energy scenarios are found. Finally, the cost analysis for overall design is stated, and the energy-optimal control strategies for horizontal and vertical launch cases are determined.

Considering the overall system, it may be beneficial to note a design consideration.

While deriving the mathematical model of the thrust forces and moments in Chapter 3, it is assumed that the application point of the booster thrust is on the x_b axis of the body frame. In this case, moment arm of the booster thrust vector is defined in the body frame as $\boldsymbol{l}_T = [l_x, l_y, l_z]$ where $l_y = l_z = 0$ and l_x =-3.0903 m. However, this may not be the case in practice, so that l_y and l_z are different from zero and this situation is called as thrust misalignment. As long as the measure of this misalignment is known during the system design, guidance and control design can be performed to compensate this alignment error. However, when the misalignment is unknown during the control system design, practical flight results may differ from the expected results. To simulate this situation where there is an unknown thrust misalignment before the launch, the optimal horizontal launch scenario for launch and boost phases is used. Two different simulations are performed for the aligned and misaligned thrust cases and the results are compared with each other in Figure 5.45. For the misaligned thrust case, moment arm of the booster thrust vector is defined as $\boldsymbol{l}_T = [-3.0903, 0, 0.1]$ meters. Here, l_y is set to zero to avoid the lateral motion as a consequence of the misalignment. However, it should be kept in mind that in practice l_y may also be different from zero and it may result with an undesired roll-yaw motion.

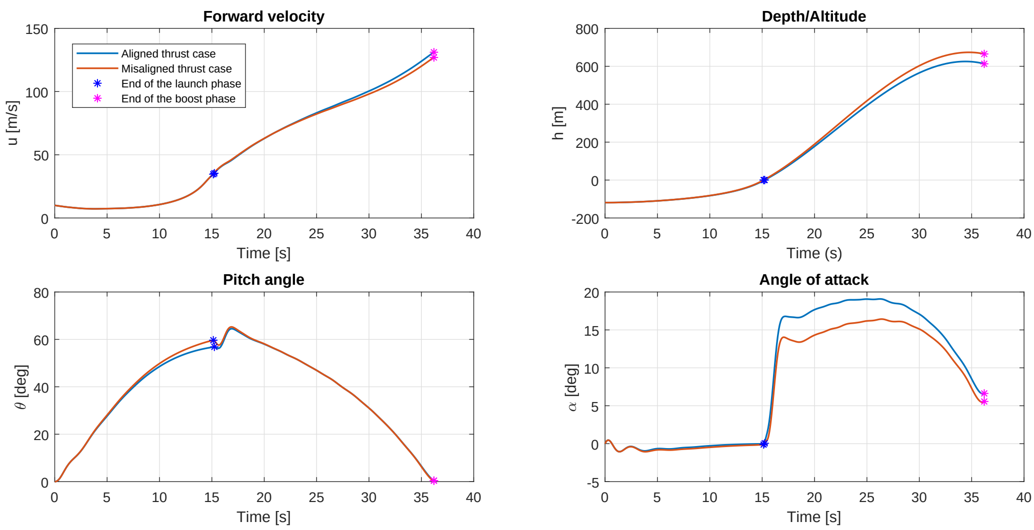

Figure 5.45: Simulation of the aligned and misaligned booster thrust scenarios

From the comparisons, it is seen that forward velocity and angle of attack values during the water-exit and the water-exit time are not much affected by the thrust misalignment. However, water-exit pitch angle is almost 3 degrees larger for the thrust misalignment case, since the positive misalignment in the z_b axis resulted with a larger pitching moment. In the boost phase, since there is a pitch angle autopilot, the pitch angle results are almost the same. On the other hand, there is a distinguishable difference between the angle of attack results. For the thrust misalignment case, final forward velocity is almost 4 m/s smaller, and final altitude is almost 52 meters larger. As a final result, it can be concluded that, although the misaligned thrust scenario results are not much different from the desired results for the examined cases, according to the magnitude of the possible thrust misalignment, some additional control structures or design methodologies may be needed to compensate this alignment errors. For instance, in the case that the differences are not in acceptable levels in the underwater phase, some additional control surfaces and autopilot systems can be used.

CHAPTER 6

AUTOPILOT DESIGN

6.1 Introduction

To control the missile motion from water-exit to target hit, an autopilot system that covers the boost, cruise and terminal phases should be designed. The mission profile of the missile necessitates the control of different flight variables through different phases. While attitude is controlled in the boost phase, altitude and maneuvering are controlled in the cruise phase. Terminal phase needs the control of normal and lateral acceleration that guides the missile through the target, and speed is controlled through the cruise and terminal phases. A common approach during autopilot design is linearizing the nonlinear missile model at some selected equilibrium points from the flight envelope and applying linear control methods at these points. Then, the obtained autopilot gains by linear control methods are tabulated to provide a family of linear controllers which covers the complete flight envelope. During the flight, appropriate autopilot gains are chosen from this tabulated data as a function of the current flight condition, which is called gain scheduling [38]. In this chapter, firstly nonlinear equations of motion are linearized and decoupled for roll, pitch and yaw dynamics. Then, three different cascaded autopilot options are developed in which inner angular rate loops are controlled with PID, LQR or pole-placement based autopilots. For each option, the same outer loop level is controlled with P or PI based autopilots. Design results are presented for both linear and nonlinear models, then the performance comparisons between three different options are made. Some practical design considerations related to the digital implementation are explained. Having integrated the designed autopilots to the missile model by using gain scheduling, two different complete missions from underwater launch to stationary target interception are simulated in the 6 DOF nonlinear simulation environment, and the results are given.

6.2 Linear Equations of Motion

To be able to use linear controller methods, first, the nonlinear equations of motion should be linearized under the appropriate assumptions for trim conditions. In the next sections, the nonlinear dynamics for the missile's second and third flight mode are linearized. For Flight Mode 3 pitch, roll and yaw axis dynamics are linearized, whereas for Flight Mode 2, pitch and roll axis dynamics are linearized. Then, the linearized dynamics are compared with the nonlinear dynamics to show that the assumptions are correct, and the linearized dynamics can be used in the autopilot design process.

6.2.1 Cruise and Terminal Phase Dynamics

To obtain the linear models to be used in cruise phase and terminal phase autopilots; pitch, roll and yaw axis dynamics are linearized in this study. The following assumptions are made for the pitch, roll and yaw axis dynamics:

- Among velocity components (u, v, w), forward velocity, u, is much larger than v and w.
- A constant total velocity, V, is achieved with a speed controller.
- For pitch axis dynamics, roll rate, yaw rate and sideslip angle are zero.
- For roll axis dynamics, pitch rate and yaw rate are zero.
- For yaw axis dynamics, pitch rate and roll rate are zero.

6.2.1.1 Pitch Axis Dynamics

Angle of attack can be approximated as

$$\alpha = \tan^{-1}\left(\frac{w}{u}\right) \approx \frac{w}{u} \tag{6.1}$$

and by taking the derivative it is obtained that:

$$\dot{\alpha} = \frac{\dot{w}u - w\dot{u}}{u^2} \tag{6.2}$$

Substituting rigid-body equations of motion obtained in Chapter 3 into (6.2):

$$\dot{\alpha} = \frac{\dot{w}}{u} = \frac{\frac{Z}{m} + qu}{u} \tag{6.3}$$

and using the linear expressions of aerodynamic forces and moments acting on the missile body, given in (3.79), Z can be written as:

$$\begin{aligned} Z &= QAC_z \\ Z &= QA(C_{z\alpha}\alpha + C_{z\delta_e}\delta_e + C_{zq}q\frac{d}{2V}) \end{aligned} \tag{6.4}$$

angle of attack equation can be written as:

$$\dot{\alpha} = Z_\alpha \alpha + (Z_q + 1)q + Z_{\delta_e}\delta_e \tag{6.5}$$

where

$$Z_\alpha = \frac{QA}{mV}C_{z\alpha} \qquad Z_q = \frac{QA}{mV}\frac{d}{2V}C_{zq} \qquad Z_{\delta_e} = \frac{QA}{mV}C_{z\delta_e} \tag{6.6}$$

Using the given assumptions and rigid-body equations of motion obtained in Chapter

3, derivative of pitch rate can be written as:

$$\dot{q} = \frac{M}{I_y} \tag{6.7}$$

where, M can be defined as:

$$M = QAd(C_{m\alpha}\alpha + C_{m\delta_e}\delta_e + C_{mq}q\frac{d}{2V}) \tag{6.8}$$

Then, pitch rate equation becomes:

$$\dot{q} = M_\alpha\alpha + M_q q + M_{\delta_e}\delta_e \tag{6.9}$$

where

$$M_\alpha = \frac{QAd}{I_y}C_{m\alpha} \qquad M_q = \frac{QAd}{I_y}\frac{d}{2V}C_{mq} \qquad M_{\delta_e} = \frac{QAd}{I_y}C_{m\delta_e} \tag{6.10}$$

6.2.1.2 Roll Axis Dynamics

Sideslip angle can be approximated as:

$$\beta = \sin^{-1}\left(\frac{v}{V}\right) \approx \frac{v}{V} \tag{6.11}$$

and by taking the derivative and substituting rigid-body equations of motion, the result is:

$$\dot{\beta} = \frac{\dot{v}}{V} = \frac{\frac{Y}{m} + wp}{V} \tag{6.12}$$

If linear expression of side force, Y, which acting on the missile body is written as:

$$\begin{aligned} Y &= QAC_y \\ Y &= QA(C_{y\beta}\beta + C_{y\delta_a}\delta_a + C_{yp}p\frac{d}{2V}) \end{aligned} \tag{6.13}$$

then derivative of sideslip angle takes the form of:

$$\dot{\beta} = Y_\beta \beta + Y_p p + Y_{\delta_a} \delta_a \tag{6.14}$$

where

$$Y_\beta = \frac{QA}{mV} C_{y\beta} \qquad Y_p = \frac{QA}{mV} \frac{d}{2V} C_{yp} + \sin(\alpha_0) \qquad Y_{\delta_a} = \frac{QA}{mV} C_{y\delta_a} \tag{6.15}$$

Derivative of roll rate can be written by using the given assumptions and nonlinear motion equations as:

$$\dot{p} = \frac{L}{I_x} \tag{6.16}$$

where, L can be defined as:

$$L = QAd(C_{l\beta}\beta + C_{l\delta_a}\delta_a + C_{lp} p \frac{d}{2V}) \tag{6.17}$$

Then, roll rate equation is:

$$\dot{p} = L_\beta \beta + L_p p + L_{\delta_a} \delta_a \tag{6.18}$$

where

$$L_\beta = \frac{QAd}{I_x} C_{l\beta} \qquad L_p = \frac{QAd}{I_x} \frac{d}{2V} C_{lp} \qquad L_{\delta_a} = \frac{QAd}{I_x} C_{l\delta_a} \tag{6.19}$$

6.2.1.3 Yaw Axis Dynamics

Using the similar procedure that linearization of roll axis dynamics, derivative of sideslip angle can be approximated as:

$$\dot{\beta} = \frac{\dot{v}}{V} = \frac{\frac{Y}{m} - ur}{V} \tag{6.20}$$

This time linear expression of side force, Y, which acting on the missile body is written as:

$$\begin{aligned} Y &= QAC_y \\ Y &= QA(C_{y\beta}\beta + C_{y\delta_r}\delta_r + C_{yr}r\frac{d}{2V}) \end{aligned} \tag{6.21}$$

then derivative of sideslip angle takes the form of:

$$\dot{\beta} = Y_\beta\beta + Y_r r + Y_{\delta_r}\delta_r \tag{6.22}$$

where

$$Y_\beta = \frac{QA}{mV}C_{y\beta} \qquad Y_p = \frac{QA}{mV}\frac{d}{2V}C_{yr} - \cos(\alpha_0) \qquad Y_{\delta_r} = \frac{QA}{mV}C_{y\delta_r} \tag{6.23}$$

Similarly, derivative of yaw rate can be written by using the given assumptions and nonlinear motion equations as:

$$\dot{r} = \frac{N}{I_z} \tag{6.24}$$

where, N can be defined as:

$$N = QAd(C_{n\beta}\beta + C_{n\delta_r}\delta_r + C_{nr}r\frac{d}{2V}) \tag{6.25}$$

Then, yaw rate equation becomes:

$$\dot{r} = N_\beta\beta + N_r r + N_{\delta_r}\delta_r \tag{6.26}$$

where

$$N_\beta = \frac{QAd}{I_z}C_{n\beta} \qquad N_r = \frac{QAd}{I_z}\frac{d}{2V}C_{nr} \qquad N_{\delta_r} = \frac{QAd}{I_z}C_{n\delta_r} \tag{6.27}$$

6.2.2 Boost Phase Dynamics

In this study, the linear models to be used in boost phase autopilots are obtained by linearizing pitch and roll axis dynamics. The following assumptions are made for the considered dynamics:

- Among velocity components (u, v, w), forward velocity, u, is much larger than v and w.
- For pitch axis dynamics, roll rate, yaw rate and sideslip angle are zero.
- For roll axis dynamics, pitch rate and yaw rate are zero.

6.2.2.1 Pitch Axis Dynamics

Following the same procedure that of the linearization for cruise phase pitch axis dynamics, but considering the booster thrust forces and moments, non-constant forward velocity and the absence of fin control, pitch axis dynamics of boost phase are obtained as below:

$$\begin{aligned} \dot{\alpha} &= Z_{T\alpha}\alpha + (Z_{Tq} + 1)q + Z_{\theta_T}\theta_T \\ \dot{q} &= M_{T\alpha}\alpha + M_{Tq}q + M_{\theta_T}\theta_T \end{aligned} \tag{6.28}$$

where

$$\begin{aligned} Z_{T\alpha} &= \frac{QA}{mV}C_{z\alpha} - \frac{\dot{u}}{V} \qquad & Z_{Tq} &= \frac{QA}{mV}\frac{d}{2V}C_{zq} \qquad & Z_{\theta_T} &= \frac{T}{m} \\ M_{T\alpha} &= \frac{QAd}{I_y}C_{m\alpha} \qquad & M_{Tq} &= \frac{QAd}{I_y}\frac{d}{2V}C_{mq} \qquad & M_{\theta_T} &= \frac{Tl_x}{I_y} \end{aligned} \tag{6.29}$$

6.2.2.2 Roll Axis Dynamics

Sideslip angle and roll rate expressions which are derived in Equation (6.14) and Equation (6.18) can be used as linear roll axis dynamics of boost phase.

6.2.3 Comparison Between the Linear and Nonlinear Models

In this section, the previously derived linear dynamics are compared with the nonlinear dynamics such that at a trim condition, a small perturbation is applied to the trim value of the deflection, which may be elevator, rudder, aileron or thrust deflection, then the linear and nonlinear model responses are compared with each other. Figure 6.1 shows the comparisons of pitch and roll dynamics of second flight mode and pitch, roll and yaw dynamics of third flight mode for some selected trim points as an example. The trim conditions which are examined here are given in Table 6.1.

Comparison results show that the linearized model and nonlinear model responses are similar in terms of damping characteristic and steady-state values. Differences can be considered as they are at acceptable levels. It can be concluded that having such similar characteristics for different trim points of each axis dynamics, means that the derived linear models can be used as linear plants of the autopilot design phase.

Axis	Mach	α(deg)	β(deg)	δ(deg)	Angular rate(deg/s)
Pitch (Mode 2)	0.3	4.0	0.0	θ_T=0.0471	q=0.2733
Roll (Mode 2)	0.3	3.0	1.0	δ_a=0.0607	p=1.3423
Pitch (Mode 3)	0.6	4.0	0.0	δ_e=3.3158	q=2.5898
Roll (Mode 3)	0.6	3.0	-1.0	δ_a=-0.1855	p=-2.6821
Yaw (Mode 3)	0.6	3.0	1.0	δ_r=-0.7403	r=-0.0790

Table 6.1: Trim conditions for linear and nonlinear model comparisons of Flight Mode 2 and Flight Mode 3 dynamics

6.3 Design Details

6.3.1 Actuator Models

In the scope of this study, the missile has two dynamically modeled actuators to realize control outputs of control surface deflections and thrust vector deflection. First, control surface deflection angles δ_a, δ_e and δ_r are realized with an actuator system which controls the tail fins. Second, thrust vector deflection angles θ_T and ψ_T are realized with an actuator system, which controls mechanical movable structures like jet vanes, jet tabs or jetavator which inserted into the exhaust jet of the booster mo-

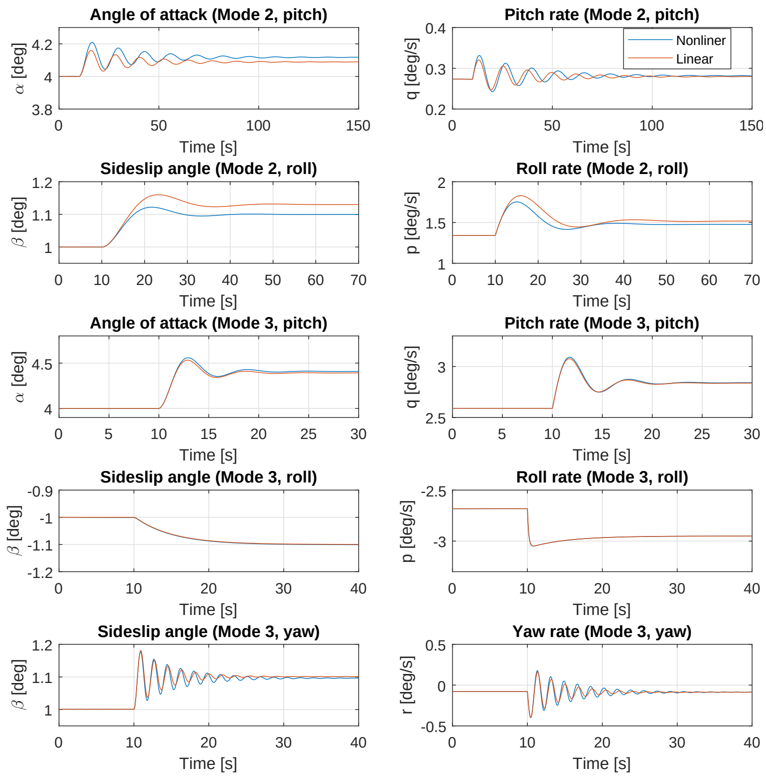

Figure 6.1: Linear and nonlinear model comparisons of Flight Mode 2 and Flight Mode 3 dynamics

tor [39], to provide desired thrust deflection angles. Both actuator systems can be modeled as a standard form second-order transfer function which shows the relationship between the desired deflection angle ($\delta_{ac}, \delta_{ec}, \delta_{rc}, \theta_{Tc}, \psi_{Tc}$) and the realized deflection angle ($\delta_a, \delta_e, \delta_r, \theta_T, \psi_T$). This transfer function is given as:

$$G(s) = \frac{{\omega_n}^2}{s^2 + 2\zeta\omega_n s + {\omega_n}^2} \tag{6.30}$$

where ω_n is natural frequency and ζ is damping ratio whose values are chosen as 157 (rad/s) and 0.7, respectively [40].

6.3.2 Autopilot Structures

In Chapter 2, the mission profile of the missile is divided into four phases which are launch, boost, cruise, and terminal. Control of the launch phase is achieved in Chapter

5 by applying optimal control profiles, without any thrust vector deflection or control surface deflection. Boost, cruise, and terminal phases need the control of different flight variables and these control aims are performed using TVC and tail fin based control in the boost phase, and only tail fin and cruise engine based control in cruise and terminal phases.

Control objectives of each phase are explained as follows. In the boost phase, the aim is to follow a desired pitch angle profile that is found in Chapter 5 and keeping the roll angle at zero. In cruise phase, the missile follows a route that is defined by way-points and flights at a desired altitude. The maneuvers for waypoint navigation will be accomplished by bank-to-turn (BTT) control strategy [41], so roll angle control and keeping zero lateral acceleration in the body frame is necessary during maneuvers [42]. In the terminal phase, the missile navigates through the target by tracking normal acceleration, roll angle, and zero lateral acceleration commands. Furthermore, speed control is desired through the cruise and terminal phases. According to this explanation, the variables to be controlled by the autopilot system are listed below:

- **Boost phase:** Pitch angle, θ, and roll angle, ϕ.
- **Cruise phase:** Missile altitude, h, roll angle, ϕ, lateral acceleration in body frame, A_y, and total velocity, V.
- **Terminal phase:** Normal acceleration in body frame, A_z, roll angle, ϕ, lateral acceleration in body frame, A_y, and total velocity, V.

In this study, cascade control structures are used to control the flight variables which are listed above. In this structure, angular rates are controlled in the inner loop. Pitch angle, roll angle, or acceleration control can be done in the 1st level outer loop. Altitude control will be achieved by adding two more outer loops over the acceleration control loop. Altitude rate and altitude are controlled in these 2nd and 3rd level outer loops of altitude autopilot structure. For example, cascade control block diagrams for pitch angle control and altitude control systems are shown in Figure 6.2 and Figure 6.3.

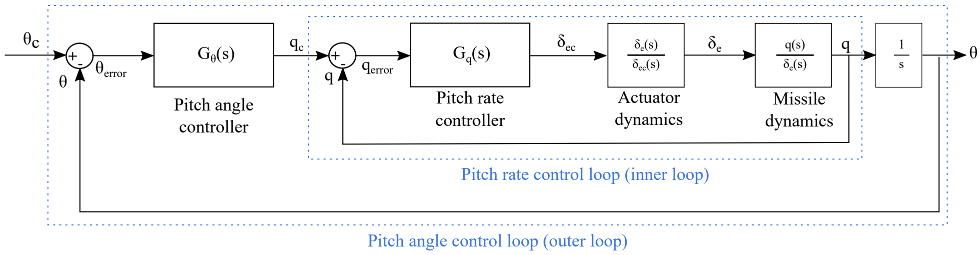

Figure 6.2: Pitch angle and pitch rate cascade control diagram

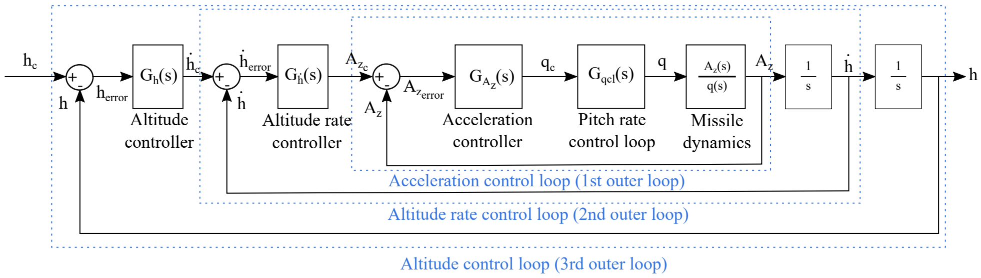

Figure 6.3: Altitude, altitude rate, acceleration and pitch rate cascade control diagram

In this study, pitch rate control loop is established with two different control structures, which are proportional-integral-derivative (PID) based control and state feedback based control. State feedback based control design is performed with two different methods which are linear quadratic regulator (LQR) based and pole placement based. So, for each angular rate controller, three different design options are obtained. Outer loops of each option is designed with the same autopilot structure such that:

- outer loop of pitch angle and roll angle closed control loop is designed with Proportional (P) controller,
- outer loop of normal and lateral acceleration closed control loop is designed with Proportional-Integral (PI) controller,
- 2nd and 3rd level outer loops of altitude closed control loop are designed with Proportional controller.

Selection between the P and PI controller options are based on the necessity of removing steady-state error to a unit step input. The P controller is used where a Type 1 closed-loop system is obtained as if P control is used, and then zero steady-state error is achieved. On the other hand, PI control was needed to make normal and lateral acceleration closed control loop system a Type 1 system.

In Table 6.2, designed autopilots are listed and the resulting three different autopilot options for the overall system are given.

Flight Mode	Control axis	Control loop level	Controlled variable	Option 1	Option 2	Option 3
2	Pitch	Inner loop	Pitch rate (q)	PID	LQ Tracker	Pole placement
		Outer loop	Pitch angle (θ)	P	P	P
	Roll	Inner loop	Roll rate (p)	PID	LQ Tracker	Pole placement
		Outer loop	Roll angle (ϕ)	P	P	P
3	Pitch	Inner loop	Pitch rate (q)	PID	LQ Tracker	Pole placement
		1st outer loop	Nor. acceleration (A_z)	PI	PI	PI
		2nd outer loop	Altitude rate ($\dot{h}$)	P	P	P
		3rd outer loop	Altitude (h)	P	P	P
	Roll	Inner loop	Roll rate (p)	PID	LQ Tracker	Pole placement
		Outer loop	Roll angle (ϕ)	P	P	P
	Yaw	Inner loop	Yaw rate (r)	PID	LQ Tracker	Pole placement
		Outer loop	Later. acceleration (A_y)	PI	PI	PI

Table 6.2: Autopilot structures and overall autopilot system options

For cruise and terminal phases, a single Proportional total velocity controller is used for all flight conditions, with the proportional gain of $K_p = 2$ [35].

Cruise phase's vertical acceleration command, and terminal phase's horizontal and vertical acceleration commands are found by using proportional navigation guidance method given in [40]. Vertical and horizontal acceleration commands are found for the Earth-fixed frame, and then translated into the commands of roll angle and normal acceleration in body frame.

In the following section, the reasons for PID control and state feedback control selections for inner angular rate loops are explained. Also, they are mathematically explained, and control system block diagrams for both control architectures are given.

6.3.2.1 PID Control

PID control strategy is well studied in control literature and it is commonly used since most control problems can be solved by PID controllers [43]. It is able to provide a good cost/benefit ratio and although it is relatively simple to implement, satisfactory performance is achieved in many control tasks [44]. So, one of the three control system options in this study is based on PID controlled angular rates in the inner loops.

In the general form of PID controllers, the relationship between the control signal, $u(t)$, and the error signal, $e(t)$, which is the difference between the desired set point and the measured output, can be shown as following:

$$u(t) = K_p e(t) + K_i \int e(t)dt + K_d \frac{de(t)}{dt} \tag{6.31}$$

where K_p, K_i and K_d are proportional, integral and derivative gain parameters to be tuned according to the desired control performance in time and/or frequency domain.

In Figure 6.4, block diagram of pitch rate control system which is based on PID controller is given.

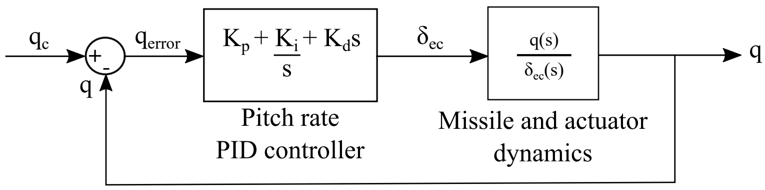

Figure 6.4: Pitch rate control system based on PID controller

6.3.2.2 State Feedback Control

Considering a linear time invariant control system

$$\begin{aligned} \dot{\boldsymbol{x}} &= \boldsymbol{A}\boldsymbol{x} + \boldsymbol{B}u \\ y &= \boldsymbol{C}\boldsymbol{x} \end{aligned} \tag{6.32}$$

where $\boldsymbol{x}$ is state vector (n-vector), y is output signal (scalar), u is control signal (scalar) and $\boldsymbol{A}$, $\boldsymbol{B}$ and $\boldsymbol{C}$ are $n \times n$, $n \times 1$ and $1 \times n$ consant matrices, control signal can be chosen as

$$u = -\boldsymbol{K}\boldsymbol{x} \tag{6.33}$$

where $1 \times n$ matrix $\boldsymbol{K}$ is called the state feedback gain matrix and such a control scheme is called state feedback control [45]. State feedback control can be applied where all states are available for feedback. Both the pole placement method and linear quadratic optimal control method can be used to obtain the state feedback gain matrix. These methods constitute the second and third control system options in this study.

Linear Quadratic Regulator

Generally a good performance characteristics and stability margins are provided with linear quadratic regulator (LQR) design [46], [47]. Applying LQR design method provides a balance between the desire to regulate perturbations in the state and the size of the control signals needed to do so [48]. With this method, a unique, stabilizing and optimal controller can be found for a linearized system when this system is completely state controllable. Also, guaranteed levels of stability can be described as; upward gain margin is infinite, downward gain margin is at least 1/2 and phase margin is at least $\pm$ 60 degrees [43].

For a controllable system given in the form of Equation (6.32), a quadratic performance index

$$J = \frac{1}{2}\int_0^\infty (\boldsymbol{x}^T\boldsymbol{Q}\boldsymbol{x} + u^T R u)dt \tag{6.34}$$

where $\boldsymbol{Q}$ is an $n \times n$ real symmetric semi positive definite matrix and R is positive definite scalar, can be minimized with a unique and optimal control u as given in the form of Equation (6.33). Here, state feedback gain matrix is defined as

$$\boldsymbol{K} = R^{-1}\boldsymbol{B}^T\boldsymbol{S} \tag{6.35}$$

where $\boldsymbol{S}$ is the unique, symmetric, semi positive definite solution of the Algebraic Riccati Equation (ARE) which is stated as

$$\boldsymbol{SA} + \boldsymbol{A^T S} - \boldsymbol{SB}R^{-1}\boldsymbol{B^T S} + \boldsymbol{Q} = \boldsymbol{0} \tag{6.36}$$

The control u which minimizes (6.34), transfers the state vector $\boldsymbol{x}(t = 0)$ to zero while t goes to infinity, thus stability of the closed-loop system is achieved. Presented LQR structure can be modified to have a solution for tracking problem in which a given nonzero reference input trajectory $\boldsymbol{r}(t)$ is followed [48]. To perform this aim, the system in (6.32) is modified such that

$$\begin{aligned}
&\underbrace{\begin{bmatrix} \dot{\boldsymbol{x}} \\ \dot{\boldsymbol{\varepsilon}} \end{bmatrix}}_{\bar{\boldsymbol{x}}} = \underbrace{\begin{bmatrix} \boldsymbol{A} & 0 \\ -\boldsymbol{C} & 0 \end{bmatrix}}_{\bar{\boldsymbol{A}}} \begin{bmatrix} \boldsymbol{x} \\ \boldsymbol{\varepsilon} \end{bmatrix} + \underbrace{\begin{bmatrix} \boldsymbol{B} \\ 0 \end{bmatrix}}_{\bar{\boldsymbol{B}}} u + \underbrace{\begin{bmatrix} 0 \\ \boldsymbol{I} \end{bmatrix}}_{\bar{\boldsymbol{G}}} \boldsymbol{r} \\
&\boldsymbol{y} = \boldsymbol{C}\boldsymbol{x} \\
&\boldsymbol{u} = -\boldsymbol{K}\boldsymbol{x} - \boldsymbol{k_I}\boldsymbol{\varepsilon}, \quad \boldsymbol{K_T} = [\boldsymbol{K} \quad \boldsymbol{k_I}]
\end{aligned} \tag{6.37}$$

where the integral of the tracking error is defined as a new state variable, $\boldsymbol{\varepsilon}$, and $\boldsymbol{r}$ is the reference trajectory. Then the performance index in (6.34) is modified as:

$$J = \frac{1}{2}\int_0^\infty (\bar{\boldsymbol{x}}^T \boldsymbol{Q} \bar{\boldsymbol{x}} + u^T R u) dt \tag{6.38}$$

Thus, the modified state vector and system representation becomes:

$$\boldsymbol{z} = [\boldsymbol{x} \quad \boldsymbol{\varepsilon}]^T \tag{6.39}$$

$$\dot{\boldsymbol{z}} = \bar{\boldsymbol{A}}\boldsymbol{z} + \bar{\boldsymbol{B}}\boldsymbol{u} + \bar{\boldsymbol{G}}\boldsymbol{r} \tag{6.40}$$

$$\boldsymbol{u} = -\boldsymbol{K_T}\boldsymbol{z} \tag{6.41}$$

State feedback gain matrix $\boldsymbol{K_T}$ can be found with the method explained in the previous part. With this design, $\boldsymbol{z}(t)$ converges to zero, meaning that integral of the tracking error also converges to zero. Obtained closed-loop system is given below:

$$\dot{\boldsymbol{z}} = (\bar{\boldsymbol{A}} - \bar{\boldsymbol{B}}\boldsymbol{K_T})\boldsymbol{z} + \bar{\boldsymbol{G}}\boldsymbol{r} \tag{6.42}$$

In conclusion, design parameters of LQR based state feedback control are $\boldsymbol{Q}$ and R. Elements of these matrices are tuned to obtain desired control performance in time and/or frequency domain.

Pole Placement

Having assumed that the all state variables of system given in (6.40) are available for feedback and the system is completely state controllable, then by using an appropriate state feedback gain matrix, the closed-loop system poles may be placed at any desired locations. Pole locations can be determined based on the control system specifications in time and/or frequency domain. After the closed-loop poles are chosen, state feedback gain matrix can be found via different approaches. One method is equating $|s\boldsymbol{I} - \bar{\boldsymbol{A}} + \bar{\boldsymbol{B}}\boldsymbol{K_T}|$ with the desired characteristic equation and solving for $\boldsymbol{K_T}$. Other well known method is to use Ackermann's formula [45].

In accordance with the representation given in (6.40), for instance, pitch axis dynamics of cruise and terminal phase, including actuator dynamics, where the aim is to control pitch rate, can be described in state space form as follows:

$$\begin{bmatrix} \dot{\alpha} \\ \dot{q} \\ \dot{\delta}_e \\ \ddot{\delta}_e \\ e_q \end{bmatrix} = \begin{bmatrix} Z_\alpha & Z_q + 1 & Z_{\delta_e} & 0 & 0 \\ M_\alpha & M_q & M_{\delta_e} & 0 & 0 \\ 0 & 0 & 0 & 1 & 0 \\ 0 & 0 & -\omega_n^2 & -2\zeta\omega_n & 0 \\ 0 & -1 & 0 & 0 & 0 \end{bmatrix} \begin{bmatrix} \alpha \\ q \\ \delta_e \\ \dot{\delta}_e \\ \int e_q \end{bmatrix} + \begin{bmatrix} 0 \\ 0 \\ 0 \\ \omega_n^2 \\ 0 \end{bmatrix} \delta_{ec} \tag{6.43}$$

where e_q is the pitch rate tracking error. Block diagram of pitch rate control system based on state feedback control is given in Figure 6.5,

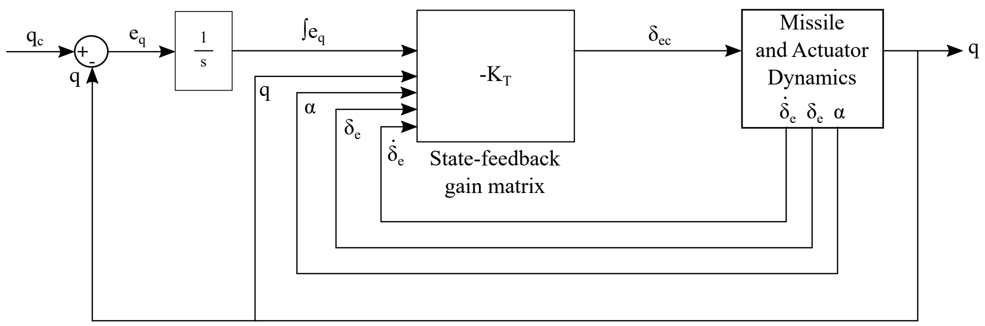

Figure 6.5: Pitch rate control system based on state feedback control

6.3.3 Design Criteria and Design Methods

Design Criteria

Time and/or frequency domain performance specifications of the autopilots are determined as follows:

For angular rate control loops of Flight Mode 2, it is aimed that system response to step input have a minimum sum of rise time, T_r, and settling time, T_s, while overshoot, OS, is less than 5$\%$, gain cross-over frequency, ω_{gc}, is larger than the natural frequency of the concerned open loop dynamics and smaller than 8.33 rad/s for pitch axis dynamics and 52.33 rad/s for roll axis dynamics. Maximum frequency value is chosen based on a classical rule of thumb, which is choosing the maximum cross-over frequency to be about one-third the frequency of the dynamics which does not needed to be controlled, that is actuator dynamics in this case [49]. Outer pitch and roll angle loops are designed such that the aim is to minimize sum of rise time and settling time, while overshoot is less than 0.1%.

Angular rate control loops of Flight Mode 3 are designed with the same criteria that of Flight Mode 2, except that the allowed maximum overshoot is 10%. In the outer loops, normal and lateral accelerations are designed so that sum of rise time and settling time is minimized while gain margin, GM, is larger than 10 dB and phase margin, PM, is larger than 45°. Outer altitude rate and altitude loops are designed to obtain minimum sum of rise time and settling time, while overshoot is less then 5% and $\%0.1$, respectively. Roll angle outer loop is designed in the same way of Flight Mode 2's roll angle loop design.

Design specifications for each autopilot are summarized in Table 6.3

Design Method

Given that the design criteria in the previous part, PID controller's gain parameters K_p, K_d, K_i, LQR based controller's state weighing matrices $\boldsymbol{Q}, R$ and desired pole locations for pole placement method should be determined. For PID and LQR based control, this design problem is solved by using constrained optimization. For the pole placement method, the dominant pole approach is used.

In the constrained optimization method, cost functions to be minimized are defined as the sum of closed-loop step response rise time and settling time of concerned dynamics, as it is explained in design specifications together with the constraints. An interior-point method based algorithm is used to solve the formulated constrained optimization problem of each autopilot.

In LQR based control, design parameters are described such that $\boldsymbol{Q}$ is diagonal with non-zero elements correspond with the controlled states, and input weighing matrix R is 1. As an example, state vectors and design parameters related to pitch and roll dynamics are given as:

$$
\begin{aligned}
&Pitch: \\
&\boldsymbol{x} = \begin{bmatrix} \alpha & q & \delta_e & \dot{\delta}_e & \int e_q \end{bmatrix}^T \\
&\boldsymbol{Q} = \begin{bmatrix} 0 & 0 & 0 & 0 & 0 \\ 0 & 0 & 0 & 0 & 0 \\ 0 & 0 & 0 & 0 & 0 \\ 0 & 0 & 0 & 0 & 0 \\ 0 & 0 & 0 & 0 & q_1 \end{bmatrix} \quad R = 1 \\
&Roll: \\
&\boldsymbol{x} = \begin{bmatrix} \beta & p & \delta_a & \dot{\delta}_a & \int e_p \end{bmatrix}^T \\
&\boldsymbol{Q} = \begin{bmatrix} q_1 & 0 & 0 & 0 & 0 \\ 0 & 0 & 0 & 0 & 0 \\ 0 & 0 & 0 & 0 & 0 \\ 0 & 0 & 0 & 0 & 0 \\ 0 & 0 & 0 & 0 & q_2 \end{bmatrix} \quad R = 1
\end{aligned}
\tag{6.44}
$$

In conclusion, for LQR based control, constrained optimization algorithm will find the design parameters of q_1 for pitch rate dynamics and q_1 and q_2 for roll rate dynamics. It should be noted that for roll/yaw dynamics, although sideslip angle, β, is not a directly controlled state, it is also weighed since regulating β around zero is a desirable performance result.

In dominant pole approach, if the ratios of the real parts of the closed-loop poles

Flight Mode 2			
Pitch axis autopilots		Roll axis autopilots	
Pitch rate	Pitch angle	Roll rate	Roll angle
Minimum $(T_r + T_s)$ s.t. OS < 5% $\omega_{gc} > \omega_{n,pitch}$ ω_{gc} < 8.33 (rad/s)	Minimum $(T_r + T_s)$ s.t. OS < 0.1%	Minimum $(T_r + T_s)$ s.t. OS < 5% $\omega_{gc} > \omega_{n,roll}$ ω_{gc} < 52.33 (rad/s)	Minimum $(T_r + T_s)$ s.t. OS < 0.1%
Flight Mode 3			
Pitch axis autopilots			
Pitch rate	Normal acceleration	Altitude rate	Altitude
Minimum $(T_r + T_s)$ s.t. OS < 10% $\omega_{gc} > \omega_{n,pitch}$ ω_{gc} < 8.33 (rad/s)	Minimum $(T_r + T_s)$ s.t. GM > 10 (dB) PM > 45°	Minimum $(T_r + T_s)$ s.t. OS < 5%	Minimum $(T_r + T_s)$ s.t. OS < 0.1%
Roll axis autopilots		Yaw axis autopilots	
Roll rate	Roll angle	Yaw rate	Lateral acceleration
Minimum $(T_r + T_s)$ s.t. OS < 10% $\omega_{gc} > \omega_{n,roll}$ ω_{gc} < 52.33 (rad/s)	Minimum $(T_r + T_s)$ s.t. OS < 0.1%	Minimum $(T_r + T_s)$ s.t. OS < 10% $\omega_{gc} > \omega_{n,yaw}$ ω_{gc} < 52.33 (rad/s)	Minimum $(T_r + T_s)$ s.t. GM > 10 (dB) PM > 45°

Table 6.3: Autopilot design specifications

exceed 5 and there are no zeros nearby, then the closed-loop poles nearest to the imaginary axis will dominate in the transient response behavior, and quite often they occur in the form of a complex-conjugate pair [45]. Thus, by choosing dominant closed-loop pole locations according to autopilot design specifications, design with pole placement can be performed. If dominant closed-loop pole locations are

$$s_{1,2} = -\sigma \pm j\omega_d \tag{6.45}$$

where

$$\begin{aligned} \sigma &= \zeta\omega_n \\ \omega_d &= \omega_n\sqrt{1-\zeta^2} \\ \beta &= -\tan^{-1}\left(\frac{\omega_d}{\sigma}\right) \end{aligned} \tag{6.46}$$

and ω_n and ζ are natural frequency and damping ratio of the closed-loop system, then the closed-loop system can be approximated as a second-order system. For a second-order system, transient-response specifications for maximum (percent) overshoot, M_p, settling time (with 2% criterion), T_s, and rise time, T_r are given as:

$$\begin{aligned} M_p &= e^{-(\zeta/\sqrt{1-\zeta^2})\pi} \\ T_s &= \frac{4}{\zeta\omega_n} \\ T_r &= \frac{\pi-\beta}{\omega_d} \end{aligned} \tag{6.47}$$

Using these expressions, ζ and ω_n parameters can be found to satisfy maximum overshoot and gain crossover frequency specifications of the autopilots. By choosing ω_n in this way, for a fixed ζ, settling time and rise time are minimized, as it is desired in the autopilot design specifications. Since the open loop system representations for pitch, roll, and yaw dynamics are fifth order, there are three remaining poles to be determined. Two of them are the same poles as the open loop poles that correspond to the actuator dynamics. These poles are much away from the imaginary axis with large negative real parts, and their contribution to the transient response can be neglected. In the study, all the angular rate open loop transfer functions have two zeros, which one is located at zero, and the other one is negative real. One remaining pole is chosen such that negative open loop zero is canceled in the closed-loop system.

6.4 Design Results

Using the design methods explained in the previous section, boost phase and cruise/terminal phase autopilots are designed for the selected design points. In this section, firstly, linear model design results for selected points are given. Then, the autopilot performances are tested in the 6 DOF nonlinear simulation model.

6.4.1 Pitch Axis Autopilots

6.4.1.1 Flight Mode 2

Pitch rate and pitch angle autopilot design steps are explained for the following flight condition: {Mach = 0.3, α = 10°, β = 0°, h = 500 m, $\dot{u}$ = 10 m/s^2}. With the aerodynamic data of the given flight condition, open loop transfer function which relates the thrust deflection command and pitch rate is found as:

$$\frac{q(s)}{\theta_{Tc}(s)} = \frac{4.18 \times 10^5 s^2 + 6.885 \times 10^4 s}{s^5 + 220.1 s^4 + 2.471 \times 10^4 s^3 + 4158 s^2 + 3438 s} \tag{6.48}$$

Pole and zero locations of this system are:

$$\begin{aligned} p_1 &= 0 \\ p_{2,3} &= -109.96 \pm j112.18 \\ p_{4,5} &= -0.083639 \pm j0.36381 \\ z_1 &= 0 \\ z_2 &= -0.16471 \end{aligned} \tag{6.49}$$

Using the design methods explained in the previous section, for pitch rate control, PID gains are found as;

$$K_p = 0.4892 \quad K_i = 0.3032 \quad K_d = 0 \tag{6.50}$$

LQR design parameter q_1 and resulting gain matrix $\boldsymbol{K}$ are found as;

$$q_1 = 2.8889 \quad \boldsymbol{K} = [-0.0087, 0.4619, 0.0686, 0.0003, -1.6997] \tag{6.51}$$

For the pole placement method, desired closed-loop pole locations and the resulting gain matrix are determined as:

$$\begin{aligned} p_1 &= -0.16471 \\ p_{2,3} &= -109.96 \pm j112.18 \\ p_{4,5} &= -3.7604 \pm 3.9435i \\ \boldsymbol{K} &= [-0.0088, 0.4594, 0.0682, 0.0003, -1.7525] \end{aligned} \tag{6.52}$$

Having found the pitch rate controllers, pitch angle open loop transfer functions can be obtained for PID, LQR, and pole-placement based options. Since the number of integrators in the pitch angle open loop transfer function is 1, a type 1 closed-loop system can be obtained using the proportional controller to complete outer pitch angle loop, then the steady state error to a unit step input will be zero for pitch angle control system. For PID, LQR and pole-placement based inner pitch rate loops, pitch angle controller proportional gains are found as:

$$K_{p,PID} = 2.8656 \quad K_{p,LQR} = 1.4292 \quad K_{p,pole-placement} = 1.4777 \tag{6.53}$$

In conclusion, pitch angle control loop is completed. In Figure 6.6, pitch angle and pitch rate step responses of the linear closed-loop system are given. In Table 6.4 controller gains and time and frequency domain results are given. The performance of pitch axis autopilots, which are designed at different flight conditions, are tested in the 6 DOF nonlinear simulation environment by using gain scheduling during flight. Simulation results are given in Figure 6.7. Design results on linear system show that the design specifications are achieved and autopilot performance in nonlinear simulation is satisfactory.

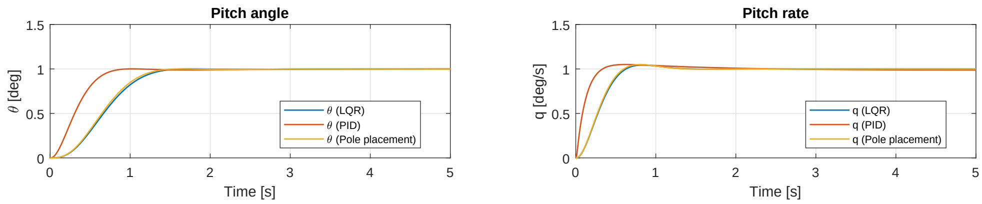

Figure 6.6: Flight Mode 2, linear pitch axis closed-loop system step responses

Option 1 (PID)	Option 2 (LQR)	Option 3 (Pole placement)
	Pitch rate loop	
$K_p = 0.4892$, $K_i = 0.3032$ $K_d = 0$	$\boldsymbol{K}$ = [-0.0087, 0.4619, 0.0686, 0.0003, -1.6997]	$\boldsymbol{K}$ = [-0.0088, 0.4594, 0.0682, 0.0003, -1.7525]
$T_s(s) = 0.2688$ $T_r(s) = 0.2273$ $OS(\%) = 5.0000$	$T_s(s) = 0.5539$ $T_r(s) = 0.5027$ $OS(\%) = 4.3819$	$T_s(s) = 0.5339$ $T_r(s) = 0.4863$ $OS(\%) = 4.9997$
$GM(dB) = 28.4270$ $PM(°) = 81.5073$ $\omega_{gc}(rad/s) = 8.3300$ $\omega_{n,pitch}(rad/s) = 0.3733$	$GM(dB) = \infty$ $PM(°) = 65.5734$ $\omega_{gc}(rad/s) = 8.3300$ $\omega_{n,pitch}(rad/s) = 0.3733$	$GM(dB) = \infty$ $PM(°) = 64.7562$ $\omega_{gc}(rad/s) = 8.3297$ $\omega_{n,pitch}(rad/s) = 0.3733$
	Pitch angle loop	
$K_p = 2.8656$	$K_p = 1.4292$	$K_p = 1.4777$
$T_s(s) = 0.6951$ $T_r(s) = 0.6058$ $OS(\%) = 0.1000$	$T_s(s) = 1.2649$ $T_r(s) = 1.1339$ $OS(\%) = 0.1000$	$T_s(s) = 1.2116$ $T_r(s) = 1.0889$ $OS(\%) = 0.1000$
$GM(dB) = 30.8492$ $PM(°) = 70.2626$	$GM(dB) = 13.9227$ $PM(°) = 67.3041$	$GM(dB) = 13.5790$ $PM(°) = 67.2281$

Table 6.4: Flight Mode 2, linear pitch axis autopilot design results

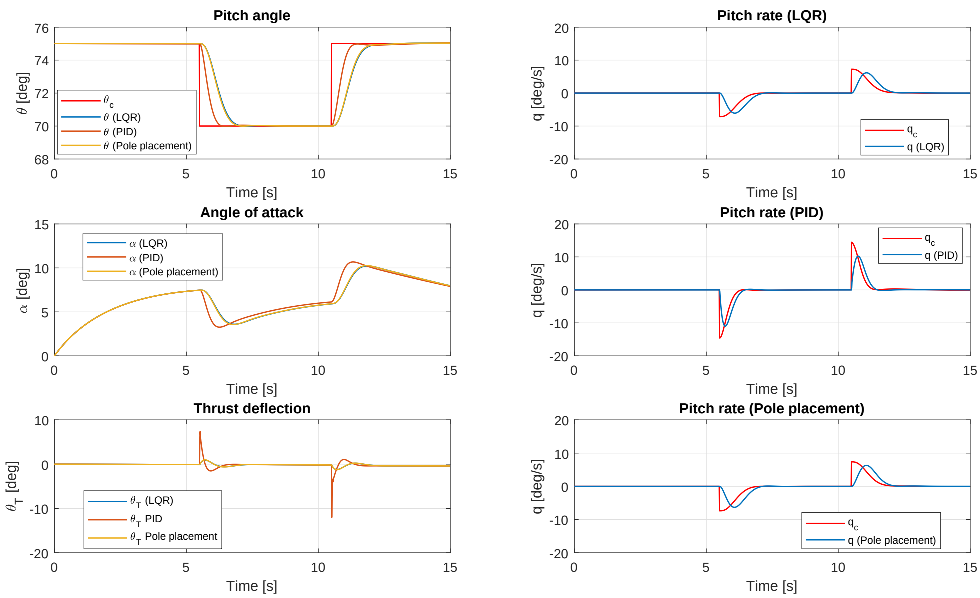

Figure 6.7: Flight Mode 2, pitch axis autopilot performance in the nonlinear 6 DOF model

6.4.1.2 Flight Mode 3

Pitch rate, normal acceleration, altitude rate and altitude autopilot design steps are explained for the following flight condition: {Mach = 0.6, α = 8°, β = 0°, h = 500 m}. With the aerodynamic data of the given flight condition, open loop transfer function which relates the elevator deflection command and pitch rate is found as:

$$\frac{q(s)}{\delta_{ec}(s)} = \frac{3.86 \times 10^4 s^2 + 1.646 \times 10^4 s}{s^5 + 220.4 s^4 + 2.479 \times 10^4 s^3 + 1.305 \times 10^4 s^2 + 3.784 \times 10^4 s} \tag{6.54}$$

Using the same approach that of Flight Mode 2 pitch rate autopilot design, PID gains are found as;

$$K_p = 5.0547 \quad K_i = 10.0463 \quad K_d = 0.0824 \tag{6.55}$$

LQR design parameter q_1 and resulting gain matrix $\boldsymbol{K}$ are found as;

$$q_1 = 359.5587 \quad \boldsymbol{K} = [-1.0128, 4.9582, 0.0673, 0.0003, -18.9620] \tag{6.56}$$

For the pole placement method, desired closed-loop pole locations and the resulting gain matrix are determined as:

$$\begin{aligned} p_1 &= -0.4265 \\ p_{2,3} &= -109.96 \pm j112.18 \\ p_{4,5} &= -3.5563 \pm 4.8522i \\ \boldsymbol{K} &= [-1.0381, 4.7414, 0.0640, 0.0003, -23.1349] \end{aligned} \tag{6.57}$$

As different from the second flight mode's pitch axis autopilots, normal acceleration is controlled in the 1st outer loop of third flight mode pitch axis autopilot system. Pitch rate and normal acceleration can be related with the following transfer function:

$$\frac{A_z(s)}{q(s)} = V\left(\frac{Z_{\delta_e} s^2 + (Z_q M_{\delta_e} - M_q Z_{\delta_e})s + Z_\alpha M_{\delta_e} - M_\alpha Z_{\delta_e}}{M_{\delta_e} s + M_\alpha Z_{\delta_e} - Z_\alpha M_{\delta_e}}\right) \tag{6.58}$$

Using this relationship, normal acceleration open loop transfer functions are obtained for PID, LQR, and pole-placement based options. Since the number of integrators in the normal acceleration open loop transfer function is 0, a type 1 closed-loop system can be obtained using the PI controller to complete outer normal acceleration loop, then the steady state error to a unit step input will be zero for normal acceleration control system. For PID, LQR and pole-placement based inner pitch rate loops, normal acceleration controller proportional-integral gains are found as:

$$\begin{aligned} K_{p,PID} &= -0.0019 \quad K_{p,LQR} = -0.0056 \quad K_{p,pole-placement} = -0.0045 \\ K_{i,PID} &= -0.0053 \quad K_{i,LQR} = -0.0024 \quad K_{i,pole-placement} = -0.0019 \end{aligned} \tag{6.59}$$

Following the same approach to get zero steady-state error and considering the system types, 2nd and 3rd level outer loops of altitude rate and altitude can be controlled using proportional control. According to the design specifications, proportional gains for altitude rate and altitude control loops are found as:

$$\begin{aligned} &\text{Altitude rate loop :} \\ &K_{p,PID} = 0.2595 \quad K_{p,LQR} = 0.2542 \quad K_{p,pole-placement} = 0.2055 \\ &\text{Altitude loop :} \\ &K_{p,PID} = 0.0862 \quad K_{p,LQR} = 0.0993 \quad K_{p,pole-placement} = 0.0797 \end{aligned} \tag{6.60}$$

Then, altitude control loop is completed. In Figure 6.8, linear closed-loop system altitude, altitude rate, normal acceleration and pitch rate step responses are given. In Table 6.5 controller gains and time and frequency domain results are given. Design results show that the design specifications are satisfied. To test the performance of pitch axis autopilots of Flight Mode 3, which are designed at different flight conditions, the 6 DOF nonlinear simulation environment is used. Simulation results for a case in which an altitude profile, which has a step change, is tracked are given in Figure 6.9. Nonlinear simulation results show that the autopilot performance is adequate.

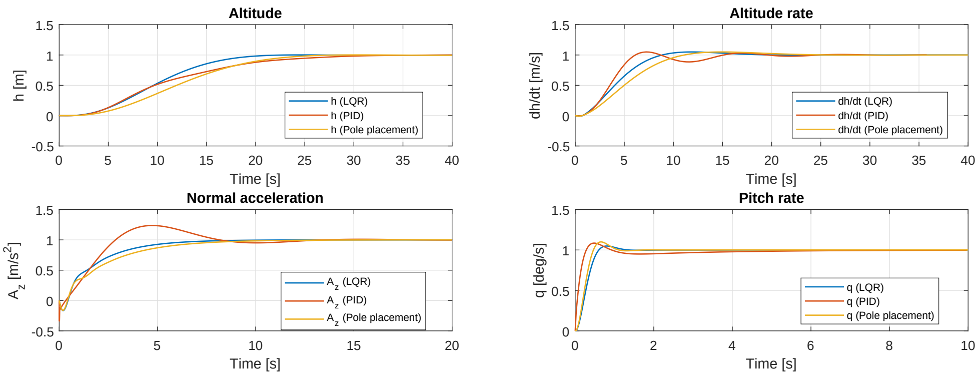

Figure 6.8: Flight Mode 3, linear pitch axis closed-loop system step responses

6.4.2 Roll Axis Autopilots

6.4.2.1 Flight Mode 2

In Figure 6.10, roll angle and roll rate responses of the linear closed-loop system designed at the flight point of {Mach = 0.3, α = 6°, β = 0°, h = 500 m} are given. In Table 6.6 controller gains and time and frequency domain results are provided. The performance of roll axis autopilots, which are designed for different flight conditions, are tested in the 6 DOF nonlinear simulation environment. Simulation results are given in Figure 6.11. Design results show that the desired control specifications are achieved and a satisfactory control performance is obtained in nonlinear simulations.

6.4.2.2 Flight Mode 3

In Figure 6.12, roll angle and roll rate responses of the linear closed-loop system designed at the flight point of {Mach = 0.6, α = 4°, β = 0°, h = 500 m} are given. In Table 6.7 controller gains and time and frequency domain results are provided. The performance of roll axis autopilots, while the missile is turning at a constant altitude and with a constant speed, are tested in the 6 DOF nonlinear simulation environment. Simulation results are given in Figure 6.13. Results show that the design specifications are achieved and the autopilot performance in nonlinear simulation is satisfactory.

Option 1 (PID)	Option 2 (LQR)	Option 3 (Pole placement)
Pitch rate loop		
K_p = 5.0547, K_i = 10.0463 K_d = 0.0824	$\boldsymbol{K}$ = [-1.0128, 4.9582, 0.0673, 0.0003, -18.9620]	$\boldsymbol{K}$ = [-1.0381, 4.7414, 0.0640 0.0003, -23.1349]
$T_s(s)$ = 0.6986 $T_r(s)$ = 0.2127 $OS(\%)$ = 8.4806	$T_s(s)$ = 0.5345 $T_r(s)$ = 0.4867 $OS(\%)$ = 4.8996	$T_s(s)$ = 0.8811 $T_r(s)$ = 0.3963 $OS(\%)$ = 9.9861
$GM(dB) = \infty$ $PM(°)$ = 80.1944 $\omega_{gc}(rad/s)$ = 8.1417 $\omega_{n,pitch}(rad/s)$ = 1.2383	$GM(dB) = \infty$ $PM(°)$ = 66.1359 $\omega_{gc}(rad/s)$ = 8.3300 $\omega_{n,pitch}(rad/s)$ = 1.2383	$GM(dB) = \infty$ $PM(°)$ = 60.0021 $\omega_{gc}(rad/s)$ = 8.3358 $\omega_{n,pitch}(rad/s)$ = 1.2383
Normal acceleration loop		
K_p = -0.0019, K_i = -0.0053	K_p = -0.0056, K_i = -0.0024	K_p = -0.0045, K_i = -0.0019
$T_s(s)$ = 7.2261 $T_r(s)$ = 2.5324 $OS(\%)$ = 23.6746	$T_s(s)$ = 5.4625 $T_r(s)$ = 4.4473 $OS(\%)$ = 0	$T_s(s)$ = 6.9593 $T_r(s)$ = 5.6490 $OS(\%)$ = 0
$GM(dB)$ = 10.0001 $PM(°)$ = 45.0002	$GM(dB)$ = 10.0198 $PM(°)$ = 82.5359	$GM(dB)$ = 10.0079 $PM(°)$ = 85.3048
Altitude rate loop		
K_p = 0.2595	K_p = 0.2542	K_p = 0.2055
$T_s(s)$ = 13.8417 $T_r(s)$ = 5.3441 $OS(\%)$ = 5.0000	$T_s(s)$ = 7.8627 $T_r(s)$ = 7.1772 $OS(\%)$ = 5.0000	$T_s(s)$ = 9.8584 $T_r(s)$ = 8.9880 $OS(\%)$ = 5.0000
$GM(dB)$ = 8.6394 $PM(°)$ = 70.3566	$GM(dB)$ = 22.7751 $PM(°)$ = 63.5238	$GM(dB)$ = 26.8477 $PM(°)$ = 63.9342
Altitude loop		
K_p = 0.0862	K_p = 0.0993	K_p = 0.0797
$T_s(s)$ = 25.4205 $T_r(s)$ = 21.1031 $OS(\%)$ = 0.1000	$T_s(s)$ = 17.9587 $T_r(s)$ = 16.1473 $OS(\%)$ = 0.1001	$T_s(s)$ = 22.4097 $T_r(s)$ = 20.1484 $OS(\%)$ = 0.1002
$GM(dB)$ = 15.2734 $PM(°)$ = 71.8691	$GM(dB)$ = 13.2822 $PM(°)$ = 67.0564	$GM(dB)$ = 13.5163 $PM(°)$ = 67.1844

Table 6.5: Flight Mode 3, linear pitch axis autopilot design results

6.4.3 Yaw Axis Autopilots

6.4.3.1 Flight Mode 3

In Figure 6.14, lateral acceleration and yaw rate responses of the linear closed-loop system designed at the flight point of {Mach = 0.6, α = 4°, β = 0°, h = 500 m} are given. In Table 6.8 controller gains and time and frequency domain results are

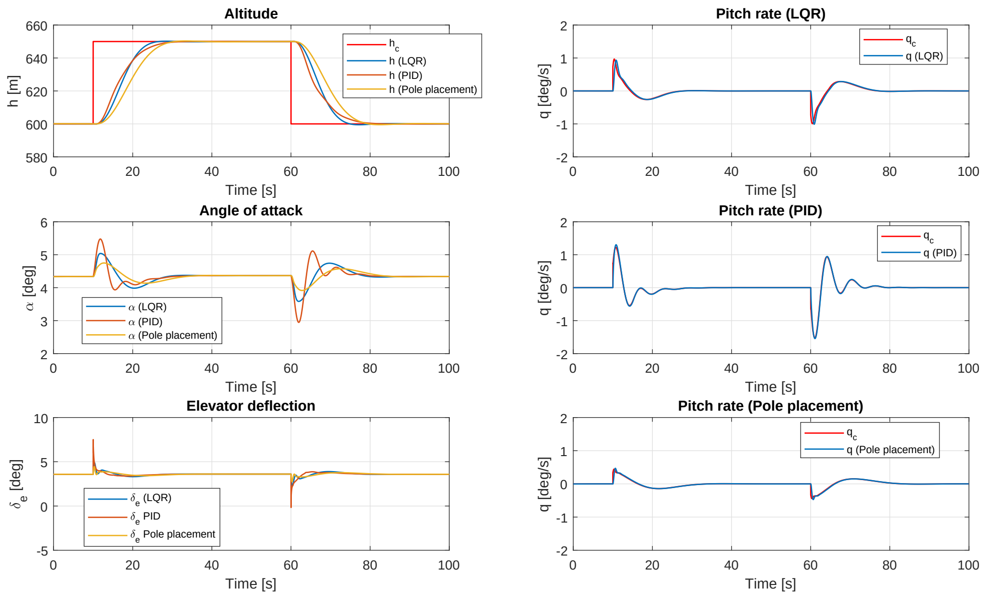

(a) Altitude, angle of attack, elevator deflection and pitch rate results

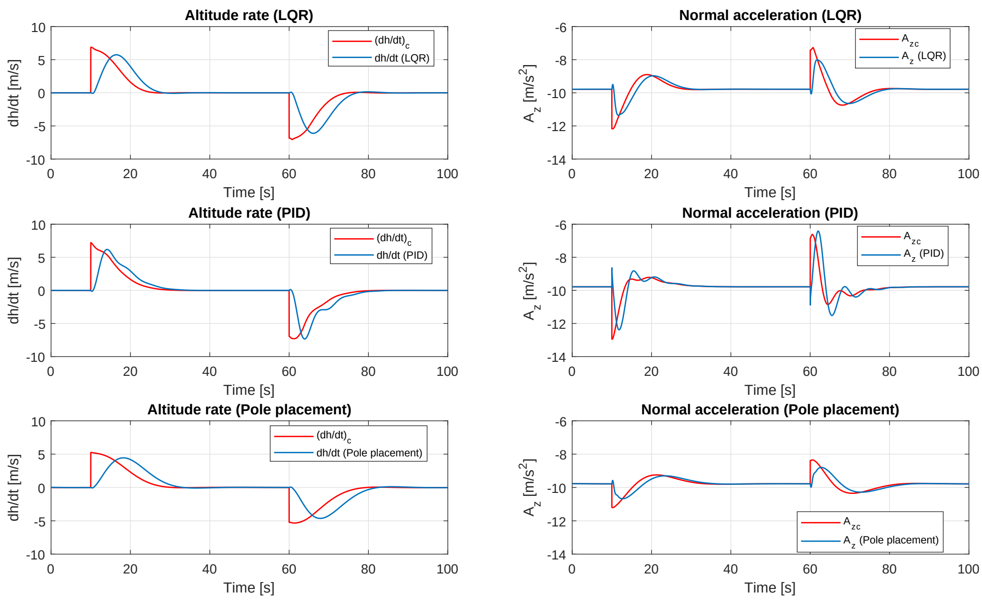

(b) Altitude rate and normal acceleration results

Figure 6.9: Flight Mode 3, pitch axis autopilot performance in the nonlinear 6 DOF model

provided. The performance of yaw axis autopilots, while the missile is turning at a constant altitude and with a constant speed, are tested in the 6 DOF nonlinear simulation environment. Simulation results are given in Figure 6.15. Results show that the design specifications are achieved and the autopilot performance in the nonlinear

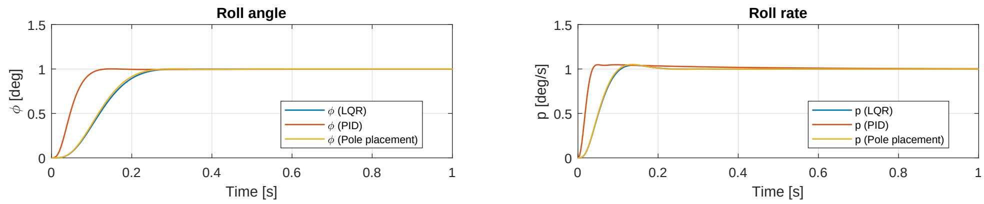

Figure 6.10: Flight Mode 2, linear roll axis closed-loop system step responses

Option 1 (PID)	Option 2 (LQR)	Option 3 (Pole placement)
	Roll rate loop	
K_p = 1.8800 , K_i = 5.8314 K_d = 0.0040	$\boldsymbol{K}$ = [0.0558, 2.0835, 0.4719 0.0019, -41.4235]	$\boldsymbol{K}$ = [0.0431, 2.0639, 0.4671 0.0019, -42.1793]
$T_s(s)$ = 0.0328 $T_r(s)$ = 0.0301 $OS(\%)$ = 4.7867	$T_s(s)$ = 0.0951 $T_r(s)$ = 0.0870 $OS(\%)$ = 4.3363	$T_s(s)$ = 0.1390 $T_r(s)$ = 0.0848 $OS(\%)$ = 5.0426
$GM(dB)$ = 17.7722 $PM(°)$ = 65.5944 $\omega_{gc}(rad/s)$ = 52.2246 $\omega_{n,roll}(rad/s)$ = 0.4350	$GM(dB) = \infty$ $PM(°)$ = 65.5468 $\omega_{gc}(rad/s)$ = 52.6272 $\omega_{n,roll}(rad/s)$ = 0.4350	$GM(dB) = \infty$ $PM(°)$ = 64.6838 $\omega_{gc}(rad/s)$ = 52.2025 $\omega_{n,roll}(rad/s)$ = 0.4350
	Roll angle loop	
K_p = 19.0600	K_p = 7.9300	K_p = 8.1700
$T_s(s)$ = 0.0981 $T_r(s)$ = 0.0856 $OS(\%)$ = 0.0996	$T_s(s)$ = 0.2263 $T_r(s)$ = 0.2024 $OS(\%)$ = 0.0878	$T_s(s)$ = 0.2170 $T_r(s)$ = 0.1948 $OS(\%)$ = 0.0966
$GM(dB)$ = 15.0141 $PM(°)$ = 68.1219	$GM(dB)$ = 12.7533 $PM(°)$ = 66.7331	$GM(dB)$ = 12.3985 $PM(°)$ = 66.5666

Table 6.6: Flight Mode 2, linear roll axis autopilot design results

simulation is satisfactory.

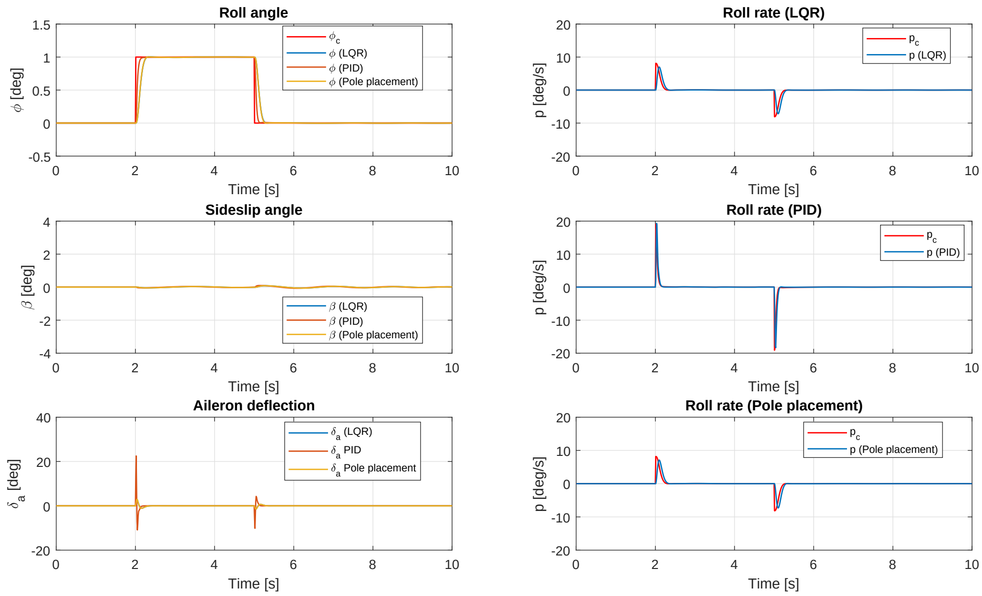

Figure 6.11: Flight Mode 2, roll axis autopilot performance in the nonlinear 6 DOF model

Option 1 (PID)	Option 2 (LQR)	Option 3 (Pole placement)
Roll rate loop		
K_p = 0.4367 , K_i = 3.3400 K_d = 0.0005	$\boldsymbol{K}$ = [0.0204, 0.4653, 0.4531, 0.0019, -11.1746]	$\boldsymbol{K}$ = [-0.0692, 0.4570, 0.4330, 0.0017, -13.8375]
$T_s(s) = 0.0334$ $T_r(s) = 0.0309$ $OS(\%) = 5.0000$	$T_s(s) = 0.0898$ $T_r(s) = 0.0821$ $OS(\%) = 4.1316$	$T_s(s) = 0.1385$ $T_r(s) = 0.0664$ $OS(\%) = 10.1083$
$GM(dB) = 15.0474$ $PM(°) = 64.0748$ $\omega_{gc}(rad/s) = 51.6555$ $\omega_{n,roll}(rad/s) = 5.7000$	$GM(dB) = \infty$ $PM(°) = 67.3855$ $\omega_{gc}(rad/s) = 52.3598$ $\omega_{n,roll}(rad/s) = 5.7000$	$GM(dB) = \infty$ $PM(°) = 59.5978$ $\omega_{gc}(rad/s) = 52.3338$ $\omega_{n,roll}(rad/s) = 5.7000$
Roll angle loop		
$K_p = 20.3700$	$K_p = 8.3800$	$K_p = 10.3400$
$T_s(s) = 0.0903$ $T_r(s) = 0.0794$ $OS(\%) = 0.0989$	$T_s(s) = 0.2148$ $T_r(s) = 0.1918$ $OS(\%) = 0.0907$	$T_s(s) = 0.1605$ $T_r(s) = 0.1465$ $OS(\%) = 0.0874$
$GM(dB) = 13.4773$ $PM(°) = 67.2178$	$GM(dB) = 12.7646$ $PM(°) = 66.7390$	$GM(dB) = 10.5250$ $PM(°) = 66.3976$

Table 6.7: Flight Mode 3, linear roll axis autopilot design results

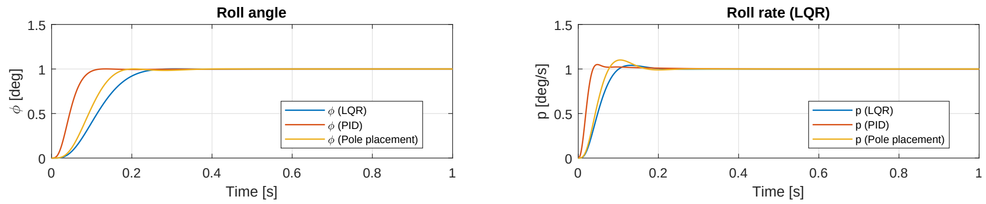

Figure 6.12: Flight Mode 3, linear roll axis closed-loop system step responses

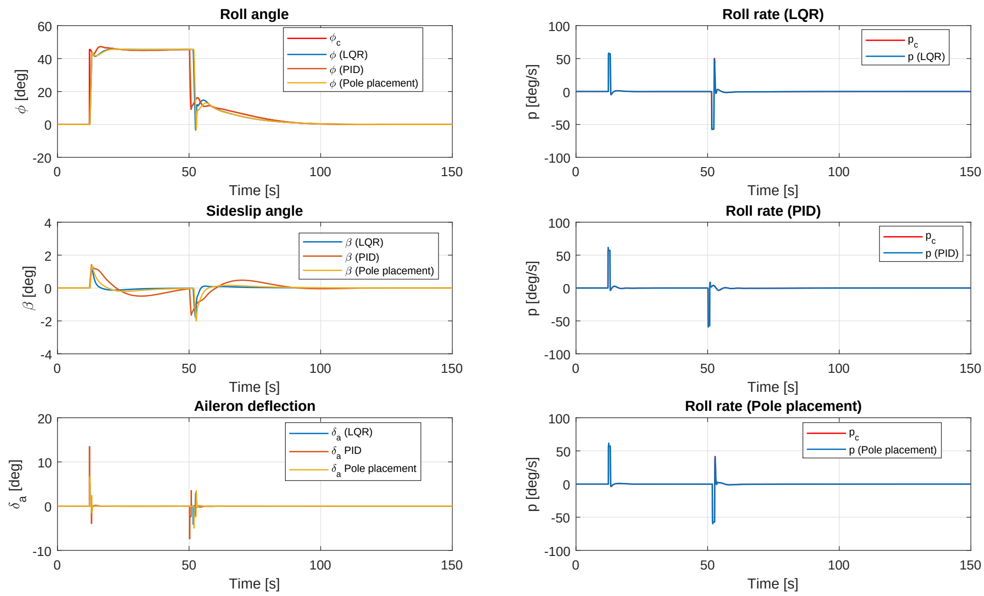

Figure 6.13: Flight Mode 3, roll axis autopilot performance in the nonlinear 6 DOF model

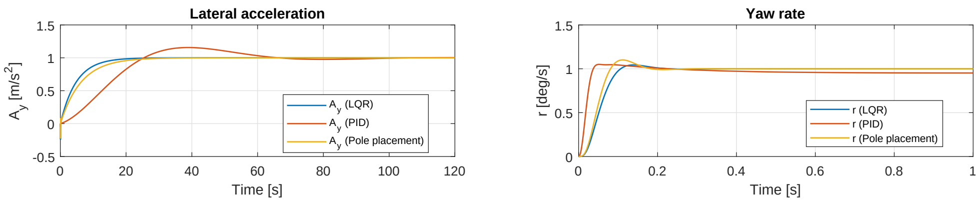

Figure 6.14: Flight Mode 3, linear yaw axis closed-loop system step responses

Option 1 (PID)	Option 2 (LQR)	Option 3 (Pole placement)
Yaw rate loop		
$K_p = 3.0368$, $K_i = 12.3327$ $K_d = 0.0068$	$\boldsymbol{K}$ = [0.9223, 3.3995, 0.4665, 0.0019, -68.1573]	$\boldsymbol{K}$ = [0.9895, 3.3782, 0.4530 0.0018, -85.1972]
$T_s(s) = 22.0413$ $T_r(s) = 0.0305$ $OS(\%) = 5.0000$	$T_s(s) = 0.0950$ $T_r(s) = 0.0869$ $OS(\%) = 4.3670$	$T_s(s) = 0.1475$ $T_r(s) = 0.0704$ $OS(\%) = 10.0953$
$GM(dB) = 18.2102$ $PM(^\circ) = 65.3495$ $\omega_{gc}(rad/s) = 51.3185$ $\omega_{n,yaw}(rad/s) = 3.3943$	$GM(dB) = \infty$ $PM(^\circ) = 65.6949$ $\omega_{gc}(rad/s) = 52.3410$ $\omega_{n,yaw}(rad/s) = 3.3943$	$GM(dB) = \infty$ $PM(^\circ) = 58.9202$ $\omega_{gc}(rad/s) = 52.3363$ $\omega_{n,yaw}(rad/s) = 3.3943$
Lateral acceleration loop		
$K_p = 0.0010$, $K_i = 0.0005$	$K_p = 0.0127$, $K_i = 0.0010$	$K_p = 0.0097$, $K_i = 0.0008$
$T_s(s) = 57.0405$ $T_r(s) = 22.0400$ $OS(\%) = 15.6354$	$T_s(s) = 13.4083$ $T_r(s) = 11.1033$ $OS(\%) = 0$	$T_s(s) = 17.7084$ $T_r(s) = 14.5826$ $OS(\%) = 0$
$GM(dB) = 23.5789$ $PM(^\circ) = 53.5540$	$GM(dB) = 10.0138$ $PM(^\circ) = 89.4076$	$GM(dB) = 10.0022$ $PM(^\circ) = 89.6414$

Table 6.8: Flight Mode 3, linear yaw axis autopilot design results

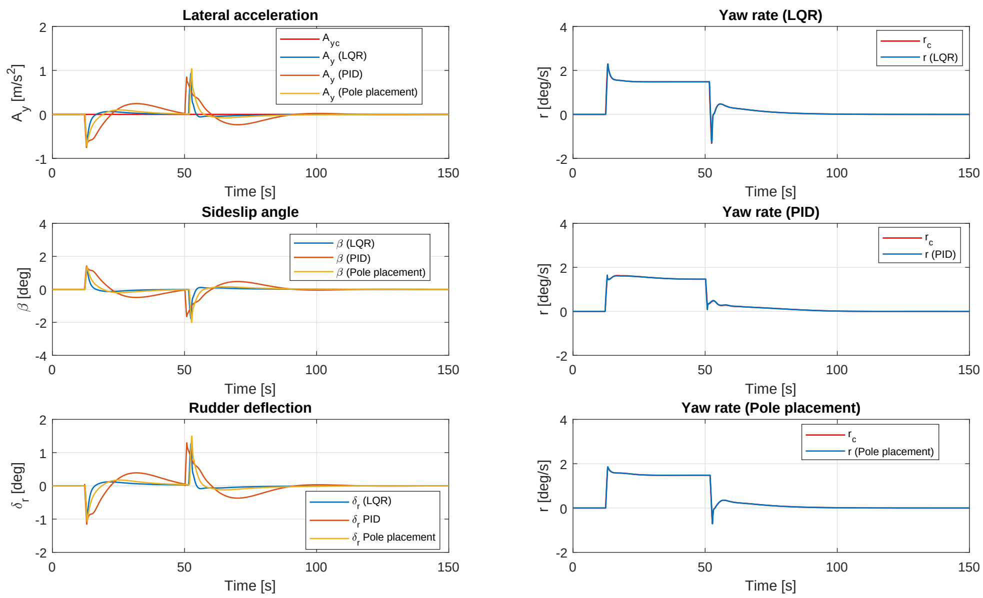

Figure 6.15: Flight Mode 3, yaw axis autopilot performance in the nonlinear 6 DOF model

6.5 Performance Comparisons and Autopilot Selection

Having designed the three different autopilot options and tested them in the 6 DOF nonlinear simulation model, by using nonlinear simulation results, the performance of the options can be compared in terms of several important criteria which are selected by the designer. Then, the best option can be determined considering the overall performance on these criteria. In this study, autopilot options are compared with respect to the

- integral of the absolute tracking error,
- maximum absolute control effort,
- deviations from the trim angle of attack for level flight,
- deviations from the zero sideslip angle.

While the first and second criteria are applied for all autopilots of Mode 2 and Mode 3, third criteria is only applied for altitude autopilot of Mode 3 and fourth criteria is only applied for lateral acceleration autopilot of Mode 3.

In Table 6.9, the scores of each autopilot option for the related performance criteria are given. Scores of each autopilot category are scaled such that the worst option's score is normalized to 1.

Performance scores show that different autopilot options can be suitable concerning different performance criteria. For example, while Option 1 generally has the worst performance in terms of maximum absolute control effort, its tracking performance is generally better than the other options. Thus, in order to conclude with an "overall best option", each performance criterion can be weighed, and a total score of each option can be calculated for each autopilot category. This total score can be defined as:

$$S_{total} = \sum_{i=1}^{n} w_i s_i \tag{6.61}$$

Integral absolute error scores			
Autopilot category	Option 1 (PID)	Option 2 (LQR)	Option 3 (Pole placement)
Roll angle autopilot (Mode 2)	0.4084	1.0000	0.9887
Pitch angle autopilot (Mode 2)	0.5176	1.0000	0.9747
Roll angle autopilot (Mode 3)	0.1446	0.9531	1.0000
Altitude autopilot (Mode 3)	0.7483	0.7758	1.0000
Normal acceleration autopilot (Mode 3)	0.7248	0.5953	1.0000
Lateral acceleration autopilot (Mode 3)	1.0000	0.2446	0.4286
Maximum absolute control efffort scores			
Autopilot category	Option 1 (PID)	Option 2 (LQR)	Option 3 (Pole placement)
Roll angle autopilot (Mode 2)	1.0000	0.1304	0.1326
Pitch angle autopilot (Mode 2)	1.0000	0.1013	0.1046
Roll angle autopilot (Mode 3)	1.0000	0.3853	0.4919
Altitude autopilot (Mode 3)	1.0000	0.6516	0.5922
Normal acceleration autopilot (Mode 3)	1.0000	0.6516	0.5922
Lateral acceleration autopilot (Mode 3)	0.8640	0.8481	1.0000
"α deviation from trim for level flight" scores			
Autopilot category	Option 1 (PID)	Option 2 (LQR)	Option 3 (Pole placement)
Altitude autopilot (Mode 3)	1.0000	0.9229	0.7054
"β deviation from zero" scores			
Autopilot category	Option 1 (PID)	Option 2 (LQR)	Option 3 (Pole placement)
Lateral acceleration autopilot (Mode 3)	1.0000	0.2422	0.4269

Table 6.9: Separate performance criterion scores of each autopilot option

where n is the number of performance criteria, w_i's are criteria weighting factors and s_i's are the scores for each criteria. Integral absolute error, maximum absolute control effort, α deviation and β deviation scores are assigned as s_1, s_2, s_3 and s_4, respectively. Then, the weightings of each autopilot are chosen as:

- Pitch angle and roll angle autopilots: $w_1 = 0.75$, $w_2 = 0.25$
- Altitude autopilot $w_1 = 0.6$, $w_2 = 0.2$, $w_3 = 0.2$
- Normal acceleration autopilot: $w_1 = 0.75$, $w_2 = 0.25$
- Lateral acceleration autopilot $w_1 = 0.6$, $w_2 = 0.2$, $w_4 = 0.2$.

With these weightings, total scores are calculated as in Table 6.10. The total scores show that, for roll and pitch angle autopilots, Option 1 is the best option, and for altitude, normal and lateral acceleration autopilots, Option 2 provides the best results.

Total scores			
Autopilot category	Option 1 (PID)	Option 2 (LQR)	Option 3 (Pole placement)
Roll angle autopilot (Mode 2)	0.5563	0.7826	0.7747
Pitch angle autopilot (Mode 2)	0.6382	0.7753	0.7572
Roll angle autopilot (Mode 3)	0.3584	0.8112	0.8730
Altitude autopilot (Mode 3)	0.8490	0.7804	0.8595
Normal acceleration autopilot (Mode 3)	0.7936	0.6093	0.8981
Lateral acceleration autopilot (Mode 3)	0.9728	0.3648	0.5426

Table 6.10: Total performance scores of each autopilot option

6.6 Digital Implementation

In the previous sections, autopilot design studies are conducted and the designed autopilots are implemented in the continuous time domain. However, in today's practical systems, controllers are generally implemented by using digital control systems, since they can be advantageous over analog control systems in terms of a lot of measures such as cost, performance, power consumption, accuracy, reliability, and easiness of implementation [48]. For the missile system considered in this work, the digital control system can be represented as in Figure 6.16.

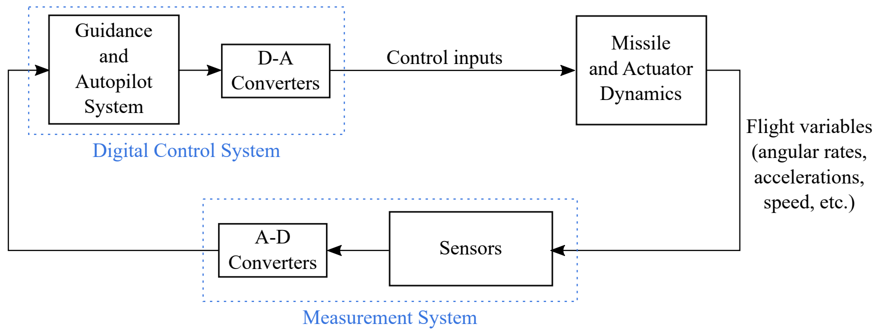

Figure 6.16: Digital control system representation for the missile

In this representation, flight variables such as angular rates, accelerations, speed, etc. are measured and provided to the digital control system by the measurement system. Outputs of the measurement system can be considered as the sampled and quantized versions of the continuous time flight variables. This sampling and quantization processes are done by analog-to-digital (A-D) converters. Thus, the guidance and autopilot system deals with discrete-time signals. The digital control system provides analog control inputs to the missile and actuator dynamics, by utilizing digital-to-analog (D-A) converters. When the controller design procedure is done in a way that the design specifications are met with continuous time controllers and if they will be implemented in digital systems, the performance of the control system should also be tested for the digitally implemented version of the system. A way of doing this is using discrete measurement and control models in the simulations or performing real-time hardware-in-the-loop simulations.

However, some issues still can be taken into account during the control design procedures in the continuous domain. For example, the performance of the digital controller may get worse as the sampling rate decreases. For this reason, different rules of thumb can be used to choose a proper sampling rate. One of these rules of thumb states that the sampling rate should be larger than 5 times of the closed-loop bandwidth of the considered feedback loop [48]. In other words, it can be concluded that where the sample rate is fixed before the controller design studies, the closed-loop bandwidth of the controller to be designed should be less than one-fifth of the fixed sample rate.

As an example, PID based pitch angle autopilot of Flight Mode 2 is considered to test the discrete time implementation performance with respect to the reference continuous time implementation performance. In the simulation model, pitch angle and pitch rate measurements are sampled with different frequencies and provided to the discrete pitch angle autopilot block. During the discrete implementation, discrete integration and derivation structures are used. Analog control inputs which are fed to the missile and actuator dynamics are generated in zero-order hold sense. Pitch angle tracking performances for different sampling frequencies are shown in Figure 6.17. The tracking performance of the continuous time controller which uses the continuous time measurements is chosen as the desired reference tracking performance.

The results show that the digital controller performance for 100 Hz sampling frequency is very close to that of the continuous time controller performance. However, as the sampling frequency decreases, the difference between the reference tracking and the obtained tracking increases and the digital controller performance degrades. The tracking performance at 5 Hz sampling frequency is significantly different from the desired control performance due to the existence of high overshoot and oscilla-

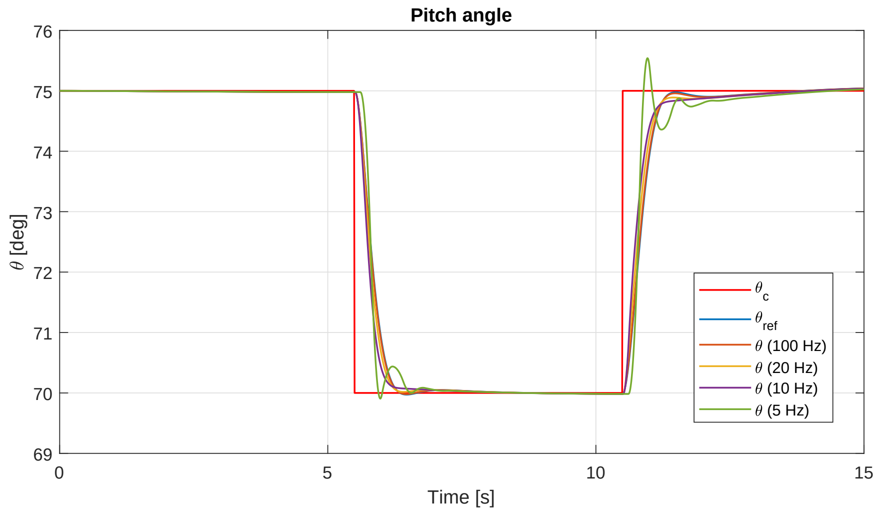

Figure 6.17: Pitch angle control performance for different sampling frequencies

tions. The maximum closed-loop bandwidth, which is seen among the linear PID based pitch angle controllers, is about 1.5 Hz. Thus, according to the given rule of thumb related to the ideal selection of safe sampling rate, the sampling frequency should not be larger than 7.5 Hz and the result obtained for 5 Hz sampling frequency is consistent with this statement.

In the analysis of the designed autopilots for pitch, roll and yaw axes of different flight modes, it is seen that the maximum closed-loop bandwidth is about 17 Hz. Based on the given rule of thumb, since the digital hardware of today is capable of providing a sampling frequency which is much larger than this bandwidth and assuming that the quantization errors are negligible, digital implementation of the autopilots of this study is not a factor which may degrade the desired autopilot performances.

6.7 Simulation of Complete Mission

In this section, two different complete missions which covers the launch, boost, cruise, and terminal phases are simulated in the 6 DOF simulation model.

In the first scenario, the mission starts from underwater launch and ends with a stationary target interception. The control strategy of launch and boost phases are the obtained optimal control strategy for these phases in Chapter 5. The route of the missile in cruise phase consists of 4 waypoints, which are located 25 kilometers away from each other and 400 meters above the 0 meter altitude. After the last waypoint is reached, the terminal phase begins and the missile is guided through the target, which is located at 0 meter altitude and 15 km away from the last waypoint. Through the cruise and terminal phases, the desired total velocity is set to 0.6 Mach.

In the second scenario, the launch and boost phases are simulated as in the first scenario. However, as different from the previous scenario, the route of the missile in cruise phase is more complex and consists of 12 waypoints, which are located with different ranges away from each other. Moreover, the altitude profile to be followed is not constant but changing between the waypoints. Similar to the first scenario, after the last waypoint is reached, the terminal phase begins and the missile is guided through the target, which is located at 0 meters altitude and 15 km away from the last waypoint. Through the cruise and terminal phases, the desired total velocity is set to 0.6 Mach.

Simulation results showing the flight parameters and applied controls for both scenarios are given in the following figures.

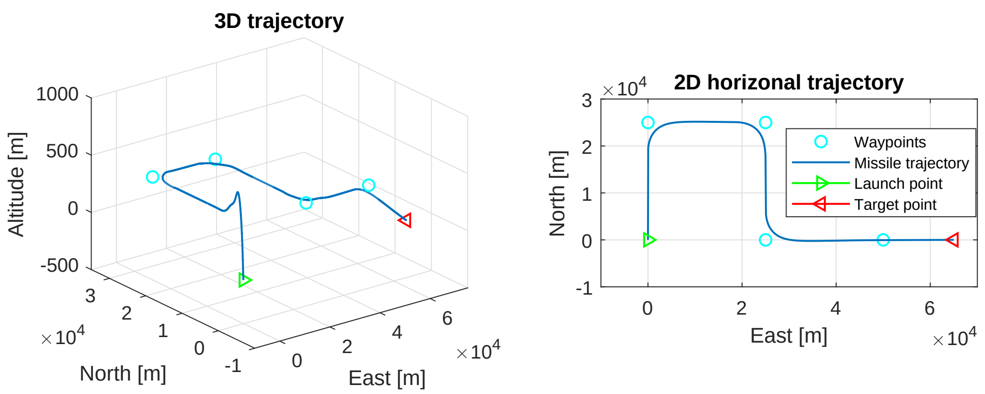

Figure 6.18: Complete Mission 1 simulation results for 3D and 2D horizontal trajectories

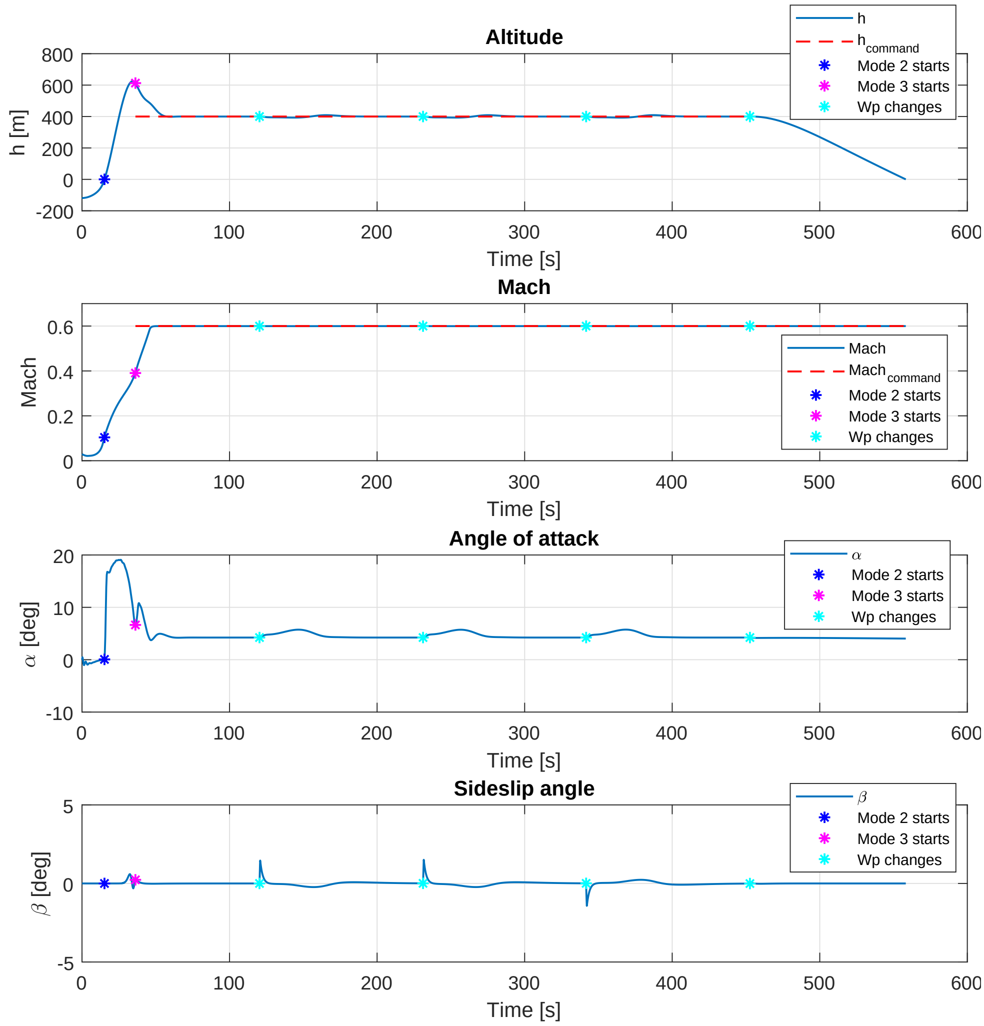

Figure 6.19: Complete Mission 1 simulation results for altitude, Mach, angle of attack and sideslip angle

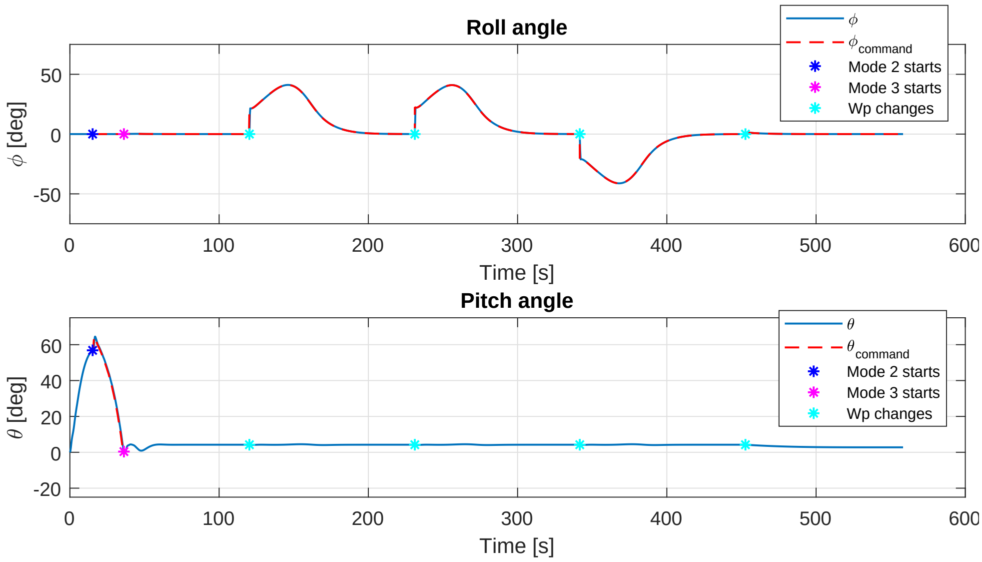

Figure 6.20: Complete Mission 1 simulation results for roll angle and pitch angle

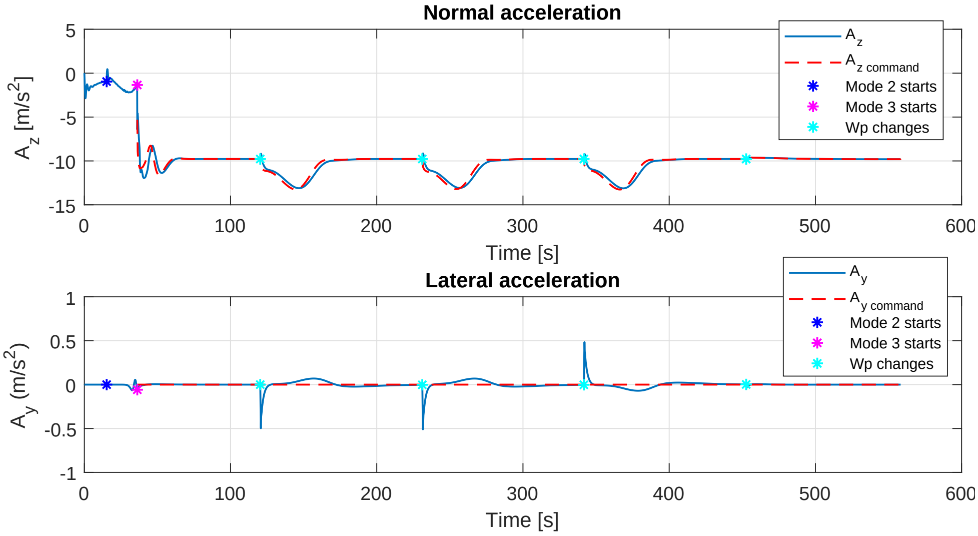

Figure 6.21: Complete Mission 1 simulation results for normal acceleration lateral acceleration

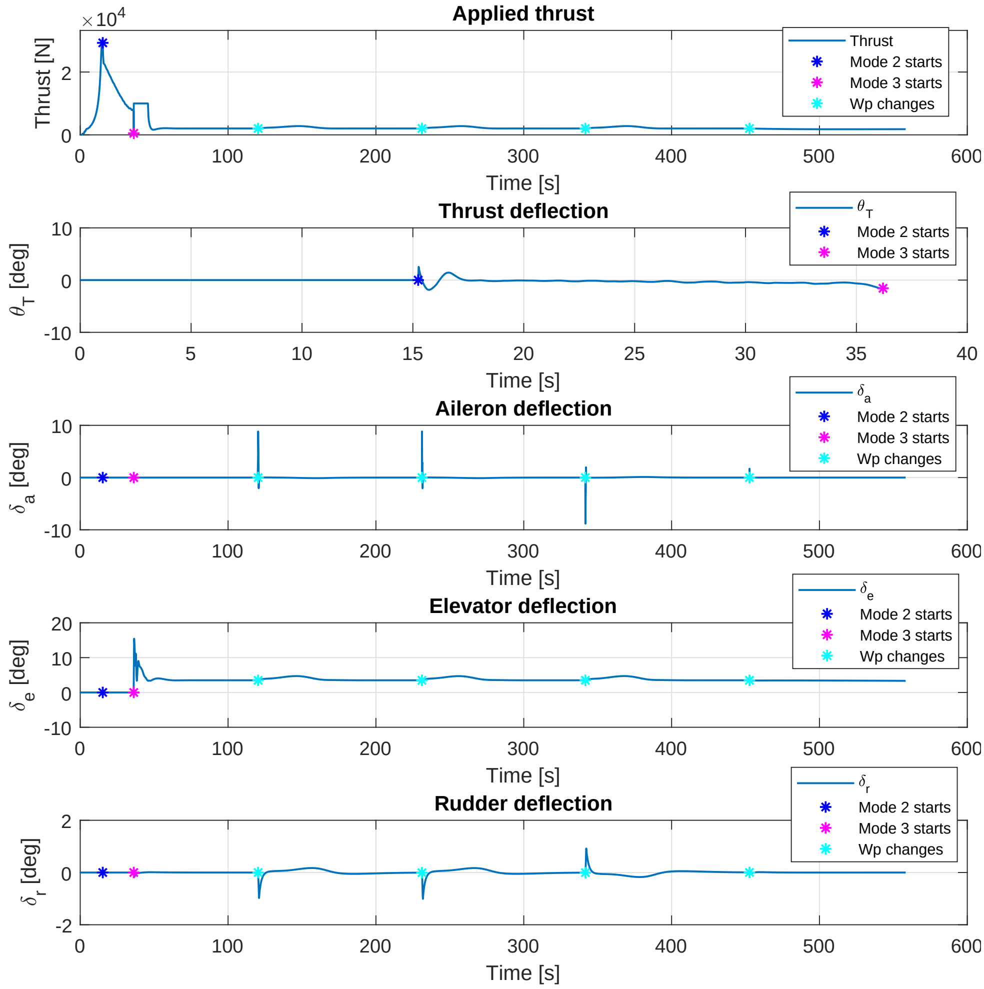

Figure 6.22: Complete Mission 1 simulation results for applied thrust, thrust deflection and control surface deflections

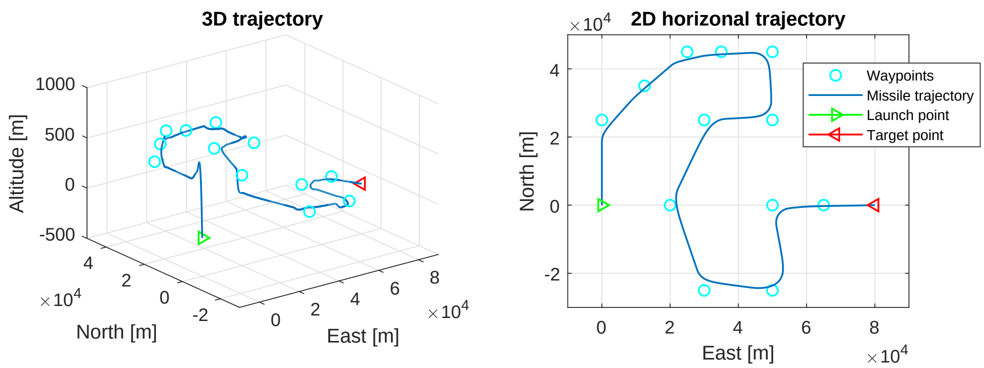

Figure 6.23: Complete Mission 2 simulation results for 3D and 2D horizontal trajectories

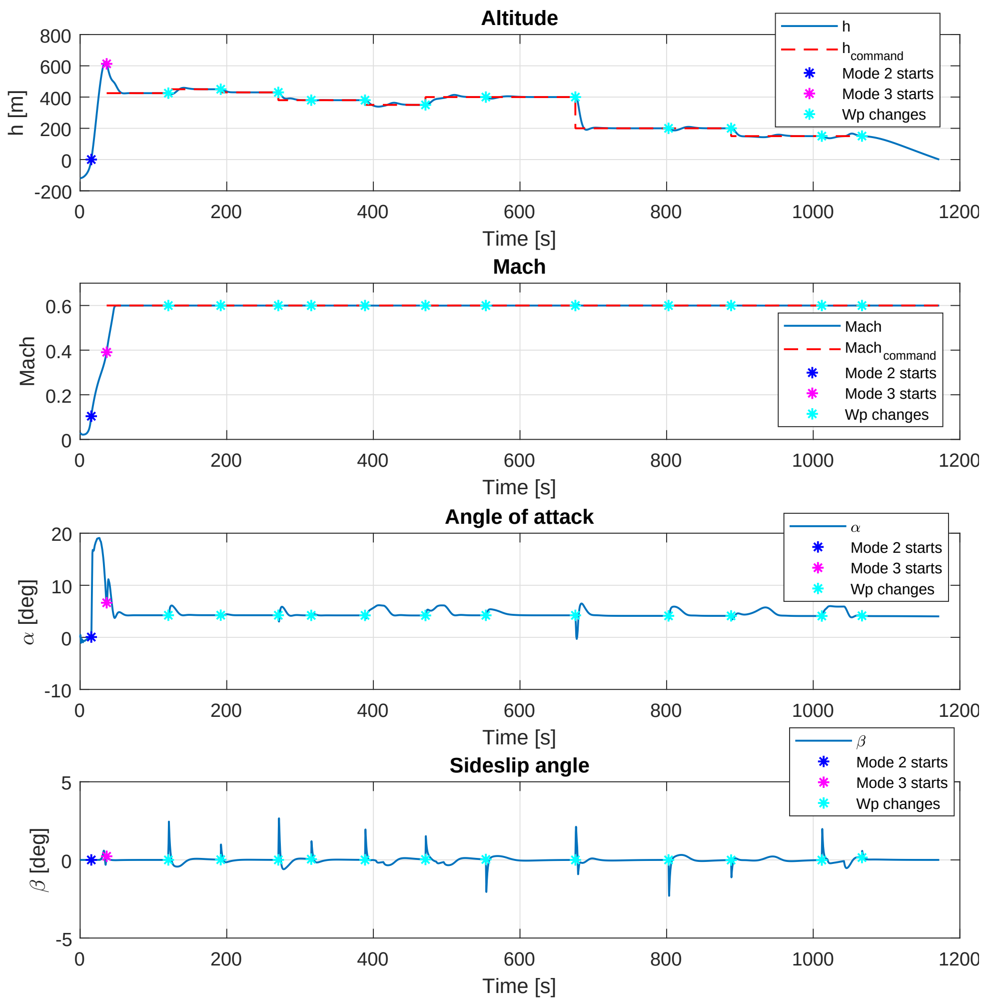

Figure 6.24: Complete Mission 2 simulation results for altitude, Mach, angle of attack and sideslip angle

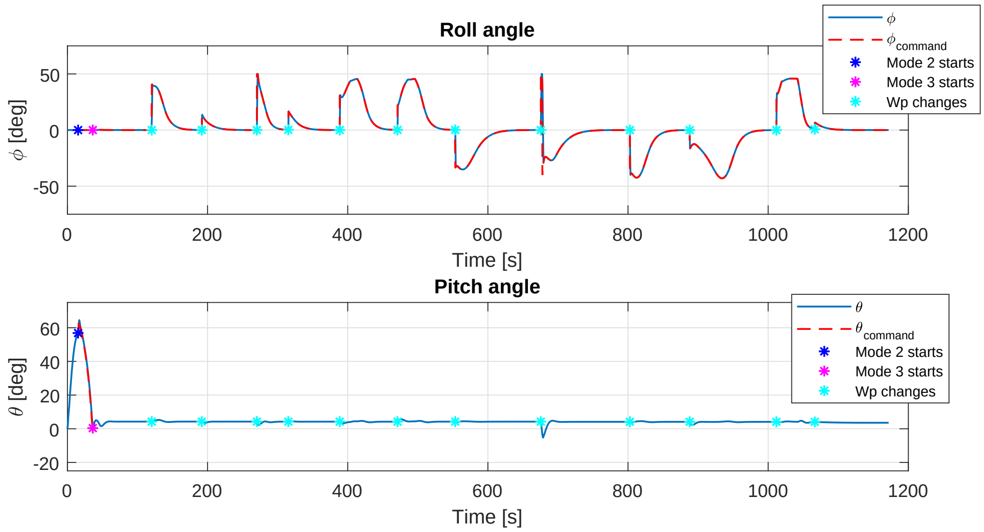

Figure 6.25: Complete Mission 2 simulation results for roll angle and pitch angle

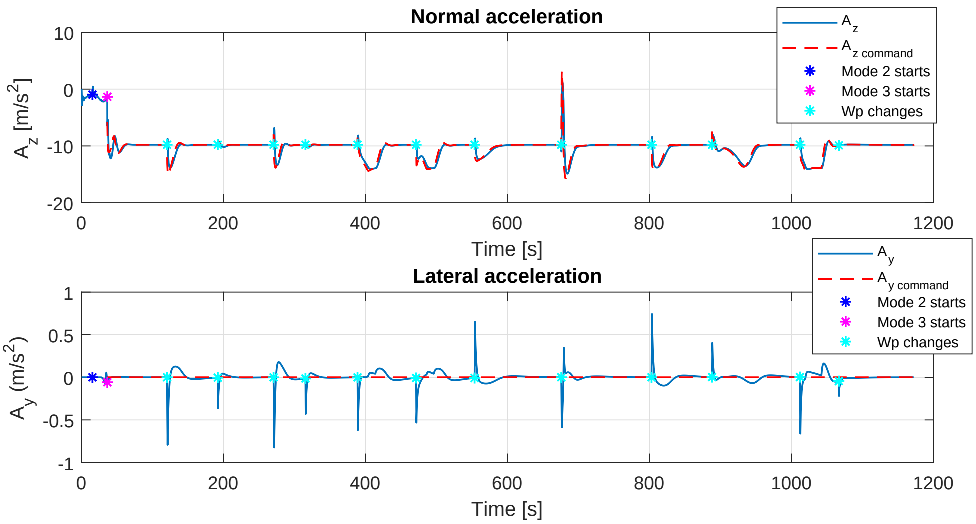

Figure 6.26: Complete Mission 2 simulation results for normal acceleration lateral acceleration

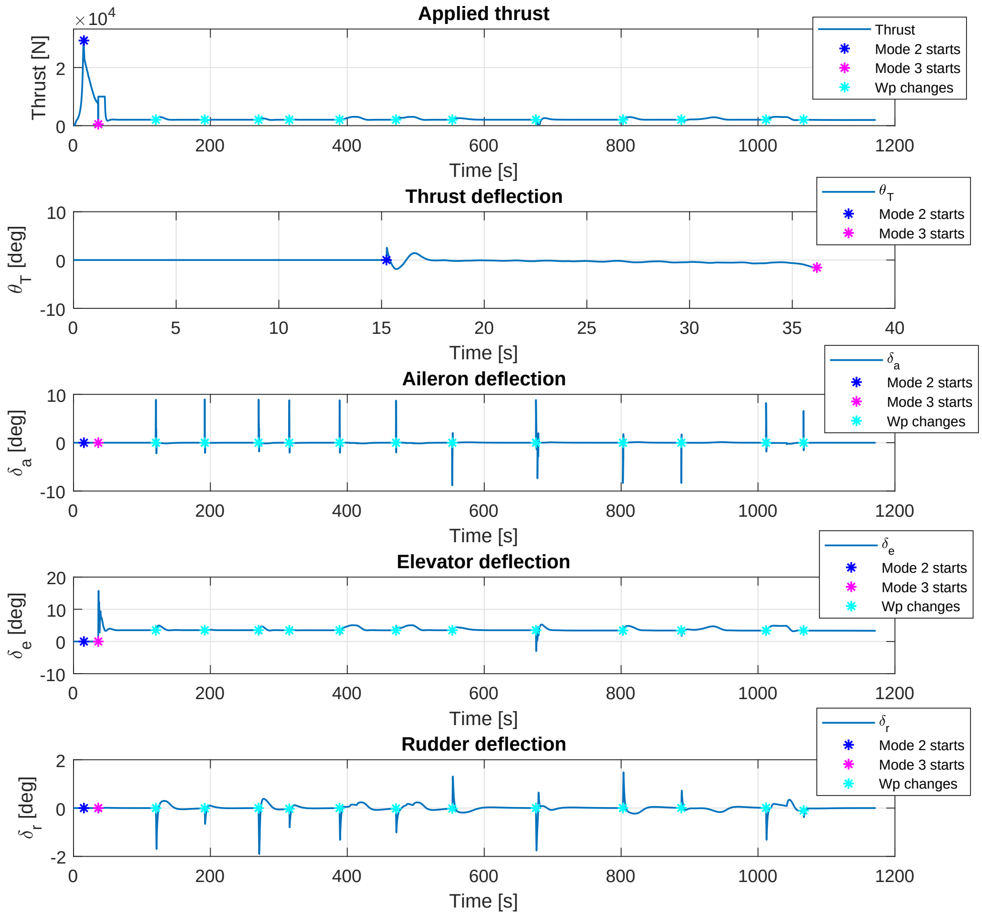

Figure 6.27: Complete Mission 2 simulation results for applied thrust, thrust deflection and control surface deflections

6.8 Conclusion

In this chapter, firstly nonlinear motion equations are linearized and decoupled for roll, pitch and yaw dynamics. After that, three different cascaded autopilot options are developed in which inner angular rate loops are controlled with PID, LQR or pole-placement based autopilots. For each option, attitude angle, normal/lateral acceleration, altitude rate, and altitude variables are controlled in the outer loops by using P or PI based autopilots. Design results are presented for both linear and nonlinear models, and the performance comparisons between three different options are made and the overall best option for each autopilot category is determined. Some practical design considerations related to digital implementation are explained. Having integrated the designed autopilots to the missile model by using gain scheduling, a complete mission from underwater launch to a stationary target interception is simulated in the 6 DOF nonlinear simulation environment, and the results are given. In the results, it is seen that control performances are satisfactory and the results of the other flight parameters are reasonable.

Considering the overall autopilot system design, it is important to explain a design consideration. In this study, a second order standard actuator dynamic model which does not include any control surface deflection/deflection rate limit is used. However, in practice, the existing actuators have control surface deflection and deflection rate limits. Through the investigated nonlinear 6-DOF autopilot test scenarios and complete mission simulations of this study, it is seen that the control surface deflection and deflection rate results are reasonable and the practical actuators can be used in accordance with the designed autopilots. On the other hand, for a real control system design, these deflection and deflection rate limits should be taken into account in the autopilot design specifications and extensive simulations which cover the possible flight scenarios including the extreme cases should be investigated to make sure that the available actuators are suitable for the designed control system.

CHAPTER 7

DISCUSSION AND CONCLUSION

In this thesis, guidance and control problem of a submarine-launched cruise missile is studied. Firstly the conceptual missile and a typical mission profile, which consists of four phases which are the launch, boost, cruise, and terminal phases, are described in detail. Then, the nonlinear 6 DOF motion equations are derived, and hydrodynamic/aerodynamic parameters are retrieved. After that, the guidance and control problem for all phases is focused on.

The guidance and control of the launch and boost phases are examined as a minimum-effort optimal control problem where the aim is to complete these phases for given initial and final conditions while minimizing the energy need, which is represented as a function of the applied thrust in this study. The objective of effective usage of available energy is derived from the desire to achieve a range or increase the existing range of the launch and boost phases. This is a desirable objective because the efficient usage of the available energy and obtaining larger ranges provides the system designer with flexibility to accomplish some system or mission-based constraints such as being in a predefined region of speed-altitude envelope at the end of boost phase to ignite its cruise motor or for the initial success of cruise control. In addition to finding optimal control solutions that satisfy the given control objectives, the effect of initial and final conditions of the launch and boost phases on energy need is investigated, and optimal conditions which minimize the energy need are determined. This investigation is performed as there still are feasible solutions. For the launch phase, which covers the motion from submarine-launch to water-exit, effect of launch depth, final forward velocity, water-exit angle, and final time is investigated. For the horizontal launch scenarios, it is observed that, as the final forward velocity increases, the energy need increases. However, for other conditions, the energy need does not monotonically increase or decrease, and optimal conditions should be searched in the region of interest. For the vertical launch scenarios, as the launch depth increases the energy need increases as it is expected. Considering only the launch phase of horizontal launch, for the fixed final forward velocity of 35 m/s, optimal conditions are found as 45 degrees water-exit angle, 102 meters launch depth and 13.8 seconds completion time. Considering the launch phase of vertical launch, for the fixed final forward velocity of 35 m/s, initial depth of 100 meters, and vertical water-exit, optimal completion time is found as 5 seconds. For the boost phase, which covers the motion from water-exit to the beginning of the cruise, the effect of final altitude, final forward velocity, water-exit angle, and final time is investigated. It is seen that, as the final forward velocity and final altitude increase, the energy need increases, and as the final time increases, the energy need decreases. However, for the water-exit angle, the energy need does not monotonically increase or decrease, and the optimal value should be searched in the region of interest. Considering only the boost phase, for the fixed final forward velocity of 135 m/s, and the final altitude of 600 meters, optimal water-exit angle is found as 65 degrees and optimal completion time is found as 21 seconds. Considering the total energy need of the launch and boost phases together by summing them, the water-exit angle which provides the minimum energy need is found as 55 degrees. Then, for the launch phase, for the fixed final forward velocity of 35 m/s and 55 degrees water-exit angle, 119 meters launch depth and 15.2 seconds completion time are found as the optimal values. For the boost phase, for the fixed final forward velocity of 135 m/s, final altitude of 600 meters and 55 degrees water-exit angle, 21.0 seconds completion time is found as the optimal value. In the results, it is also seen that the optimal horizontal launch strategy needs less energy than that of the optimal vertical launch strategy. Results show that, while some optimal initial and final conditions can be determined according to the system and/or mission constraints, others can be chosen utilizing the minimum-effort optimal control solutions.

In order to control the missile motion in the boost, cruise and terminal phases, different autopilot systems are designed. While in the boost phase the attitude is controlled, during cruise phase maneuver and altitude control is achieved to follow a route that is devised by the waypoints. In the terminal phase, the control system aims to guide the missile through the target by realizing acceleration commands calculated by the guidance system. The autopilots are designed in cascaded architecture, where angular rates are controlled in the inner loop, and angle, acceleration, altitude rate and altitude control are performed in the outer loops. The control of inner angular rate loops are achieved by PID and state-feedback based control methods. For state feedback-controllers, design is both done by LQR based and pole-placement based methods. So, in the overall, three different options are obtained for each autopilot category. The performance of the three options are compared in the nonlinear 6 DOF simulation environment, and it is seen that the results satisfy the autopilot specifications. To figure out the best autopilot option, a total performance score is calculated for each option, based on the results obtained from the nonlinear simulation environment. The total performance scores are calculated by weighing some important performance criteria. These criteria are chosen as integral of the absolute tracking error, maximum absolute control effort, deviations from the trim angle of attack for level flight, and deviations from zero sideslip angle. While the first and second criteria are applied for all autopilots of boost, cruise and terminal phases, third criteria is only applied for altitude autopilot of cruise phase and fourth criteria is only applied for lateral acceleration autopilot of cruise and terminal phases. Results show that, while the tracking performance of PID based option is better than the others in general, LQR based option provide better results in terms of control effort, since its maximum absolute control effort is smaller in general. For angle of attack and sideslip angle deviation criterion, pole placement and LQR based options provide the best scores, respectively. Calculating the total performance scores by weighing the separate performance scores, it is seen that, PID based option is best for pitch and roll angle control, and LQR based option provides the best results for altitude and acceleration autopilots. With these results, it can be concluded that according to the control objectives, different autopilot architectures can be more suitable than the other options and the system designer can choose among the options by comparing them with respect to the different critical performance criteria related to the system.

A possible improvement which can be focused on in the future is related to the booster thrust model. In this study, it is assumed that the desired booster thrust is ideally realized within an upper and lower bound. However, in practice, there are some limitations about the total available thrust, some possible delays during the thrust generation, some characteristic thrust increase or decrease profiles or possible misalignments. These models can be combined with a fuel consumption and dynamically changing mass, inertia, and center of gravity models. Thus, a more realistic design can be achieved.

REFERENCES

[1] G. M. Siouris, *Missile guidance and control systems*. Springer Science & Business Media, 2004.

[2] K. Tsipis, "Cruise missiles," *Scientific American*, vol. 236, no. 2, pp. 20–29, 1977.

[3] T. Takahashi, R. Spall, D. Turner, and M. Birney, "A multi-disciplinary survey of advanced subsonic tactical cruise missile configurations," in *43rd AIAA Aerospace Sciences Meeting and Exhibit*, p. 709, 2005.

[4] W. Locke, "Cruise missile system design," in *16th Annual Meeting and Technical Display*, p. 902, 1981.

[5] B. Kuchta, "Technology advances in cruise missiles," in *16th Annual Meeting and Technical Display*, p. 937, 1981.

[6] J. Krempasky, "Terminal area navigation using a relative gps correction vector scheme," in *Guidance, Navigation, and Control Conference*, p. 3816, 1996.

[7] L. Zhang, C. Wei, L. Jing, and N. Cui, "Fixed-time sliding mode attitude tracking control for a submarine-launched missile with multiple disturbances," *Nonlinear Dynamics*, pp. 1–21, 2018.

[8] R. Lloyd and G. Thorp, "A review of thrust vector control systems for tactical missiles," in *14th Joint Propulsion Conference*, p. 1071, 1978.

[9] S. R. Wassom, L. C. Faupell, and T. Perley, "Integrated aerofin/thrust vector control for tactical missiles," *Journal of Propulsion and Power*, vol. 7, no. 3, pp. 374–381, 1991.

[10] R. Tekin, "Design, modeling, guidance and control of a vertical launch surface to air missile," Master's thesis, Middle East Technical University, 2010.

[11] "Mk-45 vertical launching system vls submarines ssn ssgn." `http://www.seaforces.org/wpnsys/SUBMARINE/Mk-45-vertical-launching-system.htm`. Accessed: 2019-06-24.

[12] J. C. Callahan, "Submarine horizontal launch tactom capsule," Aug. 6 2002. US Patent 6,427,574.

[13] M. Haochun, M. Qinghua, C. Yun, Z. Xiaofeng, and Y. Xianjun, "Guidance and control system design of submarine-to-air missile based on optimal control," in *TENCON 2013-2013 IEEE Region 10 Conference (31194)*, pp. 1–4, IEEE, 2013.

[14] N. Wen, Z. Liu, L. Chang, and Y. Ren, "Time optimal control of mini-submarine missile based on control variable parameterization with enhanced time-scaling method," in *Guidance, Navigation and Control Conference (CGNCC), 2016 IEEE Chinese*, pp. 640–642, IEEE, 2016.

[15] M. Xiao, "Modeling and adaptive sliding mode control of the catastrophic course of a high-speed underwater vehicle," *International Journal of Automation and Computing*, vol. 10, no. 3, pp. 210–216, 2013.

[16] D. Qi, J. Feng, B. Xu, A. Liu, and Y. Li, "Water exit model and takeoff control for a morphing cross-media vehicle," *Journal of the Chinese Institute of Engineers*, vol. 40, no. 2, pp. 110–117, 2017.

[17] J. Yang, J. Feng, Y. Li, A. Liu, J. Hu, and Z. Ma, "Water-exit process modeling and added-mass calculation of the submarine-launched missile," *Polish Maritime Research*, vol. 24, SI, pp. 152–164, 2017.

[18] Y. Q. Lian, B. Tian, and S. Z. Wang, "The simulation of submarine-launched missile out-water movement based on matlab/simulink," in *Applied Mechanics and Materials*, vol. 182, pp. 1328–1332, Trans Tech Publ, 2012.

[19] S. Z. Wang, H. P. Wang, M. Yang, L. P. Wang, and G. W. Wei, "Simulation on three dimensional water-exit trajectory of submarine launched missile," in *Advanced Materials Research*, vol. 791, pp. 1069–1072, Trans Tech Publ, 2013.

[20] K. Zhao, L.-Q. Sun, J.-L. Zhao, and X.-O. Cheng, “Simulation analysis of wave effect on exceeding water gesture and load of submarine launched missile,” *Research Journal of Applied Sciences, Engineering and Technology*, vol. 7, no. 6, pp. 1113–1119, 2014.

[21] H. Dugoff, “Prediction of trajectories for an underwater missile,” tech. rep., Stevens Institute of Technology Hoboken NJ Davidson Lab, 1963.

[22] T. I. Fossen, *Nonlinear modelling and control of underwater vehicles*. Fakultet for informasjonsteknologi, matematikk og elektroteknikk, 1991.

[23] T. I. Fossen, *Guidance and control of ocean vehicles*. John Wiley & Sons Inc, 1994.

[24] T. I. Fossen, *Handbook of marine craft hydrodynamics and motion control*. John Wiley & Sons, 2011.

[25] P. D. Groves, *Principles of GNSS, inertial, and multisensor integrated navigation systems*. Artech house, 2013.

[26] J.-L. Boiffier, *The dynamics of flight*. Wiley,, 1998.

[27] P. C. Hughes, *Spacecraft attitude dynamics*. Courier Corporation, 2012.

[28] O. Egeland and J. T. Gravdahl, *Modeling and simulation for automatic control*, vol. 76. Marine Cybernetics Trondheim, Norway, 2002.

[29] G. Antonelli and G. Antonelli, *Underwater robots*, vol. 3. Springer, 2014.

[30] M. E. Rentschler, “Dynamic simulation modeling and control of the odyssey iii autonomous underwater vehicle,” Master’s thesis, Massachusetts Institute of Technology, 2003.

[31] K. A. Wise and D. J. B Roy, “Agile missile dynamics and control,” *Journal of Guidance, Control, and Dynamics*, vol. 21, no. 3, pp. 441–449, 1998.

[32] R. D. Blevins and R. Plunkett, “Formulas for natural frequency and mode shape,” *Journal of Applied Mechanics*, vol. 47, p. 461, 1980.

[33] J. N. Newman, *Marine hydrodynamics*. MIT press, 2018.

[34] C. Rosema, J. Doyle, L. Auman, M. Underwood, and W. B. Blake, "Missile datcom user's manual-2011 revision," tech. rep., Aviation and Missile Research, Development, and Engineering Center Redstone Arsenal AL, 2011.

[35] D. McLean, "Automatic flight control systems(book)," *Englewood Cliffs, NJ, Prentice Hall, 1990, 606*, 1990.

[36] D. E. Kirk, *Optimal control theory: an introduction*. Courier Corporation, 2012.

[37] J. L. Speyer and D. H. Jacobson, *Primer on optimal control theory*, vol. 20. Siam, 2010.

[38] M. Horton, "Autopilots for tactical missiles: An overview," *Proceedings of the Institution of Mechanical Engineers, Part I: Journal of Systems and Control Engineering*, vol. 209, no. 2, pp. 127–139, 1995.

[39] G. P. Sutton and O. Biblarz, *Rocket propulsion elements*. John Wiley & Sons, 2016.

[40] P. Zarchan, *Tactical and strategic missile guidance*. American Institute of Aeronautics and Astronautics, Inc., 2012.

[41] D. E. Williams, B. Friedland, and A. N. Madiwale, "Modern control theory for design of autopilots for bank-to-turn missiles," *Journal of Guidance, Control, and Dynamics*, vol. 10, no. 4, pp. 378–386, 1987.

[42] J. G. Lee, H. S. Han, and Y. J. Kim, "Guidance performance analysis of bank-to-turn (btt) missiles," in *Proceedings of the 1999 IEEE International Conference on Control Applications (Cat. No. 99CH36328)*, vol. 2, pp. 991–996, IEEE, 1999.

[43] W. S. Levine, *The Control Handbook*. CRC Press, Inc., 1999.

[44] A. Visioli, *Practical PID control*. Springer Science & Business Media, 2006.

[45] K. Ogata and Y. Yang, *Modern control engineering*, vol. 4. Prentice-Hall, 2002.

[46] J. Doyle and G. Stein, "Robustness with observers," *IEEE transactions on automatic control*, vol. 24, no. 4, pp. 607–611, 1979.

[47] J. C. Doyle, "Synthesis of robust controllers and filters," in *The 22nd IEEE Conference on Decision and Control*, pp. 109–114, IEEE, 1983.

[48] W. S. Levine, *The control systems handbook: Control system advanced methods*. CRC press, 2010.

[49] F. W. Nesline and P. Zarchan, "Why modern controllers can go unstable in practice," *Journal of Guidance, Control, and Dynamics*, vol. 7, no. 4, pp. 495–500, 1984.

APPENDIX A

THE CHARACTERISTICS OF SOME IMPORTANT FORCE AND MOMENT COEFFICIENTS

In this part, for the derived hydrodynamic and aerodynamic parameters of the missile in this study, the change of some important force and moment coefficients with angle of attack, at zero sideslip angle, zero control surface deflections and different Mach numbers are given in the following figures. The related coefficients are longitudinal static stability derivative ($C_{m\alpha}$), pitch damping derivative (C_{mq}), lift coefficient (C_L), elevator surface control effectiveness ($C_{m\delta_e}$), lateral static stability derivative ($C_{l\beta}$), directional static stability derivative ($C_{n\beta}$), roll damping derivative (C_{lp}), yaw damping derivative (C_{nr}) and their cross derivatives (C_{np} and C_{lr}), aileron surface control effectiveness ($C_{l\delta_a}$) and rudder surface control effectiveness ($C_{n\delta_r}$).

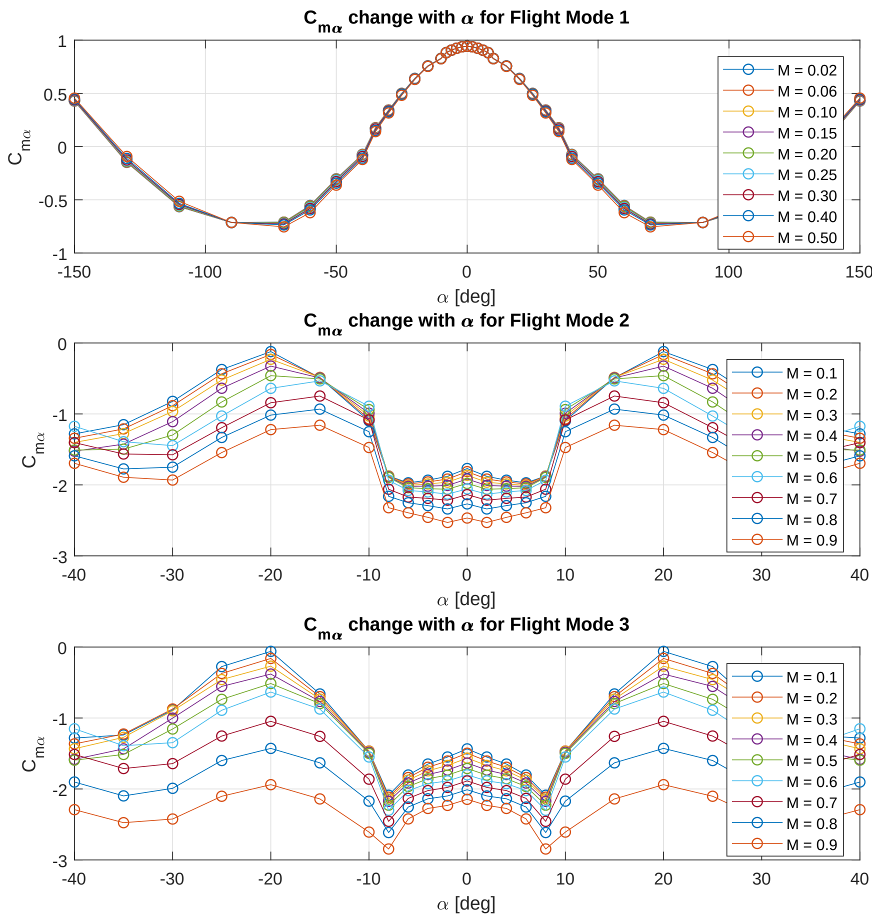

Figure A.1: $C_{m\alpha}$ change with α for different Mach numbers and $\beta = 0$

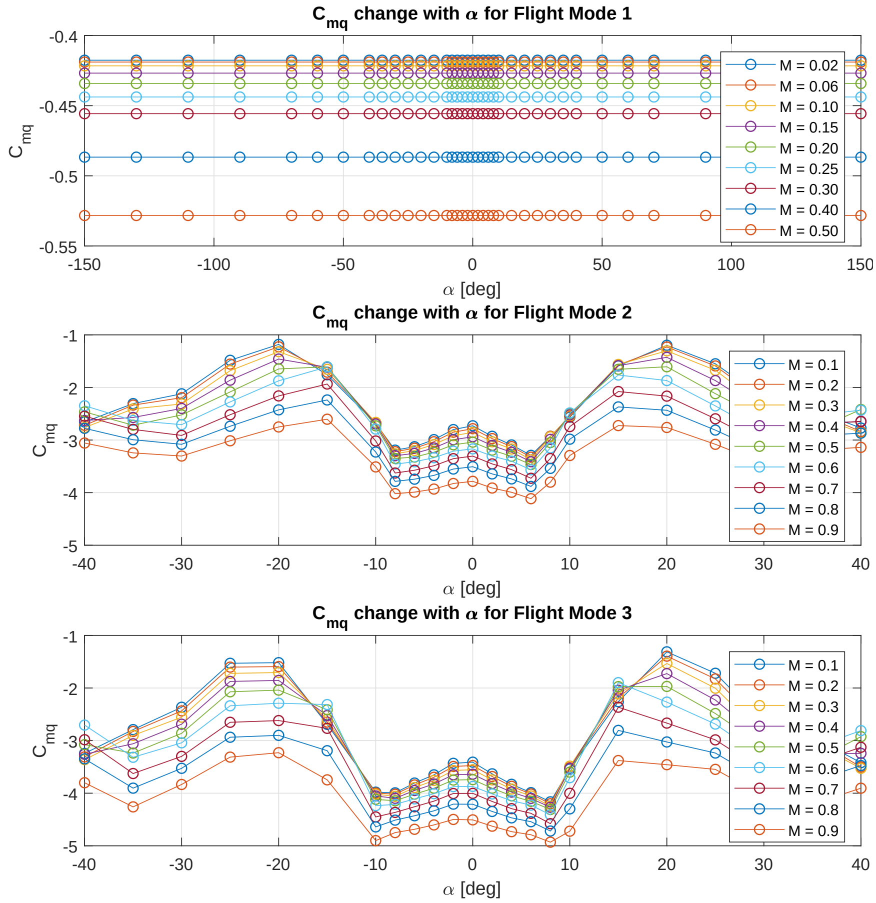

Figure A.2: C_{mq} change with α for different Mach numbers and $\beta = 0$

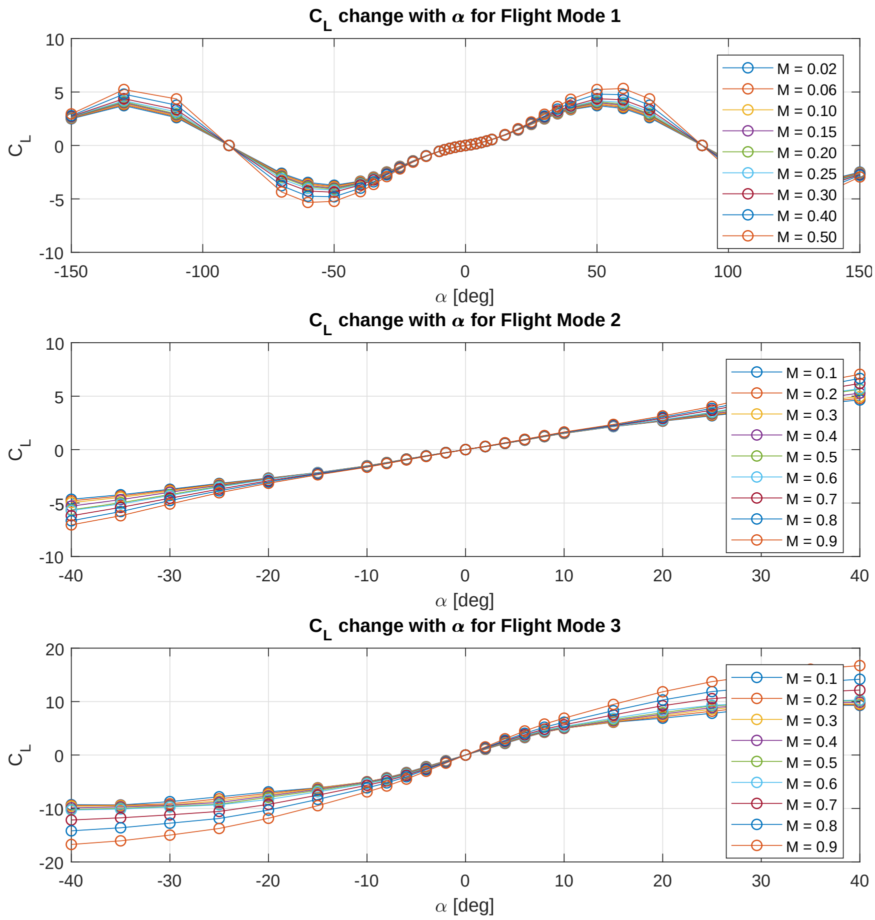

Figure A.3: C_L change with α for different Mach numbers and $\beta = 0$

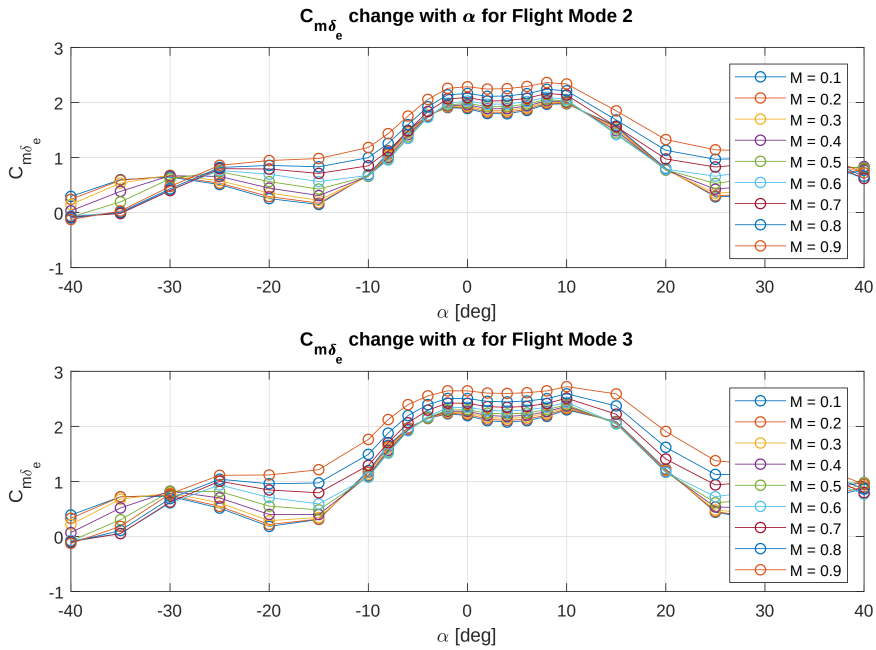

Figure A.4: $C_{m\delta_e}$ change with α for different Mach numbers and $\beta = 0$

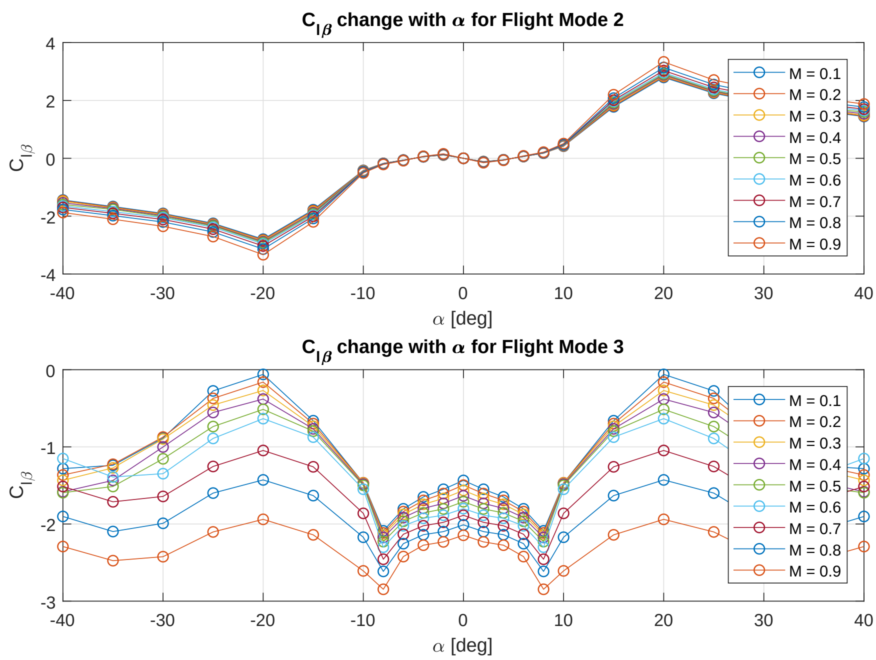

Figure A.5: C_{l_β} change with α for different Mach numbers and $\beta = 0$

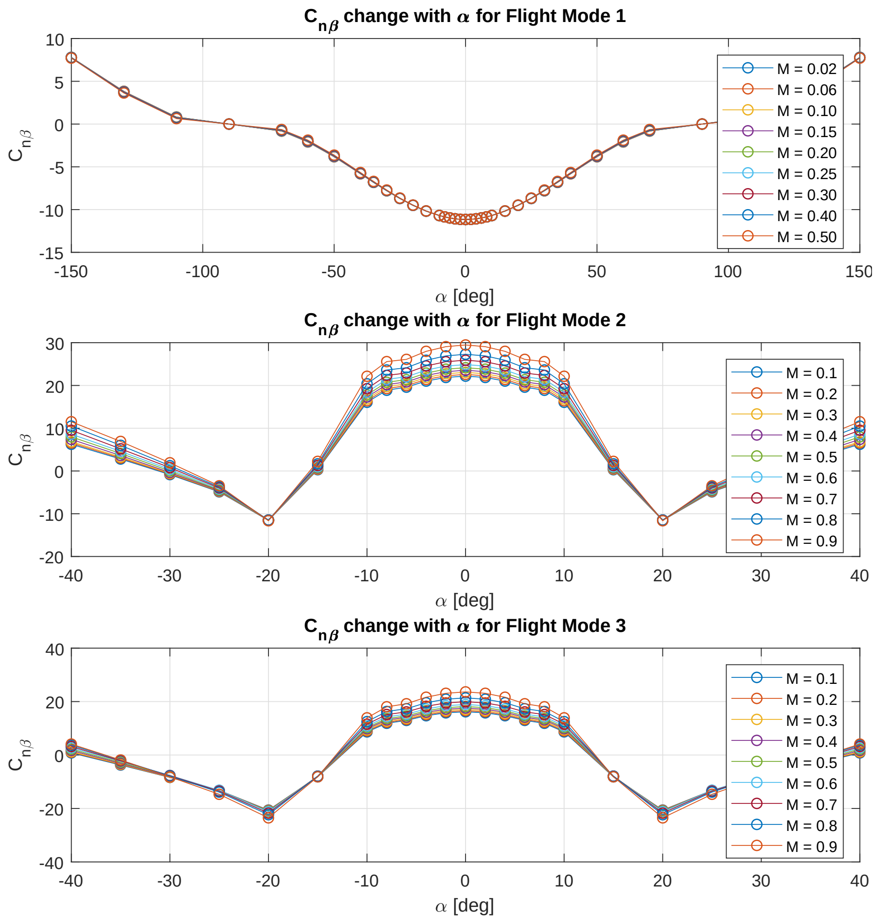

Figure A.6: C_{n_β} change with α for different Mach numbers and $\beta = 0$

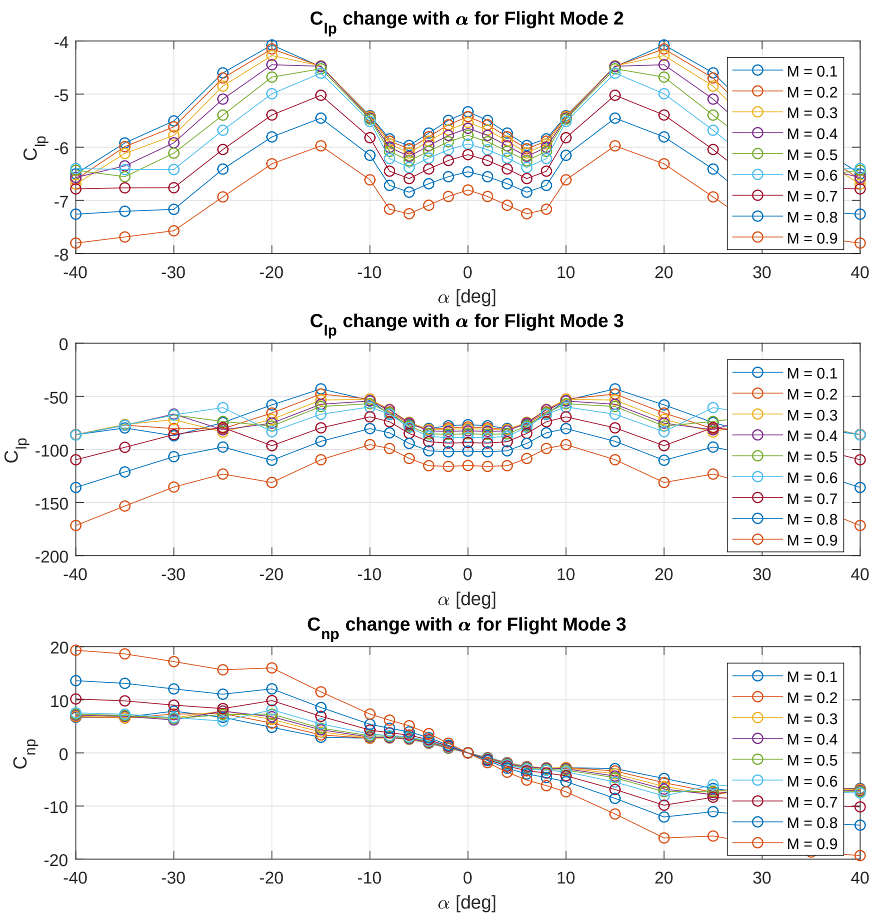

Figure A.7: C_{lp}, C_{np} change with α for different Mach numbers and $\beta = 0$

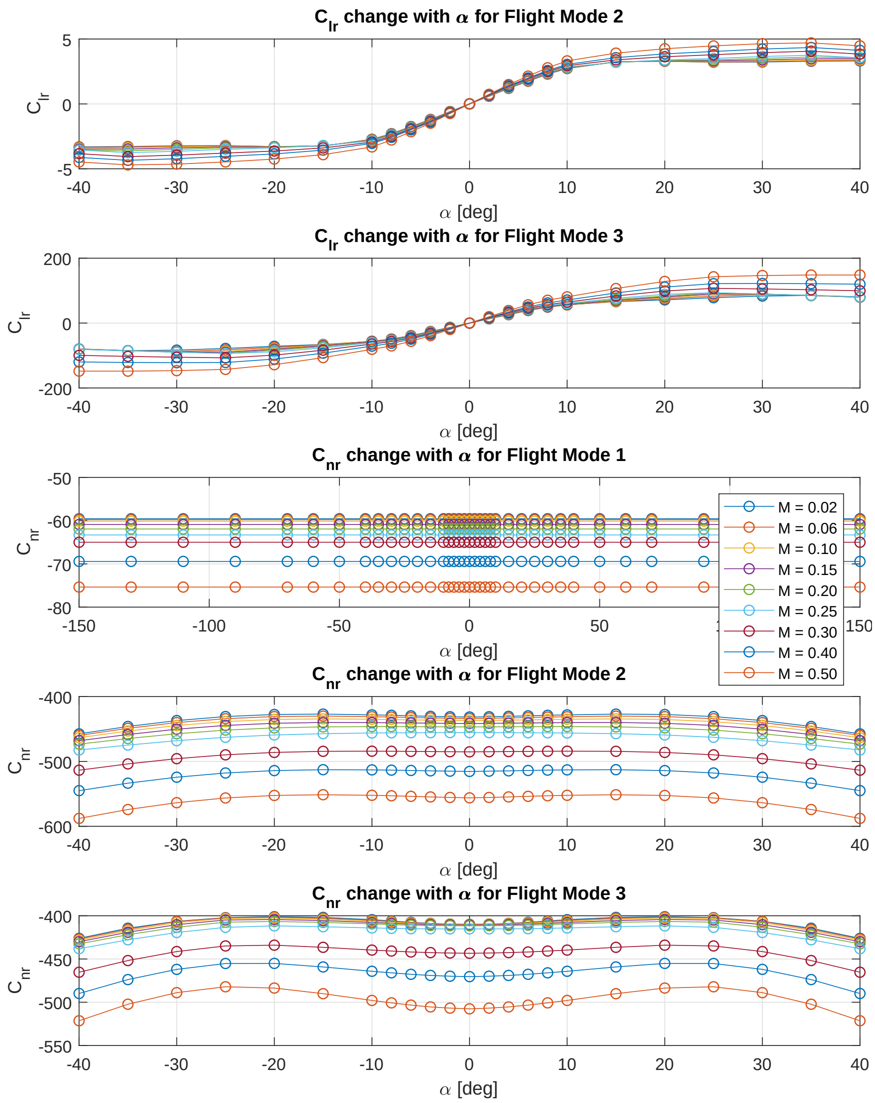

Figure A.8: C_{lr}, C_{nr} change with α for different Mach numbers and $\beta = 0$

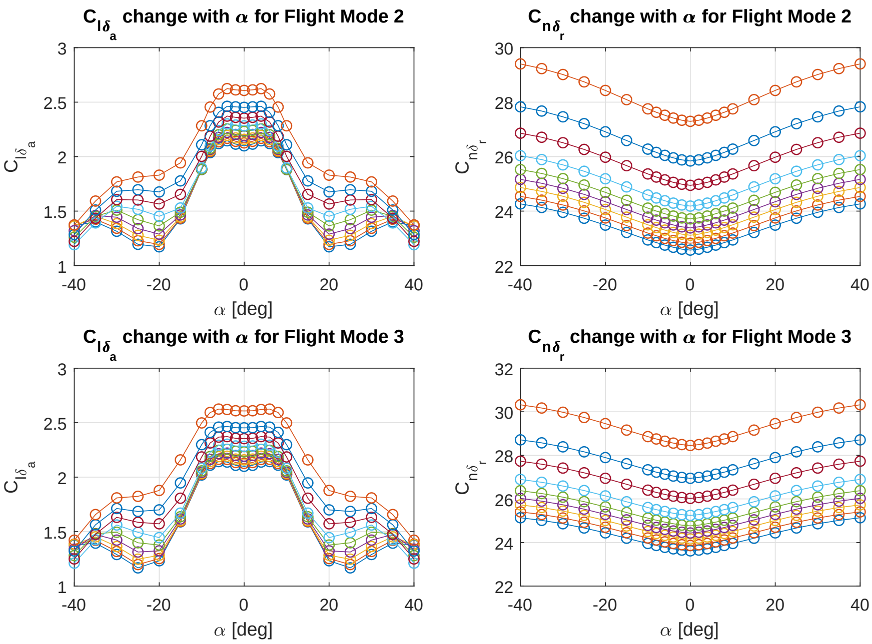

Figure A.9: $C_{l\delta_a}, C_{n\delta_r}$ change with α for different Mach numbers and $\beta = 0$